Forschungszentrum Jülich
in der Helmholtz-Gemeinschaft

Electronic Structure of Ferromagnet-Insulator Interfaces: Fe/MgO and Co/MgO

Martina Müller

Materie und Material
Matter and Materials

Schriften des Forschungszentrums Jülich
Reihe Materie und Material/Matter and Materials Band/Volume 40

Forschungszentrum Jülich GmbH
Institut für Festkörperforschung
Elektronische Eigenschaften (IFF-9)

Electronic Structure of Ferromagnet-Insulator Interfaces: Fe/MgO and Co/MgO

Martina Müller

Schriften des Forschungszentrums Jülich
Reihe Materie und Material/Matter and Materials Band/Volume 40

ISSN 1433-5506 ISBN 978-3-89336-493-0

Bibliographic information published by the Deutsche Nationalbibliothek.
The Deutsche Nationalbibliothek lists this publication in the Deutsche Nationalbibliografie; detailed bibliographic data are available in the Internet at http://dnb.d-nb.de.

Publisher and Distributor:	Forschungszentrum Jülich GmbH Zentralbibliothek, Verlag D-52425 Jülich phone +49 2461 61-5368 ·fax +49 2461 61-6103 e-mail: zb-publikation@fz-juelich.de Internet: http://www.fz-juelich.de/zb
Cover Design:	Grafische Medien, Forschungszentrum Jülich GmbH
Printer:	Grafische Medien, Forschungszentrum Jülich GmbH
Copyright:	Forschungszentrum Jülich 2007

Schriften des Forschungszentrums Jülich
Reihe Materie und Material/Matter and Materials Band/Volume 40

D 464 (Diss., Univ. Duisburg-Essen, Campus Duisburg, 2007)

ISSN 1433-5506
ISBN 978-3-89336-493-0

The complete volume is freely available on the Internet on the Jülicher Open Access Server (JUWEL) at http://www.fz-juelich.de/zb/juwel

Contents

Chapter 1

Introduction

Half a century of magnetic data storage has changed the world. A constantly increasing storage density has provided the basis for exciting innovations. In nowadays life, we take advantage of small portable devices like laptops or iPods providing hard disc capacities of up to some hundreds of Gigabytes. This stunning technological progress has become possible by experimental achievements that are intimately connected to the basic research on the magnetism of thin films and surfaces. Initially, this research was driven by scientific curiosity to understand the quantum mechanical processes which are governing the magnetic behavior in confined magnetic systems. The results had a direct impact on the magnetic data storage, by improving the materials itself and developing novel storage functionalities.

The last decade has witnessed further progress in information technology, which was initialized by two fundamental discoveries being closely connected to the magnetism in ultrathin magnetic layers. The discovery of the phenomenon of interlayer exchange coupling in 1986 by P. Grünberg and Co-workers [1] and the giant magnetoresistance (GMR) effect in 1988, by the groups of P. Grünberg and A. Fert [2, 3] mark the advent of the field of spin-based electronics ('spintronics'), in which magnetism and solid state electronics are joining to exploit spin-dependent transport processes [4]. The GMR effect is based on the arrangement of two successive magnetic layers, separated by a very thin non-magnetic layer. The relative orientation of the magnetization in the adjacent layers can be easily switched by applying a weak magnetic field, with the magnitude of the electric resistance being affected in an disparately way: An electric current can flow rather freely, if the layer magnetization is oriented parallel, while a high resistance results if they are antiparallel. The GMR effect in magnetic multilayers can be studied in so-called spin-valves, in which the direction of the magnetic moment of an magnetic reference layer is fixed by the phenomenon of exchange bias. Today, the field of spin-based electronics drives the progress in magnetism and provides the basis for novel electronic functionalities that in part are already conversed into technology. The GMR effect, for instance, has completely revolutionized the magnetic recording industry: the very high sensitivity of GMR-based read heads has allowed a reduction of the bit size, and hence an enormous increase in the storage capacity of magnetic hard-disk drives. Now, about twenty years after its discovery, all hard-disks in computers are equipped with read heads based on the GMR effect.

In the two decades since the discovery of GMR, the magnitude of the GMR signal in spin valve structures has changed very little. The resistance of such structures is typi-

cally about 10-15% higher, if the reference magnetic moments are oriented antiparallel in comparison to the parallel case. Partly for this reason, interest has been turned towards magnetic multilayer thin film stacks, which are based on two ferromagnetic electrodes magnetically decoupled by a thin insulating layer. The virtue of these so-called magnetic tunnel junctions (MTJs) is a much larger change in resistance from the parallel to the antiparallel magnetization state, which is known as tunneling magnetoresistance (TMR). Since the first observation of large reproducible TMR at room temperature in amorphous aluminum oxide based MTJs, there has been a surge in research in this field [5, 6]. Recently, magnetic tunnel junctions have been significantly improved with the discovery of much higher magnetoresistive ratios of several hundred percent using magnesium oxide tunnel barriers and $3d$ transition metal ferromagnetic alloy electrodes [7, 8]. And this is certainly not the end of the development: In contrast to the metallic GMR sensors, there is – at least theoretically – no limit for the magnitude of the tunnel magnetoresistance in MTJs [9, 10]. Therefore, magnetic tunnel junctions look promising for magnetic memory storage elements (MRAM) and highly sensitive magnetic field sensors. A further progress, however, is tied to an improved understanding and control of the physical processes governing the TMR.

Scientific groups all over the world are pushing forward research on the electronic and transport properties of MTJs in search of a systematical understanding of the complex physical mechanisms which underly the TMR effect. The phenomenon of TMR is a consequence of spin-dependent tunneling (SDT), which is an imbalance in the electric current carried by spin up and spin down electrons tunneling from the ferromagnetic electrode through the tunneling barrier. The magnitude of TMR is thereby determined by the spin polarization of the tunneling current. A detailed understanding of the relationship between the tunneling magnetoresistance and the corresponding spin polarization of the tunneling current to the ferromagnetic and tunneling barrier materials is still developing. Interestingly, the magnitude of the TMR signal is found to be rather insensitive to the ferromagnetic electrode material. For many years, the tunneling spin polarization was considered to be only related to the fundamental electronic structure of the ferromagnetic electrodes and, in particular, to the degree of spin polarization of the density of states at the Fermi level of the electrodes [11]. It has become clear, that this model is too simplified and that the properties of the tunnel barrier and its interface with the magnetic electrodes are extremely important in determining the degree of spin polarization of the tunnel current and, consequently, the tunneling magnetoresistance.

Indeed, the most important physics in SDT is mainly related to the interfaces of the ferromagnet-insulator-ferromagnet systems. Recent theoretical studies provided new insights into this aspect by deducing the spin dependence of the tunneling current in single-crystalline MTJs from the symmetry of the Bloch states in the bulk ferromagnetic electrodes and the complex band structure of the insulator [12, 13]. By identifying those bands in the electrodes that are coupled efficiently to the evanescent states decaying most slowly in the insulating barrier, one can draw conclusions about the spin polarization of the tunneling current. In other words, the tunnel barrier can act as a spin filter. However, it has turned out that symmetry considerations alone are not always sufficient to predict the spin polarization of the tunneling current, because they assume perfectly sharp and well-ordered interfaces, which are hardly realized in real MTJs.

An important mechanism by which the interfaces affect the spin polarization of the tunneling conductance is the bonding between the ferromagnetic electrodes and the insulator. The interface bonding determines the effectiveness of transmission across the interface, because it can be different for electrons of different orbital character carrying an unequal spin polarization. Experimentally, the effect of bonding at the ferromagnet-insulator interface is proposed to explain the inversion of the spin polarization of electrons tunneling from Co electrodes across a $SrTiO_3$ and an Al_2O_3 barrier, respectively [14]. Moreover, theoretical studies predict that an atomic layer of iron oxide at the interface between Fe and MgO layers strongly reduces the TMR in Fe/MgO/Fe tunnel junctions due to the bonding between iron and oxygen [15, 16].

These findings suggest, that the magnitude of the tunneling spin polarization and, consequently, the tunneling magnetoresistance depends on several factors, such as the chemical composition of the insulating barrier and the atomic structure and bonding at the metal-oxide interfaces. Due to the difficulties in the atomic scale characterization of the magnetic tunnel junctions, there is only limited information on the structure and bonding at ferromagnet-insulator interfaces available so far. The situation is complicated by the fact, that in most cases the oxide layer is formed by first depositing a metallic layer on top of the ferromagnetic electrode and then oxidizing it by exposing the system to ambient oxygen or oxygen plasma [17]. This may result in the formation of an oxide layer with numerous defects and deviations in local stoichiometry at the interface. The oxidation time is critical for producing MTJs with oxide barriers: An over-oxidation produces a ferromagnet-oxide layer at the interface, that is unfavorable for transmitting spin polarization of the ferromagnetic electrode across the interface. An under-oxidation, in turn, leads to the presence of oxygen vacancies at the interface. Their impact on the spin-dependent tunneling process is not yet clear. It is therefore crucial to investigate ferromagnet-oxide interfaces with different oxide stoichiometries, as this approach provides the most realistic insight into the fundamental mechanisms ruling the metal-oxide bonding at real ferromagnet-insulator interfaces.

The physics of the ferromagnet-insulator interface largely relies on the nature of the interface electronic states close to the Fermi level. Generally, even small variations of the atomic potentials and bonding near the interface have a strong impact on the interfacial density of states. Such variations are common for real interfaces, and they are intimately reflected by the interface density of states formed by the $3d$ electronic structure of the transition metal electrodes. Hence, these effects influence the spin polarization of the tunneling current in real MTJs, and are directly related to the chemical bonds formed at the interface with the tunnel barrier. This, in turn, can improve the possibilities for altering the properties of MTJs. In particular, by modifying the electronic properties of the ferromagnet-insulator interface it seems to be possible to engineer MTJs with properties desirable for application.

However, the atomic-scale characterization of the complex interplay between the electronic structure and chemical bonding formation at ferromagnet-insulator interfaces poses an experimental challenge. A suitable experiment has to provide detailed information on the electronic structure of the ferromagnetic electrode as a function of the overlaying oxide composition. This endeavor requires elemental and surface sensitive information both for the ferromagnetic and the oxide electronic structure. As a matter of fact, the measurements

have to provide a spin resolved picture of the electronic states.

In this thesis, the role of the interface bonding at ferromagnet-insulator interfaces will be elucidated by probing the electronic states of ferromagnetic iron and cobalt films covered with ultrathin magnesium oxide barriers by means of spin- and angle-resolved photoemission spectroscopy. With its ability to investigate the electronic and magnetic properties of the ferromagnetic band structure with high surface sensitivity, low-energy photoemission spectroscopy is a suitable tool to investigate the interface with different MgO stoichiometries to quantify the effect of bonding and oxidation on the interfacial ground state electronic structure. The interplay between chemical bonding and electronic structure formation can be analyzed by combining elementally sensitive results from core-level and valence-band photoemission. Thus, the direct relation between the oxidation ratio of the MgO layer and the interfacial spin-polarization can be revealed. Moreover, this thesis aims at characterizing possible bonding mechanisms which rule the intrinsic electronic properties of the ferromagnet/insulator interfaces. It is organized as follows:

Chapter 2 reviews the fundamental physical aspects, which arise when discussing the interfacial properties of the ferromagnetic electronic structure in contact with ultrathin MgO_x overlayers. Primarily, we address the main properties of the spin-split electronic structure of the $3d$ ferromagnets. The occupied electronic states of the latter are probed by a spin- and angle-resolved photoemission experiment. The fundamental physical processes yielding the excitation and emission of spin-polarized electrons are discussed in the framework of the three-step model. The photoemission results are compared to ab-inito bandstructure calculations, which are performed in the framework of density functional theory. Finally, we will discuss the relation between the ferromagnetic bandstructure and the spin-dependent transport properties in magnetic tunnel junctions in more detail. Moreover, we will point out the necessity to investigate ferromagnet-insulator interfaces beyond simple model systems and highlight the decisive role of the interfacial properties for the tunneling spin polarization.

The experimental techniques, which are extensively employed to investigate the structural, chemical and magnetic properties of the ferromagnet/insulator surfaces and interfaces are presented in **chapter 3**. Different physical aspects have to be considered to conduct a successful spin- and angle-resolved photoemission experiment: Clean, single-crystalline samples with flat surfaces can be prepared by molecular beam epitaxy and provide the basis for angular-resolved photoemission studies of the electronic band structure. The knowledge on the magnetic anisotropy is necessary for the spin-detection process. We will address selected practical details of data acquisition and interpretation of the several experimental methods and briefly sketch the layout of the experiment.

In **chapter 4**, the successive preparation steps yielding the MgO_x/Fe(001) and MgO_x/Co(001) systems are reviewed in detail. We will present and discuss results on the crystalline structure of the substrate and the ferromagnetic films and analyze the magnetic anisotropy of the latter. The chemical environment at the surface of the substrate and the ferromagnetic film, as well as of the ultrathin MgO_x overlayer is quantified. A crucial parameter is given by the MgO degree of oxidation, which is addressed by means of core level spectroscopy.

In **chapter 5**, the experimental results on the electronic structure at MgO_x/Fe(001) and MgO_x/Co(001) interfaces obtained by spin- and angle resolved photoemission spectroscopy

are presented in detail. The studies thereby focus on the response of the ferromagnetic electronic structure in contact with MgO overlayers, which deviate from a well-balanced oxide stoichiometry. By combining results from core-level and valence-band spectroscopy, the close connection between the chemical bonding and electronic structure formation is unraveled. We will discuss the results with regard to possible atomic environments, which reflect the type of bonding mechanism governing the interfacial electronic structure. We will show, that the electronic structure of ferromagnet/insulator interfaces is sensitively controlled by the interface chemistry. A beneficial influence on the interfacial spin polarization is manifested for oxygen-deficient MgO layers on ferromagnetic substrates. This finding is supposed to have a significant influence on the spin-dependent tunneling process in magnetic tunnel junctions.

Finally, a concluding discussion of the main results of this thesis is given in **chapter 6**.

Chapter 2

Fundamental Aspects

The present chapter gives an overview about the general physical aspects, which are extensively employed in this thesis. The overall aim of this work is to explore the spin-split electronic structure of ferromagnetic materials in contact with ultrathin insulating overlayers. Several physical and experimental aspects come into play, which are addressed in the following.
The first part of the chapter introduces the occurrence of $3d$ ferromagnetism within the framework of band magnetism. The spontaneous magnetic order of itinerant electrons is a consequence of the minimization of the total energy of the correlated many-particle system. The electronic structure of a magnetic solid is separated into majority and minority states by the so-called exchange energy. An intrinsic parameter of a ferromagnet is its spin polarization, which is a measure for the spin imbalance of the occupied electronic states.
The most suitable method to determine the spin-split electronic structure of a ferromagnet experimentally, is a spin- and angle-resolved photoemission spectroscopy experiment. If operated in the low-energy regime, the short probing depth makes it particularly suited to study surfaces and interfaces. The basic theory of photoemission in terms of single-electron excitations is discussed in the second part of this chapter. Theoretical calculations of the band structure on the basis of spin-polarized density functional theory are employed to compare experimental results with ab inito predictions on the spin-split electronic structure. The basic ideas of spin-polarized DFT are sketched and discussed with respect to their applicability to describe the relevant experimental systems.
The electronic structure of a ferromagnet in contact with an insulator is an important issue in the lively field of spinelectronics. This branch of research investigates the spin dependence of electronic transport, with the main parameter given by the transport spin polarization of the electric current. In a magnetic tunnel junction, the tunneling spin polarization (TSP) gives rise to the tunneling magnetoresistance (TMR) effect. The electronic properties at the ferromagnet/insulator interface thereby are recognized to mainly determine sign and magnitude of the TSP. In particular, the ferromagnetic bandstructure in contact with its complex insulator counterpart acts as a spin filter for the tunneling electronic states. Thus, the ground state spin polarization does not equal that of a tunneling current. We will consider the various factors controlling the spin polarization of the tunneling current and emphasize the decisive role of the interface bonding beyond simple ferromagnet-insulator-ferromagnet systems.

2.1 Electronic structure of $3d$ ferromagnets

2.1.1 Ferromagnetism of $3d$ transition metals

The characteristic property of ferromagnetism in a solid is the spontaneous long-range order of magnetic moments in absence of an applied magnetic field and below a critical temperature. Ferromagnetic materials are usually divided into two classes, the localized and the itinerant ferromagnets. In localized ferromagnets, which are represented by the $4f$ or $5f$ rare-earth metals, the magnetic moment is carried by localized electrons, which are only weakly involved in interaction processes. These materials are successfully treated by spin-lattice models, which consider the isolated magnetic moments as being fixed at particular lattice sites [18]. The magnetic moments of the $3d$ elements Fe, Co and Ni, in contrast, are carried by the strongly delocalized valence electrons close to the Fermi level. These itinerant electrons play the crucial role in any interaction, like e.g. bonding, hybridization or transport processes. In order to describe the phenomenon of itinerant ferromagnetism, the valence electrons have to be treated collectively. The ferromagnetic ground state of such a many-electron system favors the parallel alignment of neighboring spins [19]. The origin for this collective ordering phenomenon is the quantum mechanical exchange interaction, which basically reflects a balance of electrostatic energies of electrons by taking into account their spin character. The Pauli principle correlates electrons with parallel spins by excluding that two electrons possess the same set of quantum numbers and thus occupy the same electronic state. As a consequence, electrons have to be promoted into higher energy states, since every state can be occupied by only one electron in comparison to the non-magnetic case. The parallel orientation of electron spins is therefore followed by an increase in kinetic energy. At the same time, as another consequence of the Pauli principle, the density of electrons close to another electron with the same spin orientation is reduced, and the particular electron is surrounded by a so-called exchange hole. By keeping particles with the same charge apart, the Coulomb repulsion is reduced. This reduction of electrostatic energy for the parallel spin alignment in comparison to the antiparallel situation is called exchange energy. For the total energy balance, this means that whenever the gain in exchange energy exceeds the increase of kinetic energy, the many-electron system can minimize its total energy by aligning spins parallel in a magnetically ordered ground state.

In the present case of itinerant ferromagnetism, the energetic states of the valence electrons correspond to electronic band states in the solid. This particular aspect is of great importance in order to finally formulate the criterion for the occurrence of itinerant ferromagnetism, the so-called Stoner criterion. The Stoner criterion relates the energy balance between kinetic and exchange energy to the electronic structure of the ferromagnet. A formal description of the Stoner model is usually given in the frame of density functional theory (DFT) including spin polarization [21]. The basic ideas of this approach are discussed in the following.

Stoner criterion

According to the Stoner model, the interaction between the itinerant electrons is mediated by a molecular field, which arises from the exchange interaction [20]. If the molecular

field is treated in a mean field approach, the local magnetization M, which is induced by the exchange interaction, is the same for each atom [21]. M thus can be defined as the difference between the density of states of spin-up and spin-down electrons $D^{\uparrow}(E)$ and $D^{\downarrow}(E)$ in one atomic unit cell according to

$$M = \int^{E_F} (D^{\uparrow}(E) - D^{\downarrow}(E))\, dE. \tag{2.1}$$

In the spin-polarized DFT formalism, all spin-dependent interactions enter into the so-called exchange-correlation potential $V_{xc}^{\uparrow,\downarrow}$, which is one part of the total effective potential within the Kohn-Sham-equations (see chapter 2.2.4 for a basic introduction to the DFT formalism). The interaction between the magnetization M with the electronic system is only a small parameter [21]. $V_{xc}^{\uparrow,\downarrow}$ can thus be expanded and written in the approximated form as

$$V_{xc}^{\uparrow,\downarrow} = V_{xc}^{0} \mp \widetilde{V} \cdot M. \tag{2.2}$$

V_{xc}^{0} thereby denotes the exchange-correlation potential for the non-magnetic case. Since the mean value of $\widetilde{V}$ is positive, the spin-up electrons ($\uparrow$) feel a stronger attractive potential (-) as in the non-magnetic case, while the minority electrons ($\downarrow$) feel a stronger repulsive potential (+). In the Stoner model, this enhancement or decrease of the potential is simulated by a constant

$$V_{xc}^{\uparrow,\downarrow} = V_{xc}^{0} \mp \frac{1}{2} I \cdot M. \tag{2.3}$$

I represents the exchange integral or Stoner parameter, which averages over the Coulomb interactions in the many-particle system. It is a measure for the exchange interaction strength between the atoms. In the course of a further procedure, this approach leads to a sufficient condition for the occurrence of ferromagnetism [19], by self-consistently relating the energy shift (2.3) to the magnetization (2.1). Ferromagnetic solutions exist, if

$$I \cdot D(E_F) > 1. \tag{2.4}$$

This relation is known as the Stoner criterion. It connects the exchange integral I of the many-particle system to the density of states $D(E)$. The condition for the ferromagnetic instability is fulfilled for those materials, in which the Coulomb effects are strong and the density of states $D(E_F)$ at the Fermi energy is large. Since the value of the exchange interaction is very similar for all 3d transition metals ($I \sim 1$ eV), the density of states $D(E_F)$ represents the most important parameter in the Stoner criterion [22].

Nevertheless, the Stoner criterion for itinerant ferromagnetism is only fulfilled for the 3d transition metals Fe, Co and Ni. Their density of states are calculable in the framework of spin-polarized density functional theory. The mean field approach for the exchange interaction enters the DFT calculations by the local spin density approximation (LSDA), which contains all spin- and many-particle interactions of the exchange-correlation potential V_{xc}. Figure 2.1 shows the spin-split density of states for Fe, Co and Ni, calculated by employing the SPR-KKR method developed by Ebert *et al.* [23]. Obviously, the density of states directly at the Fermi level is dominated by large contributions of localized 3d bands of either majority (Fe) or minority (Co, Ni) character, which is the main reason for these materials to fulfil the Stoner criterion.

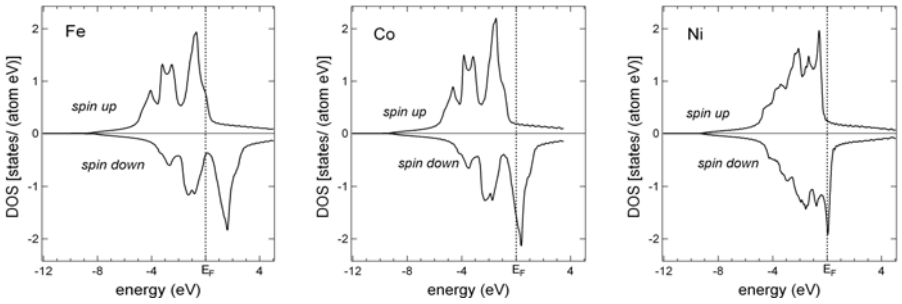

Figure 2.1: Spin-split density of states calculated for ferromagnetic bcc-Fe, bcc-Co and fcc-Ni. Whereas the spin-projected DOS at the Fermi level reveals a positive sign for Fe, a negative value is observed for Co and Ni.

2.1.2 Spin-split electronic bands

An important result, which arises from the Stoner model, is the occurrence of a spin splitting of the electronic structure of the 3*d* ferromagnets. It can be derived from equation (2.3), that the constant change $I \cdot M/2$ of the potential $V_{xc}^{\uparrow,\downarrow}$ does not act on the spatial part of the electronic wavefunctions $\psi^{\uparrow,\downarrow}(\mathbf{r}) = \psi^{0}(\mathbf{r})$ in comparison to the non-magnetic case [21]. The energy eigenvalues $\varepsilon^{\sigma}(\mathbf{k})$ ($\sigma = \uparrow, \downarrow$), however, are shifted by this constant value. The presence of the exchange interaction thus lifts the two-fold degeneracy of the electronic states and formally results in a spin-splitting of the electronic structure according to

$$\varepsilon^{\uparrow,\downarrow}(\mathbf{k}) = \varepsilon^{0}(\mathbf{k}) \mp \frac{1}{2} I \cdot M. \tag{2.5}$$

In the absence of spin-orbit coupling, majority and minority bands can be viewed as two independent sets of bands, which are separated by the constant exchange splitting $\Delta_{xc} = I \cdot M$. At this point, the Stoner model provides a rather simplified picture, since in most systems, the exchange splitting Δ_{xc} is not always a constant, but may vary with the electron wavevector $\mathbf{k}$ and the symmetry of the bands. To underline this fact, the spin polarized band structure of bcc-Fe has been calculated within the LSDA approximation according to [23]. Figure 2.2 shows the dispersion $E(\mathbf{k}, \uparrow)$ and $E(\mathbf{k}, \downarrow)$ along the Γ-Δ-H high symmetry line. It reveals the typical features of the 3*d* bandstructures: On the one hand, the region in the vicinity of the Fermi level is characterized by weakly dispersive *d* bands, which are embedded into strongly dispersive *sp*-bands on the other hand. The exchange splitting between spin-up and spin-down bands of the same symmetry is obvious, but shows that Δ_{xc} is much larger for the *d* states than for the s, p-type bands. The orbital representation of the electronic states is linked to the symmetry of the crystal, as will be introduced in chapter 2.1.3.

As the atomic number increases from Fe to Co and Ni, the *d* bands become increasingly filled and move down below the Fermi level. By considering again the spin-resolved DOS in Figure 2.1, it is obvious that the majority density of states $D^{\uparrow}(E)$ is not completely filled for Fe, but it is already for Co and Ni. The minority density of states $D^{\downarrow}(E)$, in contrast,

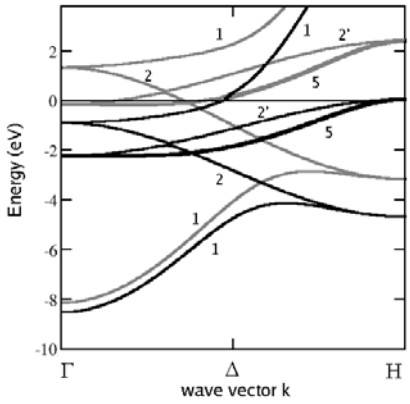

Figure 2.2: Spin-resolved bandstructure for bcc-Fe along Γ-Δ-H. Black lines: majority spins, grey lines: minority spins. The symmetries are labeled according to the single-group representation.

is partially occupied for all three 3d ferromagnets. As a consequence, the spin-projected DOS of Fe reveals a larger majority DOS at the Fermi level, in contrast to Co and Ni, where a large minority spin DOS dominates the region below the Fermi level (see Fig. 2.1).

Spin polarization

An important parameter characterizing the occupied states of the 3d ferromagnets Fe, Co and Ni is the spin-imbalance between spin-up and spin-down electrons. This quantity is referred as the ground state spin polarization P_D. The spin polarization of a bulk ferromagnet can be defined via the spin-dependent density of states D^σ ($\sigma = \uparrow, \downarrow$), which is expressed in terms of the electronic bandstructure according to

$$D^\sigma = \frac{1}{(2\pi)^3} \sum_\alpha \int \delta(E_{\mathbf{k}\,\alpha\,\sigma})\; d^3k, \tag{2.6}$$

with $E_{\mathbf{k}\,\alpha\,\sigma}$ being the energy of an electron in the band α and with a spin σ [24]. The spin polarization P_D is defined as the normalized difference between spin up and spin down electrons and takes the form

$$P_D(E) = \frac{D^\uparrow(E) - D^\downarrow(E)}{D^\uparrow(E) + D^\downarrow(E)}, \tag{2.7}$$

with $D^\uparrow$ and $D^\downarrow$ being the electronic density of states for spin-up and spin-down electrons, respectively. It is often assumed erroneously, that this very definition of P_D is measurable in a spin-resolved photoemission experiment [24]. In fact, as will be presented in the following section, photoemission is essentially a many-particle process and the photoemission spectrum reflects rather an excited state than the ground state of the electronic structure.

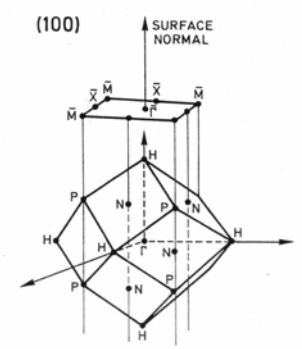

C_{4v}	orbital representation
Δ_1	s, p_z, d_{z^2}
$\Delta_{2'}$	d_{xy}
Δ_2	$d_{x^2-y^2}$
Δ_5	p_x, d_{xz} and p_y, d_{yz}

Figure 2.3: Left: Brillouin zone of a bcc cubic lattice. The (001) high symmetry line is denoted as the Δ-line and ranges from the high symmetry point Γ to the edge H. Right: Symmetries along the Δ-line in a bcc cubic lattice with the corresponding orbital representations in terms of spherical harmonics. The notation of the x, y and z axis refer to the cubic directions in the bcc lattice.

Another discrepancy between the ground state polarization of a ferromagnet and the spin polarization measured in a photoemission experiment arises from the fact, that every optical transition has to be considered with respect to the dipole selection rules. The latter determines the spectral weight of the photoelectron transition and consequently influences the measured polarization (see chapter 2.2.2). Generally, any interpretation of a spin polarization obtained by a particular experimental method has to be considered under the special experimental restrictions, as will be further pointed out in chapter 2.3.1.

2.1.3 Excursus: Symmetry and electronic structure

The symmetry of a lattice is directly connected to the symmetries of the electronic bands, which are observable in the bulk band structure. The spatial symmetry of the lattice is mirrored by the crystal potential $V(\mathbf{r})$, which enters the Hamiltonian of the electronic system. Thus, only these electronic wavefunctions $\psi(\mathbf{r})$ solve the corresponding Schrödinger equation, which possess the the same spatial symmetry as the crystal potential $V(\mathbf{r})$. Therefore, electronic bands are usually denoted with respect to the particular crystallographic symmetry direction, which, for instance, can be probed by a photoemission experiment.

In terms of group theory, the sum of all possible symmetry operations in a lattice, i.e. translation, rotation and reflection, forms a mathematical group. At a particular point $\mathbf{k}$ in the Brillouin zone, this group is described by a set of irreducible representations, which can be used to classify the different electronic states $E(\mathbf{k})$, as the number of representations equals that of the different electronic states. It is thus possible to label the individual electronic states according to the irreducible representations of the point group of a particular direction within the cubic lattice.

In the following, the high symmetry direction (001) of bcc cubic crystals is considered

in detail, since it is of particular interest in the context of this thesis. The cubic (001) axis is also denoted as the Δ-line and connects the Brillouin zone center Γ with the zone edge H as shown in Figure 2.3. The (001) direction is a fourfold axis and refers to the C_{4v} symmetry group, which preserves the bcc crystal structure under all symmetry operations. This group consists of four irreducible representations, which are indexed as Δ_1, Δ_2, $\Delta_{2'}$ and Δ_5. Thus, the electronic structure along (001) of a cubic lattice consists of these four distinguishable electronic states in terms of their spatial symmetry. In the case of a magnetic solid, the spin orientation can simply be added to the notation, if spin-orbit interaction is negligible. This aspect will be further elucidated in chapter 2.2.2.

In a further step, the symmetry of an electronic state can alternatively be expressed in terms of its angular-momentum representation. The electronic wave functions are denoted as $\psi_{nlm}(\mathbf{r})$ in terms of the spherical harmonics $Y_{l,m}$ [25]. The angular momentum number $l = 0, 1, 2, ..n-1$ represents states of s ($l = 0$), p ($l = 1$) and d ($l = 2$) character, whereas the magnetic quantum number $m_l = -l, .., 0, .., l$ gives the component of the angular momentum vector in direction of the z-axis (e.g. $p_x\,(l = 1, m_l = -1)$). Strictly speaking, this single-electron notation cannot be applied to a solid, which does not possess a continuous rotational symmetry, i.e. the deviation from the spherical symmetry is not negligible. However, there is an analogy between the irreducible representation and the orbital momentum notation [22]. By considering again the (001) orientation of a bcc lattice, one finds the most symmetric state given by a Δ_1 symmetry, which can alternatively be described by a $s\,(l = 0)$-like state. The Δ_5 symmetry states can be viewed as composed of wavefunctions of pd-character (see Table 2.3).

The angular symmetry of the electronic states has consequences for the bonding in a cubic crystal [25]. The d states, for instance, can be divided into two different classes, the so-called t_{2g} and e_g orbitals. In a cubic lattice, these orbitals reveal a bonding- or antibonding character, respectively, depending on the strength of electrostatic repulsion between each other. The t_{2g} orbitals are represented by the d_{xy}, d_{xz} and d_{yz} orbitals, which are aligned along the diagonals between the x, y and z cubic axes. The e_g orbitals, in contrast, are orientated along the main axes $d_{z^2-r^2}$ and $d_{x^2-y^2}$. In a bcc crystal lattice, the d orbitals of adjacent atoms will overlap and this process leads to an energetic splitting: The t_{2g} orbitals are lowered in energy due to their small orbital overlap and low electrostatic repulsion, thus revealing a bonding character. The e_g orbitals, in contrast, are raised in energy due to a large overlap in x, y, z-direction, which leads to an antibonding character. Bonding and antibonding states of a particular element are distinguishable e.g. in a calculated density of states, since the contributions are shifted on the energy scale.

2.2 Basic Aspects of Spin- and Angle-Resolved Photoemission Spectroscopy

Photoemission spectroscopy is an established method to explore the electronic structure of a solid. Due to its short probing depth, low-energy photoemission is particularly suited to study surfaces and interfaces, as well as thin films in the monolayer regime. The main objective of the experiment is to retrieve information on the occupied electronic states through the analysis of the photoemitted electrons. The experimental quantities, which have to be determined for this purpose, are the photoelectron's kinetic energy and momentum, which yield direct information on the binding energy and the wavevector. Therefore, the theory of photoemission is primarily a description in terms of angle-resolved photoemission, which maps out the dispersive electronic band structure with **k**-resolution $E(\mathbf{k})$.

In ferromagnets, however, a complete characterization of the electronic structure includes the analysis of electrons also with respect to their spin σ ($\sigma = \uparrow, \downarrow$). The information is provided by a measurement of the spin polarization P of the photoelectrons. A combined spin- and angle-resolved photoemission experiment hence enables one to exploit the complete information on the spin-split ferromagnetic electronic states $E(\mathbf{k}, \uparrow)$, $E(\mathbf{k}, \downarrow)$. For an extended analysis, the experimentally determined photoemission results can be compared with theoretical band structure calculations.

Phenomenologically, the photoemission process is based on the photoelectric effect as formulated by Einstein in the early 20$^{\text{th}}$ century. Due to the quantum nature of light, an electron, which is bound in a solid and hit by monochromatic light of the energy $h\nu$, can absorb the energy of the incident photon as a whole. The process causes the excitation of the electron. If the transferred energy is high enough to overcome the binding energy E_B and the work function Φ, the electron may leave the solid and can be analyzed as a function of its kinetic energy E_{kin},

$$E_{kin} = h\nu - E_B - \Phi. \tag{2.8}$$

Due to the energy conservation principle, the binding energy of the electron E_B with respect to the Fermi level can thus be determined from a measurement of its external kinetic energy, provided that the initial photon energy and work function are known. Beyond this mere energy balance, the following sections deal with the various fundamental processes, which lead to the excitation and emission of photoelectrons in a ferromagnet.

2.2.1 The three step model

The common approach to describe the photoemission process is based on the so-called three-step-model, initially proposed by Berglund and Spicer [26]. This model represents a semiclassical treatment of the photoemission process, because it divides the underlying physical mechanism into three successive events. The steps are treated independently and are formulated by separate theoretical models. A non-approximative approach has to consider the photoemission process as an one-step event. The underlying theories provide the basis for one-step photoemission calculations, which yield spectra that can be compared to the experimental ones. However, such a treatment requires considerable computational

effort and has been carried out only for few selected examples. It turns out, that the simplified picture is usually more suitable for a quantitative interpretation of the experimental results. The successive events resulting in the three-step model are briefly outlined in the following paragraphs.

I. Interband transitions. The initial step in photoemission involves the excitation of an electron from an occupied state into an empty state above the vacuum level within the electronic bandstructure of the solid. In a single particle picture, the states are termed as initial and final states. The process follows the laws for energy and momentum conservation,

$$E_f = E_i + h\nu \quad \text{and} \quad \mathbf{k}_f = \mathbf{k}_i + \mathbf{G}. \tag{2.9}$$

By employing low photon energies in the ultraviolet regime (in this work: $h\nu \leq 40$ eV), the momentum of the incoming photon can be neglected, $\mathbf{k}_f = \mathbf{k}_i + \mathbf{k}_{ph} \approx \mathbf{k}_i$, and the transition can be viewed as taking place vertically at one particular $\mathbf{k}$ value within the reduced zone scheme. The photoexcitation is considered as the most important step during the photoemission process. The quantum mechanical description of this process as well as its extension towards the spin state of the electrons are discussed in more detail in chapters 2.2.2 and 2.2.3.

II. Transport to the surface. The transport of the excited photoelectrons towards the surface is accompanied by inelastic scattering events, which may change the electron's momentum. However, a direct relation between the momentum of the detected photoelectron and an interband transition inside the solid is only permitted for those electrons, which have not been scattered inelastically during their transport to the surface.

In the context of this work, an important aspect of the transport process concerns the fact, that the scattering processes limit the mean free path λ of the photoelectrons traveling within the solid. The mean free path thereby depends on the kinetic energy of the photoelectrons [51]. In this work, photon energies between 34 and 40 eV have been used for valence-band photoemission experiments. The inelastic mean free path for electrons with such kinetic energies is smaller than 10 Å, with equals 3-4 lattice constants of a $3d$ ferromagnet single crystalline sample. This short probing depth is a main prerequisite for photoemission experiments at surfaces and interfaces, as will be illustrated in chapter 5.

Taking into account the spin character of the transported photoelectrons, it has been shown that the inelastic mean free path can reveal an asymmetry for spin-up and spin-down electrons in ferromagnetic materials [27]. The scattering rate for minority spin electrons thereby is enhanced with respect to that of the majority spin electrons because of the excess of minority spin holes. However, the effect is mainly relevant for very low kinetic energies, i.e. below $E_{kin} = 5$ eV, if electrons scatter into the unoccupied d-states [28]. For electron energies above 30 eV, practically no spin-dependence of the inelastic mean free path can be observed (see Figure 5 in Ref. [27]).

III. Transmission and escape. The transmission of the escaping electrons through the surface involves a diffraction process at the potential barrier of the interface. This event changes the perpendicular component $\mathbf{k}_\perp$ of the wavevector $\mathbf{k}$. In the in-plane direction, in

contrast, the potential is periodic and the wave vector component $\mathbf{k}_\parallel$ is conserved modulo a reciprocal wave vector $\mathbf{G}_\parallel$.

This transmission step does not necessarily conserve the spin polarization of the photoelectrons. This is due to the fact, that every atom provides a scattering potential which includes spin-orbit contributions. Beside the exchange coupling, spin-orbit interactions represent a further spin-dependent interaction in a solid. The presence of spin-orbit coupling results in a spin-dependence of the diffraction process. The spin-dependent scattering changes the electron spin polarization upon transmission though the surface, if the emission direction does not equal that of the surface normal [29]. Since the photoemission experiments in this work have been performed in normal emission geometry, we can conclude, that the spin polarization is mainly preserved.

In the following sections, the mechanism, which actually leads to the excitation of spin-polarized photoelectrons from ferromagnets is discussed in more detail.

2.2.2 The photoexcitation process

The photoexcitation process is defined as the interband transition of an electron from an occupied (initial) state Ψ_i below the Fermi energy into an unoccupied (final) Ψ_f state above the vacuum level. The incident electromagnetic radiation causing this excitation can typically be considered as a small perturbation for the electron system of the solid. This allows for the theoretical description of the process in first order perturbation theory. Whereas the excitation and emission of one photoelectron reflects a single-particle process, the remaining $N-1$ electron system does not represent a ground state anymore and will respond to the perturbation. Formally, the involved initial and final states therefore have to be expressed as many-particle eigenfunctions $\mid \Psi_i\rangle$ and $\mid \Psi_f\rangle$.

The interaction of the photons with the N-electron system is derived from the non-relativistic Schrödinger equation. The ground-state Hamiltonian of the undisturbed solid, $H_0 = \mathbf{p}^2/2m - e\phi$, thereby has to be replaced by the operator of the disturbed system,

$$H = \frac{1}{2m}\left(\mathbf{p} + \frac{e}{c}\mathbf{A}\right)^2 - e\phi = \frac{1}{2m}\,\mathbf{p}^2 + \frac{e}{2mc}\left(\mathbf{A}\cdot\mathbf{p} + \mathbf{p}\cdot\mathbf{A}\right) + \frac{e^2}{2mc^2}\mid \mathbf{A}\mid^2 - e\phi, \qquad (2.10)$$

with $\mathbf{A}(\mathbf{r},\mathrm{t})$ denoting the vector- and ϕ the scalar potential of the electromagnetic field. The quadratic term describes two electron processes, which can be neglected. Using the Coulomb gauge $\nabla\cdot\mathbf{A} = 0$, we have $[\mathbf{A},\mathbf{p}] = 0$, and the Hamiltonian can be rewritten as

$$H = \frac{1}{2m}\,\mathbf{p}^2 + \frac{e}{mc}\mathbf{A}\cdot\mathbf{p} - e\phi. \qquad (2.11)$$

In the energy regime in question ($h\nu \leq 40$ eV), the wavelength λ of the light (~ 300 Å) is always much larger than the atomic distances in a solid. The vector potential $\mathbf{A}$ is therefore assumed to be spatially constant $\mathbf{A}(\mathbf{r},\mathrm{t}) = \mathbf{A}_0(\mathrm{t})$ in surface regions of the solid, where the photoelectrons come from. This leads to the dipole approximation of the perturbation,

$$\Delta H = \frac{e}{mc}\,\mathbf{A}_0\cdot\mathbf{p}, \qquad (2.12)$$

if external electrostatic potential contributions ϕ are ignored.

In the photoexcitation process, each particular transition of a photoelectron between the initial and final eigenstate contributes to the total photocurrent $I(h\nu)$. The latter is proportional to the transition probability w according to Fermi's Golden Rule,

$$I(h\nu) \propto w \propto |\langle \Psi_f | \Delta H | \Psi_i \rangle|^2 \, \delta(E_f^N - E_i^N - h\nu), \tag{2.13}$$

where the δ function guarantees the energy conservation of the process. So far, the formalism comprises many-particle eigenstates of the N-electron system. In order to reduce the complexity of this approach, the so-called sudden approximation is usually applied. It assumes a nearly negligible interaction between the photoelectron and the remaining $N-1$ electron system during the excitation. In principle, this means neglecting many-body correlation effects between the photoelectron hole state and the interacting $(N-1)$ electron system. Hence, the eigenstates can be expressed in terms of one-electron states $|\psi_i\rangle$ and $|\psi_f\rangle$. The photocurrent then has to be summed over all possible initial and final states

$$I(h\nu) \propto \sum_{i,f=1}^{N} I(h\nu, E_i, E_f) \propto |\langle \psi_f | \Delta H | \psi_i \rangle|^2 \, A_i \; (E_f - h\nu). \tag{2.14}$$

The term A_i is called the spectral function of the hole state and contains the correlation effects of the interacting many-body system [32]. These correlation effects are often expressed by means of a complex self-energy $\sum(h\nu, E_i)$ of the hole state. In this case, the spectral function becomes

$$A_i(E_f - h\nu) \propto \frac{\mathrm{Im} \sum(h\nu, E_i)}{[h\nu - E_i - \mathrm{Re} \sum(h\nu, E_i)]^2 + [\mathrm{Im} \sum(h\nu, E_i)]^2}, \tag{2.15}$$

where $\mathrm{Re} \sum(h\nu, E_i)$ and $\mathrm{Im} \sum(h\nu, E_i)$ denote the real and imaginary part of the self-energy, respectively. This correction results in a broadening and energy shift of the peak observed in a non-interacting single-particle picture. If the correlation effects can be neglected, the self-energy corrections $A_i(h\nu, E_i)$ reduce to a series of δ functions. Finally, the expression for the excitation process in a one-electron picture can be expressed by

$$I(h\nu) \propto |\langle \psi_f | \mathbf{A}_0 \cdot \mathbf{p} | \psi_i \rangle|^2 \, \delta(E_f - E_i - h\nu). \tag{2.16}$$

The strength of each transition is determined by the dipole matrix element $m = |\langle \psi_f | \mathbf{A}_0 \cdot \mathbf{p} | \psi_i \rangle|^2$, which also decides whether a photoelectron transition can take place (see section 2.2.2). The energy conservation leads to particular transitions between initial and final states, obeying $h\nu = E_f - E_i$, within the bandstructure of the solid. This energy balance has to be distinguished from the energy conservation in equation (2.8), since in the present case the electron has not yet left the crystal. The interband transitions, which lead to the spectral features observed in the photoemission experiment, can be compared to the dispersion relation $E(\mathbf{k})$ obtained by a theoretical band structure calculation (see chapter 2.2.4). It has to be taken into account, that the band structure calculations are usually carried out for the ground state, i.e. $T = 0$ K, whereas the experiment is performed at room temperature. Moreover, the photoemission process probes the excited electron system and not the undisturbed ground state. Although the comparison between experiment and theory yields correct results, a perfect agreement can usually not be expected. In particular, the intensity of the photoelectron transitions, i.e. their spectral weight, is not accessible in this qualitative approach. In an extended analysis, the photoemission intensities may be modeled by a one-step photoemission calculation.

Symmetry selection rules

The intensity of each particular photoemission process as well as the probability of the latter are contained in the one-electron dipole matrix element $m = |\langle\psi_f|\mathbf{A}\cdot\mathbf{p}|\psi_i\rangle|^2$. The matrix element introduces dipole selection rules since both the electronic states and the field operator have a well-defined symmetry. A non-vanishing matrix element m gives rise to an optical excitation process and determines uniquely the symmetry of the states that are involved in a direct interband transition [30, 31].

The symmetry of the final state $|\psi_f\rangle$ is defined by the emission geometry of the experiment. In case of a normal emission along one of the three high-symmetry directions (001) (Δ), (110) (Σ) and (111)(Λ), the final state must possess the same symmetry as the outgoing spherical wave and thus has to be totally symmetric relative to the surface normal $\mathbf{n}$ [30]. The experiments in the present work have been carried out on (001) surfaces. In the corresponding Brillouin zone, this line is denoted as $\Delta = \Gamma - \mathrm{H}$ and has a C_{4v} symmetry (see chapter 2.1.3). The group C_{4v} consists of four irreducible representations, which are written as $\Delta_1, \Delta_2, \Delta_{2'}$ and Δ_5. This requires that the excitation takes place into a Δ_1 final state, which posses the highest symmetry among the operations of the C_{4v} point group, coming closest to a free-electron state.

A non-vanishing dipole element m implies, that the symmetry of the field operator and the initial state cannot be chosen independently. In fact, the dipole operator must have the same symmetry as the initial state in order to observe an allowed optical transition [32]. This practically restricts the possible initial states to Δ_1 and Δ_5 for the (001) surface, if the orientation of the field operator is normal ($A\cdot\mathbf{p} \parallel \mathbf{n}$) or parallel ($A\cdot\mathbf{p} \perp \mathbf{n}$) to the surface, respectively. The complete set of dipole selection rules along the Δ-line is given in Table 2.2.2. It is remarked, that the irreducible representations of the initial and final states are listed in the non-relativistic single group notation. A rigorous specification would require the relativistic double group notation, which takes into account also relativistic effects due to spin-orbit coupling.

Spin-orbit coupling is present in all materials, but its influence increases for heavy elements, since it strongly depends on the atomic number Z. Usually, the presence of spin-orbit interactions can already not be neglected for the $3d$ or $4f$ transition metals. A special case, however, is found for the $3d$ ferromagnets Fe and Co. Here, the spin-dependent interaction mechanisms are dominated by the exchange interaction of the itinerant electrons (see chapter 2.1.1), because its influence is significantly larger than that of spin-orbit coupling[1]. This reduces the effects to hybridization between electronic bands at particular crossing points [22]. It is therefore widely accepted to neglect the relativistic effect in these materials.

2.2.3 Spin-resolved photoemission from ferromagnets

So far, the spin character of the photoelectrons is not taken into account within the model of the photoexcitation process as presented in section 2.2.2. In a ferromagnet, however, the electronic wavefunctions depend not only on the spatial, but also on the spin coordinate

[1] For the $3d$ electrons in ferromagnets, the band splitting due to the exchange interaction is about 1 eV, whereas the spin-orbit coupling is of the order of 0.1 eV [42].

Initial state	Final state	Polarization
Δ_1	Δ_1	$A \cdot \mathbf{p} \perp \mathbf{n}$
Δ_2		-
Δ_2'		-
Δ_5		$A \cdot \mathbf{p} \parallel \mathbf{n}$

Table 2.1: Dipole selection rules for optical transitions along the Δ line in cubic systems (normal emission). The orientation of the light polarization $A \cdot \mathbf{p}$ with respect to the surface normal $\mathbf{n}$ decides whether a particular initial state symmetry can be observed in a direct interband transition.

$\psi = \psi(\mathbf{r}, \sigma)$. In a rigorous formal treatment, the two spin-dependent interactions, i.e. the exchange interaction and the spin-orbit coupling, would enter the Hamiltonian (2.10), asking for a Dirac description. As discussed in the previous section, we can approximately neglect the relativistic effects in terms of spin-orbit interaction for the $3d$ ferromagnets Fe and Co. The non-relativistic Schrödinger equation, with the Hamiltonian being augmented by the exchange interaction H_{xc}, thus still represents a meaningful description of the photoelectron transitions [27].

As has been discussed in chapter 2.1.2, the presence of the exchange interaction in ferromagnets lifts the energetic degeneracy between spin-up and spin-down bands and separates them by the exchange splitting Δ_{xc}. In the absence of spin-orbit coupling in Fe and Co, the exchange interaction is viewed to act only on the spins, but not on the spatial part of the wavefunction. Thus, according to the Stoner model, the exchange splitting results in two individual electronic structures for spin up and spin down electrons $E(\mathbf{k}, \uparrow)$ and $E(\mathbf{k}, \downarrow)$, which can be treated separately.

In this model, the excitation of photoelectrons yields interband transitions, which take place in the subbands of either majority or minority character (see Figure 2.4). Due to the energetic splitting of the initial and final states, the transitions take place at different $\mathbf{k}$ values. It is assumed, that the spin orientation is conserved during this process. Thus, the total photocurrent is composed of majority and minority spin contributions according to

$$I(h\nu) \sim \sum_{i,f,s_i,s_f} |\langle \psi_f | H | \psi_i \rangle|^2 \, \delta(\epsilon_f - \epsilon_i - h\nu) \, \delta_{s_i,s_f}. \tag{2.17}$$

The introduction of the spin component has no influence on the transition probability of the photoexcitation. Since the dipole operator acts only on the spatial part of the wave function and is not coupled to the spin component, the dipole selection rules can be applied in the above sense of a single-group representation (see chapter 2.2.2). The particular irreducible representation is thus simply expanded by an index for the particular spin direction.

In the spin-resolved photoemission experiment, the transitions of spin-up and spin-down electrons lead to separate features in an integrated photoemission spectrum. A spin-analysis yields the spin-polarization of the photoelectrons from the ferromagnetic electronic structure, if the spin components are aligned along a quantization axis, which by convention is provided by the magnetization direction of the sample. Therefore, the spin-resolved photoemission experiments require remanently magnetized samples, with the photoelectrons

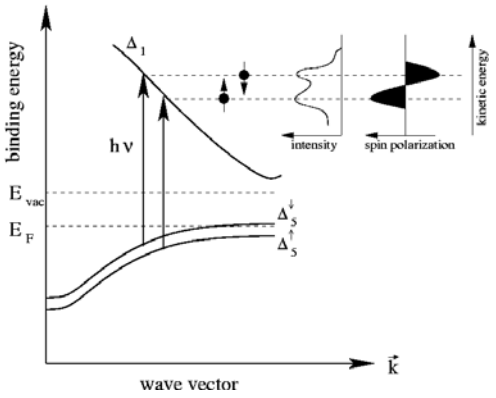

Figure 2.4: Photoexcitation process in a ferromagnet. The electronic bands are spin-split due to the exchange interaction $E^{\uparrow}(\mathbf{k}) \neq E^{\downarrow}(\mathbf{k})$. The interband transitions give rise to spectral features, with the spin polarization being detected simultaneously.

ideally originating from a single domain state in order to reveal the actual spin character of the spin-split electronic bands.

According to the above considerations, the spin integrated photoelectron intensity $I(E)$ contains the sum of all spin-up and spin-down contributions $I^{\uparrow}(E)$ and $I^{\downarrow}(E)$. By additionally measuring the spin polarization spectrum $P(E)$, the necessary quantities to analyze a spin-resolved photoemission spectrum are at hand. The spin polarization P is defined as the normalized quantity

$$P(E) = \frac{I^{\uparrow}(E) - I^{\downarrow}(E)}{I^{\uparrow}(E) + I^{\downarrow}(E)}. \tag{2.18}$$

As the spin polarization is an immanent quantity of the electronic system, the spin-polarization of the transitions should yield a value of $P = 100\%$. In an real experiment, however, the actual spin polarization is usually lower, because the remanent magnetization of the sample does not necessarily coincide with the saturated magnetization of a single domain. Beside, thermal and electron correlation effects as well as spin-orbit coupling can lead to a certain overlap of the spectral features, which reduces the spin polarization, too.

The so-called partial intensities $I^{\uparrow}$ and $I^{\downarrow}$ are obtained from the spin-integrated intensity $I(E)$ and the spin polarization spectrum $P(E)$ according to the equations

$$I^{\uparrow} = \frac{1}{2} I(E)\,(1 + P(E)) \quad \text{and} \quad I^{\downarrow} = \frac{1}{2} I(E)\,(1 + P(E)). \tag{2.19}$$

The technical details on the spin detection process and data acquisition are discussed in chapter 3.4. By coupling the spin-polarized photoemission to its angle-resolved counterpart, the experiment finally yields all observables of the electronic state of a ferromagnet, i.e. the binding energy E, the wavevector $\mathbf{k}$ and the spin character σ.

2.2.4 Basic ideas of spin-density functional theory

A common approach to interpret photoemission results is to compare the spectral features to *ab initio* bandstructure calculations. The latter are performed in the framework of density functional theory, which was developed by Hohenberg and Kohn in 1964 [33]. Its success relies on the idea, that instead of solving the many-particle Schrödinger equation for a solid by $3N$-dimensional electron wave functions $\Psi(\mathbf{r}_1, ..., \mathbf{r}_N)$, the complexity of the problem can be significantly reduced by determining the 3-dimensional electron density $n(\mathbf{r})$. This step enables one to calculate large electronic systems. The theoretical determination of the electronic structure is based on *ab initio* considerations, i.e. the calculations are carried out without assuming parameters derived from experiments, just on the basis of the underlying fundamental physical laws. Despite the exact mathematical description, the final solution of the problem in practice requires the application of suitable approximations.

The fundament of DFT is based on the theorem by Hohenberg-Kohn, which states that the ground state energy E of a many electron system can be uniquely expressed as a functional of the electron density $n(\mathbf{r})$. It is proved, that minimizing the functional $E[n(\mathbf{r})]$ yields the exact ground state energy [34].

The energy functional contains three contributions, a kinetic energy T_s of independent electrons, a Coulomb energy U due to the electrostatic interactions between the charged particles in the system and a term called exchange-correlation energy V_{xc}, that captures all many-body interactions,

$$E[n(\mathbf{r})] = T_s[n(\mathbf{r})] + U[n(\mathbf{r})] + V_{xc}[n(\mathbf{r})]. \tag{2.20}$$

In an approach by Kohn and Sham [35], the problem can be reformulated and expressed in terms of single-particle wave functions $\psi_i(\mathbf{r})$ and corresponding single-particle Schrödinger equations

$$\left(-\nabla^2 + V_{eff}\right)\psi_i(\mathbf{r}) = \epsilon_i \psi_i(\mathbf{r}) \quad \text{with} \quad n(\mathbf{r}) = \sum_{i=1}^{N} |\psi_i(\mathbf{r})|^2. \tag{2.21}$$

By this approach, the ground state energy can be found by solving an effective single-particle problem with an effective potential V_{eff}, instead of addressing the $3N$-dimensional problem.

The formalism can be extended to the spin-polarized DFT by introducing the magnetization $m(\mathbf{r})$ as a second independent quantity besides the electron density $n(\mathbf{r})$. The total electron density is given by the sum of majority $n(\mathbf{r})^{\uparrow}$ and minority $n(\mathbf{r})^{\downarrow}$ spin densities according to

$$n(\mathbf{r}) = n^{\uparrow}(\mathbf{r}) + n^{\downarrow}(\mathbf{r}) \quad \text{and} \quad m(\mathbf{r}) = \mu_B(n^{\uparrow}(\mathbf{r}) - n^{\downarrow}(\mathbf{r})). \tag{2.22}$$

The Kohn-Sham equations in (2.21) are then expressed in terms of the spin dependent single-particle wave functions $\psi_i^{\uparrow,\downarrow}(\mathbf{r})$ and energy eigenvalues $\epsilon_i^{\uparrow,\downarrow}(\mathbf{r})$. The spin-dependence is completely included in the exchange-correlation potential $V_{xc}^{\uparrow,\downarrow}$.

The only quantity of the energy functional, which is not exactly known, is the exchange-correlation energy. In a mean field approximation, the functional is replaced by the energy of a homogenous, spin-polarized electron gas with a constant spin density $n^{\uparrow,\downarrow}$. This is the so-called local spin-density approximation (LSDA), which yields good results for many ground-state properties and a good agreement with experimental results especially for

metallic materials. Although the energy eigenvalues, which are obtained by the calculations are not identical with the single-particle energies, the resulting band structures agree well with experimental data, e.g. obtained by a photoemission experiment.

In practice, the Kohn-Sham equations have to be solved iteratively. Many *ab initio* methods are based on efficient basis sets for the single-particle wave function $\psi_i(\mathbf{r})$, which solve the Kohn-Sham equations. Another possibility is to solve the Kohn-Sham equations for the single-particle Green's function, which contains the complete information about the electronic system. In this so-called KKR[2] approach, the electronic structure is viewed as the stationary state of the multiple diffraction of the wave functions at the atoms, or in other words, at the effective potentials of the Kohn-Sham equations. Within the Green's function approach, the electronic system is divided into a contribution related to the free electron gas ($H_0 \sim -\nabla^2$) and an inhomogeneity, which is described by the effective potential V_{eff}.

In the case of relativistic ferromagnets, both the exchange interaction and spin-orbit coupling enter the description in sophisticated fully-relativistic formalisms (SPR[3]). This is done in the framework of the Dirac equation, instead of the Schrödinger equation. In analogy to the non-relativistic calculations, the relativistic formulation leads to a set of relativistic Kohn-Sham equations, which have to be solved to find the ground state energy. The relativistic calculations reveal the increased complexity of the electronic bands, if the influence of spin-orbit coupling is large. If the formalism is applied on materials with negligible spin-orbit coupling, however, the electronic structures resemble that obtained by conventional spin-polarized DFT.

2.3 Electronic structure and spin polarization in FM/I systems

In this final part of the chapter, the fundamental relation between the ferromagnetic electronic structure and the phenomenon of spin dependent transport (SDT) is discussed. The main parameter in SDT is the spin polarization of the electric current, which e.g. gives rise to the tunneling magnetoresistance (TMR) effect in magnetic tunnel junctions. It turns out, that the tunneling spin polarization is determined by the electronic properties of the ferromagnet-insulator (FM/I) interface. In order to draw a comprehensive picture of the physics involved, we will approach this issue from the angle of the electronic structures of ferromagnet and insulator. The proper definition of a transport spin polarization is a major difficulty, since it relates properties of the spin-split electronic structure to the transport properties of the electric current. It is important to clearly distinguish the origin of the transport polarization from that of the ground state polarization of a bulk ferromagnet. Moreover, the tunneling spin polarization (TSP) in a tunnel junction is affected by more sophisticated mechanisms: By taking into account the particular symmetries of the coupling electronic wavefunctions at the FM/I interface, the slowest decaying wavefunctions will give rise to sign and magnitude of the TSP. Nevertheless, the wavefunction matching reacts very sensitive to any modification of the electronic structure at the FM/I interface.

[2]KKR: Korringa-Kohn-Rostoker
[3]SPR: spin-polarized relativistic

Both experiments and theory highlighted the role of interface bonding, which can result in strong modifications of the tunneling spin polarization. Although the oxidized FM/I interface is known as acting detrimental on the TSP of a tunnel junction, up to now only little attention has been paid to another interface imperfection, which considers the degree of oxidation of the oxide barrier.

2.3.1 Spin dependent transport

Although the notion of a spin polarization of a ferromagnet is frequently used in the context of this thesis, in fact it is not equivalent to the spin polarization of an electrical current, which denotes how many different spins contribute to the transport. The transport spin polarization thereby mirrors the spin-split electronic structure of a ferromagnet, but cannot be expressed in terms of equation (2.7), which is the unique definition for the polarization of the ferromagnetic ground state. Spin polarized electron transport occurs e.g. in the current through a bulk ferromagnet, in a current crossing a ferromagnet/nonmagnetic metal interface or in the current which is tunneling through an insulating barrier in a tunnel junction. The spin polarization of an electric current is defined as the imbalance of spin up and spin down electrons according to

$$P_j = \frac{j^{\uparrow} - j^{\downarrow}}{j^{\uparrow} + j^{\downarrow}}, \tag{2.23}$$

with $j^{\uparrow}$ and $j^{\downarrow}$ denoting the separate spin-up and spin-down contributions to the total current density, respectively. Equation (2.23) is the general definition of a transport spin polarization and applies to any electrical current.

Spin dependent transport in bulk ferromagnets

In the simplest case of spin polarized electron transport in a bulk $3d$ ferromagnet, the current is carried by the itinerant conductance electrons just at the Fermi level. In this case, the current density j can be supposed to be proportional to the density of states $D(E_F)$ at the Fermi level. This aspect may be incorporated in the Drude model, which is a suitable description for nearly free electron systems, and yields a current density

$$j \propto \frac{D(E_F)\, e^2\, \tau}{m_{\text{eff}}} \cdot E, \tag{2.24}$$

with e being the electron charge, τ the electron-lattice scattering time and m_{eff} the effective electron mass. Thus, substituting equation (2.24) into (2.23) yields an approximate spin polarization of a current flowing in a ferromagnetic bulk material

$$P_t \propto \frac{D^{\uparrow}(E_F)/m_{\text{eff}}^{\uparrow} - D^{\downarrow}(E_F)/m_{\text{eff}}^{\downarrow}}{D^{\uparrow}(E_F)/m_{\text{eff}}^{\uparrow} + D^{\downarrow}(E_F)/m_{\text{eff}}^{\downarrow}}. \tag{2.25}$$

This basic derivation underlines the fact, that spin-dependent transport phenomena usually are *not* defined solely by the spin-split DOS $D(E_F)$ of the ferromagnetic ground state. If this was the case, the transport polarization P_t for the $3d$ ferromagnets would reveal a positive sign ($P_t > 0$) for Fe on the one hand, and a negative sign ($P_t < 0$) for Co and

Ni on the other hand. This is due to the fact, that in Fe the DOS in the vicinity of the Fermi level is dominated by spin up contributions, whereas in Co and Ni we find larger contributions from the spin down electrons close to E_F (see chapter 2.1.2). An information on the transport polarization originating from a ferromagnet can be obtained by an experiment proposed by Tedrow and Meservey [36]. In this setup, one measures the tunneling currents for both spin polarizations at a ferromagnet/superconductor contact[4]. A detailed overview on the method is given in [36]. These experiments show, that the transport spin polarizations for Fe, Co and Ni actually have a positive sign [36], in contrast to their ground state polarizations. This finding suggests, that the effective mass m_{eff} and its spin dependence cannot be neglected, as it is indicated in equation (2.25). By translating the concept of an effective mass into terms of the ferromagnetic electronic bandstructure,

$$\frac{1}{m_{\text{eff}}^{\sigma}} = \frac{1}{\hbar^2}\frac{d^2E^{\sigma}}{d^2k}, \tag{2.26}$$

the inverse effective mass represents the curvature of the dispersion $E(\mathbf{k})$ of the spin-split ferromagnetic bands ($\sigma = \uparrow, \downarrow$). The positive sign of the measured transport polarization P_t according to [36] implies, that spin-up electrons are transported more efficiently and mainly carry the spin-polarized current in a bulk ferromagnet. By considering the current flowing e.g. in (001) direction of the ferromagnetic crystal, a view into the corresponding band structures $E(\mathbf{k}, \sigma)$ in Figure 2.2 gives further insights. In a rough approximation, the Δ_1 states are supposed to possess the lowest effective mass of all majority states due to their strong delocalized character. Although this simple picture completely neglects the $\mathbf{k}$-dependence of the spin-polarized current, one may nevertheless conclude, that the spin-polarized transport in ferromagnets can basically be considered as being dominated by 'light s-electrons'. This gives rise to a positive transport spin polarization, which actually does not equal that of the intrinsic ferromagnetic ground state.

Spin dependent tunneling in magnetic tunnel junctions

The phenomenon of spin dependent transport is also widely exploited in magnetic tunnel junctions (MTJs). A MTJ consists of two ferromagnetic layers (electrodes), which are separated by a thin insulating layer. It was discovered by Tedrow and Meservey [36], that the tunneling current reveals a spin imbalance between spin-up and spin-down electrons. The spin polarization of this tunneling current gives rise to the tunnel magnetoresistance (TMR) effect, i.e. the resistance R of the junction depends on whether the electrodes have a parallel (p) or antiparallel (a) magnetization, and is defined as

$$\text{TMR} = \frac{R_a - R_p}{R_p} = \frac{j_p - j_a}{j_p}. \tag{2.27}$$

In view of the high technological relevance of the TMR effect, it is desirable to theoretically understand the origin of the tunneling spin polarization in these devices. In fact, the transport mechanisms, which are responsible for a spin-polarized tunnel current in a MTJ

[4]By determining the spin polarization at a ferromagnet/superconductor (FM/SC) contact, not the intrinsic transport polarization of the bulk ferromagnet is measured, since the interface can modify this parameter, as will be shown in the following section.

or the spin-polarized current in a bulk ferromagnet are different in nature. In a MTJ, the complexity of the transport process is enlarged, because the conduction electrons face the insulator as a potential barrier. Only those electrons, which can pass through the barrier with a high probability will contribute to the tunneling current. The tunneling spin polarization (TSP) in a MTJ thus may be considerably changed in contrast to that of a current in a bulk ferromagnet.

Recalling the considerations from above, it seems not very conducive for a further understanding to relate the TSP to the density of states $D(E_F)$ of the ferromagnetic electrodes. This, however, is done in a model proposed by Jullière, who suggested that the tunneling probability and current are proportional to $D(E_F)$ [11]. Jullière's model predicts that

$$\mathrm{TMR} = \frac{2P'^2}{1+P'^2}. \tag{2.28}$$

The main shortcoming of this model is, that it is not clear how the polarization P' should be defined. As has been shown, the ground state polarization of the ferromagnetic electrodes does not represent a meaningful quantity for this purpose. However, the model in many cases can explain the experimental trends, if the values for the ground state polarization are already known. If e.g. the tunneling polarizations obtained in [36, 37] are used for equation (2.28), the calculated values of the TMR ratio are in agreement with experimental values[5] [5]. It has to be kept in mind, however, that any coincidence of the magnitude of TMR with equation (2.28) seems to be rather accidental than systematic.

In order to clarify the physical meaning of the tunneling spin polarization in MTJs, it was soon recognized that the properties of the insulating barrier have to be taken into account. Pioneering results by de Teresa *et al.* indicated, that the tunneling polarization of a MTJ is not only determined by the properties of the ferromagnet but also by the particular insulating material itself [14]. This is a consequence of the fact, that the tunneling conductance depends not only on the number of electrons at the Fermi level, but also on the tunneling probability, which is different for various ferromagnetic electronic states and symmetries in single-crystalline barriers. This aspect is elucidated in the following section, which approaches the issue on the basis of the electronic structures of ferromagnet and insulator.

2.3.2 Bandstructure and TMR

An improved approach to the understanding of SDT in tunnel junctions is provided by theoretical studies, which state that the spin dependence of the tunneling current can be deduced from the symmetry of the electronic states of the bulk ferromagnetic electrode and the complex band structure of the insulator [12, 13]. By identifying those bands of the ferromagnet, which couple as evanescent states and decay most slowly within the barrier, one can draw conclusions on the sign and magnitude of the spin polarization of the tunneling current. For technical reasons, the theoretical formulations are always based on perfectly epitaxial junctions. Largely related to the topic of this thesis are the systems

[5] Actually, the polarization measured in a tunnel junction does not equal that obtained from a FM/I/SC experiment. This is due to the fact, that every interface is supposed to influence the TSP.

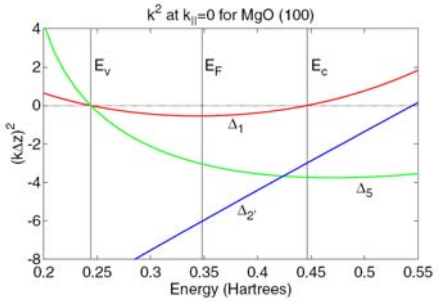

Figure 2.5: The electronic states of different symmetries (Δ_1, Δ_5 and $\Delta_{2'}$) decay with different rates within the MgO barrier in $\mathbf{k}_\parallel = 0$ direction. Actually, the Δ_1 state reveals the smallest decay rate and is therefore supposed to carry the tunneling current in the barrier. From [10].

	(100)
Fe ↑	Δ_1, $\Delta_{2'}$,Δ_5
Fe ↓	Δ_2, $\Delta_{2'}$, Δ_5
Co ↑	Δ_1
Co ↓	Δ_1, Δ_5

Table 2.2: Symmetries of the Bloch states with $\mathbf{k}_\parallel = 0$ near E_F for Fe and Co for the (001) crystal face. The corresponding orbital symmetry of these bands are $\Delta_1(s,p,d)$, $\Delta_5(p,d)$ and $\Delta_2(d)$.

bcc-Fe(100)|MgO(100)|Fe(100) and bcc-Co(100)|MgO(100)|Co(100), which are therefore considered exemplarily in more detail.

In order to identify those ferromagnetic bands, which are mainly involved in the tunneling process within the barrier, it is not necessary to examine the whole DOS $D^{\uparrow}(E_F)$ and $D^{\downarrow}(E_F)$, as is predicted in Jullières model. Instead, one has to find the wavevector $\mathbf{k}$ in the electronic bandstructure, at which the exponential decay of the electronic states inside the barrier will be the less fast compared to others[6]. It was found, that the exponential decay parameter $\kappa = \kappa(\mathbf{k}_\parallel)$ is minimal for the direction $\mathbf{k}_\parallel = 0$ [10].

In the following, one has to identify the states in the ferromagnetic electrodes which exist at $\mathbf{k}_\parallel = 0$, because these states will couple to states in the (MgO) barrier with a minimal decay rate $\kappa_{\min} = \kappa\,(\mathbf{k}_\parallel = 0)$. The symmetry of the incident electronic states of the ferromagnetic electrode is conserved during tunneling through the barrier as evanescent states [13]. As discussed in chapter 2.1.3, there are electronic states with symmetries Δ_1, Δ_5 and $\Delta_2^{'}$ for the majority and Δ_2, Δ_5 and $\Delta_2^{'}$ for the minority bands around the Fermi level for cubic bcc crystals in the (001) direction. It was proposed, that the slowest decaying

[6]In the case of a perfect FM/I interface, the wavevector $k_\parallel$ is conserved during the scattering at the interface.

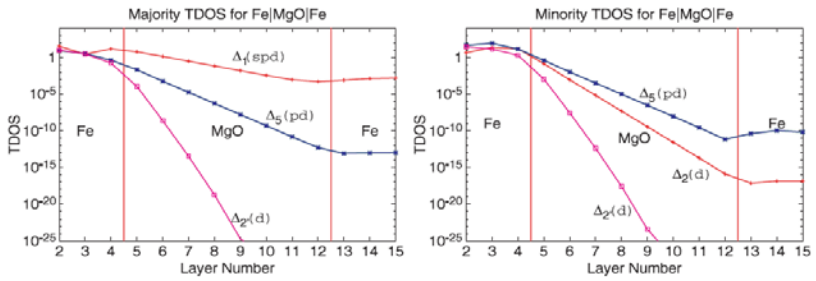

Figure 2.6: Tunneling DOS for $\mathbf{k}_{\parallel} = 0$ in a Fe/MgO/Fe(001) junction, in which the magnetization of the FM electrodes is aligned parallel. The Δ_1 majority state decays most slowly inside the MgO barrier and thus contributes dominantly to the tunnel current. From [10].

evanescent Bloch state in the barrier is typically the one with the highest symmetry [10]. As a consequence, the slowest decay rate is expected for electronic states, which posses a Δ_1 symmetry.

As an illustration of these considerations, Figure 2.5 shows the electronic Bloch states with different symmetries and decay rates within the insulating MgO barrier [10]. Here, k^2 represents the Bloch state quasi-momentum in the complex MgO bandstructure, which is plotted as a function of the energy for states traveling in the (100) direction. The negative values of k^2 determine the strength of the exponential decay rate for the tunneling states. E_v labels the top of the MgO valence band and E_c is the bottom of the conduction band. Whereas the valence band is a combination of Δ_1 and Δ_5 states, the conduction band is a pure Δ_1 state. Obviously, it is the Δ_1 state, which propagates through the MgO gap as an evanescent state with a relatively small (negative) value of k^2 and thus reveals the slowest decay rate among all participating states.

As mentioned above, both bcc Fe(100) and bcc Co (100) have the property of a high symmetry Δ_1 state at $\mathbf{k}_{\parallel} = 0$ for the majority states, but not for the minority states. This is due to the strong exchange splitting between the $\Delta_1^{\uparrow}$ and $\Delta_1^{\downarrow}$ bands. Since only the $\Delta_1^{\uparrow}$ band crosses the Fermi level, this leads to a spin selection of the tunneling current: Figure 2.6 illustrates, that the Δ_1 majority conductance is larger compared to all other symmetries in a Fe/MgO/Fe tunnel junction. However, also small contributions from $\Delta_5^{\uparrow}$ for $\mathbf{k}_{\parallel} = 0$ can be observed, which leads to moderate TMR values in Fe-based junctions [8]. For a bcc Co(001)-based electrode, an even higher magnetoresistance ratio is supposed in contrast to Fe-based electrodes [7]. This is due to the fact, that Co(001) has only one single majority state in (001) direction and this state is of Δ_1 symmetry (see Table 2.3.2). This has the consequence of an enhanced spin-filtering effect, because the Δ_5 tunneling channel is completely suppressed. These arguments go along with very recent experiments on Co-based MTJs, which reported on extraordinary high TMR ratios [40].

The symmetry arguments for the electronic states explain nicely the large values of TMR predicted for epitaxial Fe/MgO/Fe and Co/MgO/Co junctions [9, 10]. The main

improvement in the understanding of SDT is given by the idea, that the spin polarization in a MTJ is mainly controlled by the electronic structure of the ferromagnet and the insulator. The compatibility of spatial symmetries decides, which ferromagnetic wavefunctions are able to couple efficiently into the insulating barrier. This spin-filtering effect is held responsible for the actual magnitude and sign of the spin polarization of the tunneling current.

Although these findings are of high relevance for the recent understanding of SDT in tunnel junctions, these symmetry considerations apply to pure bulk materials only. This is not always sufficient to predict the tunneling spin polarization, because the theoretical studies are based on perfectly sharp and well-ordered interfaces, which are hardly realized experimentally. It was thus soon considered as critical to take into account the electronic structure of ferromagnet/barrier interfaces, which reveal modifications of the FM/I interface electronic structure.

2.3.3 Beyond simple FM/I/FM model systems

The electronic structure of ferromagnet and insulator determines, how effective electrons are transmitted across the interface, with the transmission probability being different for electrons of different orbital character or symmetry. It is reasonable to assume, that every modification of the FM/I interface results in changes of the tunneling process, i.e. of sign and magnitude of the TSP and magnetoresistance. One can imagine a variety of interface imperfections, among which are the oxidation of the ferromagnetic electrode, the presence of interface roughness or a deviating or defective oxide stoichiometry. In the context of this thesis, we will mainly focus on the aspect of the electronic structure at the FM/I interface due to modifications of the chemical bonding. Two realistic situations of modified FM/I interfaces are exemplarily discussed in the following.

The oxidized FM/I interface

It is obvious, that an FeO layer may form at the interface between Fe and MgO, when MgO is deposited onto a Fe(001) surface. Since this aspect was proven experimentally by Meyerheim *et al.* [16], the question arises, whether this modification is the reason for the differences between the calculated TMR ratios and the lower ones observed in experiments. Indeed, it is shown theoretically, that an FeO intralayer has a detrimental effect on the spin-polarized tunneling process, because it reduces the tunneling current of the majority spins [15].

This reduction is mainly ascribed to the modification of the interface bonding. It has been shown in the previous section, that the dominant contribution to the tunneling conductance arises from the Δ_1 majority state, since this state is able to couple most efficiently to the complex MgO bandstructure. In order to clarify the actual bonding mechanism for the Δ_1 states in the case of a Fe-O interlayer, the partial Δ_1 density of states in the interface region is calculated for a sharp Fe/MgO interface and a Fe/FeO/MgO system, in which O atoms have been introduced into the bcc-hollowsites of the Fe top layer [15]. Figure 2.7 (b) shows, that in the case of a non-disturbed interface, the Δ_1 DOS is concentrated vertically between the Fe and on-top oxygen sites. This leads to an

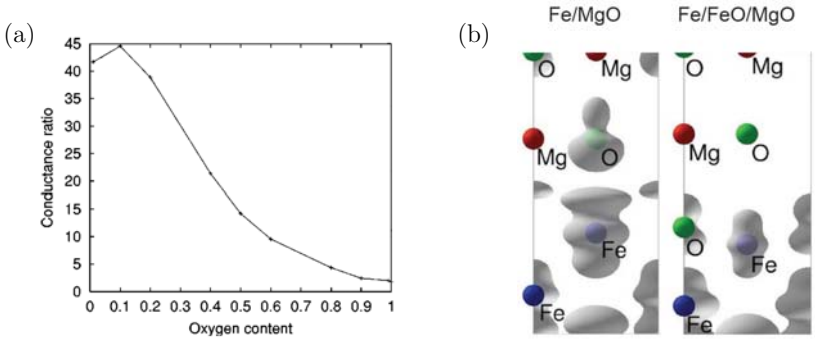

Figure 2.7: (a) Tunneling conductance of a Fe/FeO/MgO junction as a function of the O composition in the interface FeO layer. (b) Partial density of states for the Δ_1 majority states in the interface region for an ideal Fe/MgO interface and an oxidized Fe/FeO/MgO system [38].

orbital overlap, which is the main reason for the strong coupling of Δ_1 wavefunctions to the MgO barrier. The situation is different for the Fe/FeO/MgO system: Here, the Δ_1 electron density is strongly reduced in comparison to Fe/MgO and is basically concentrated horizontally within the Fe-O plane. Since the Fe-O bonds are mainly composed of s, p-like electrons, the d-like electrons are not affected by the presence of the O atoms of the FeO layer. Thus, the impact of the Fe-O bonds on the majority spin tunneling is much larger than on the minority spin current. Indeed, the reduction of the Δ_1 partial density of states results in a reduction of the tunneling conductance as a the function of the oxygen concentration in FeO, which is shown in Figure 2.7 (a). In contrast to the weakly interacting Fe/MgO system, the changed bonding in the Fe/FeO/MgO involves a charge transfer between the Fe atom and the O atom within the FeO layer [15]. It was found, that a significant magnetic moment is transferred on the O sites of the FeO layer, which indicates a strong hybridization between the O atoms and the neighboring Fe atoms.

Oxygen deficiency in FM/I/FM systems

By taking the opposite view of a strongly modified interface, one can imagine an oxygen deficiency at the FM/I interface instead of an oxygen excess. This aspect is currently under vivid discussion, since it has been completely neglected in the first-principle models proposed so far. Nevertheless, it has been recognized, that this situation reflects a rather realistic situation with respect to the preparation conditions experimentalists usually are dealing with: In order to avoid an oxidation of the ferromagnetic layers, the deposition of the barrier can be initialized with a reduced oxygen supply, which is increased to the correct amount after some monolayers [17]. Unfortunately, this kind of information up to now is only rarely available [8], so that no general conclusions on the impact on the tunneling process can be drawn so far.

On the theoretical side, very recent theoretical studies reported on the influence of

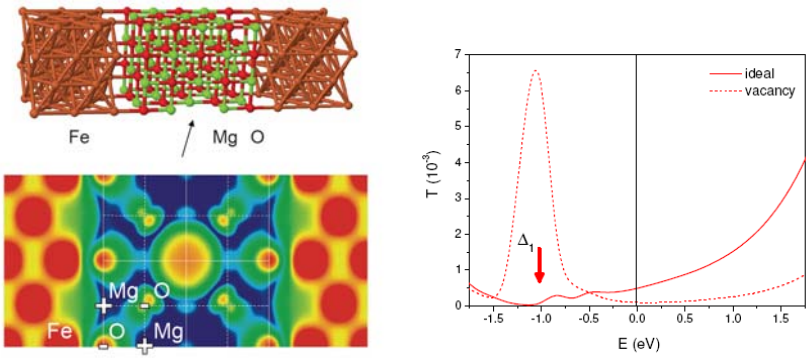

Figure 2.8: (left) Schematic drawing of one O vacancy in the middle of a MgO slab, sandwiched between two Fe electrodes and corresponding charge density (red: high and blue: low density). (right) Majority conductance in Fe/MgO/Fe(001) with one O vacancy. The latter induces a tunneling resonance -1eV below E_F. Directly at E_F, the conductance is reduced due to off-resonant scattering processes. Taken from [39].

oxygen defects on the spin-dependent tunneling in Fe/MgO/Fe(001) junctions [39]. These investigations consider a neutral oxygen vacancy, which is positioned in a bulk-like MgO slab being sandwiched between two Fe electrodes. A neutral oxygen vacancy traps two electrons of opposite spin character [104], which gives rise to a modification of the electronic structure surrounding this vacancy. As shown in Figure 2.8, the charge density of one O vacancy extends up to the nearest neighbors. By considering the transport properties, which are predicted for the defective MgO layer, it was stated that the vacancy gives rise to a resonance peak in the conductance of the Δ_1 majority channel, which is positioned below the Fermi energy as shown in Figure 2.8. The authors stated, that this resonance is not of practical interest due to its location away from E_F [39]. Just at E_F, however, the majority transmission is reduced in comparison to an ideal MgO barrier, due to a non-resonant scattering from vacancies [39]. This results in a larger decay rate for the Δ_1 state in the defective MgO, which in turn lowers the spin polarization of the tunneling current in the bulk barrier.

This theoretical model, however, does not consider the influence of O vacancies directly at the FM/I boundary. In view of the major modifications, which arise from the introduction of an oxygen excess at the FM/I interface, it is natural to expect a strongly modified interface bonding also at the oxygen deficient interface. So far, there are no theoretical studies available, which investigate the oxygen-deficient FM/I interface as a counterpart to the studies on the Fe/FeO/MgO system proposed by Zhang *et al.* [15]. At this point, we may speculate about a non-negligible influence of the oxygen defects on the Δ_1 partial density of states in the interface region. It is thus of great interest to study the electronic structure of oxygen-deficient FM/I interfaces in order to predict prospective consequences on the tunneling process.

Chapter 3

Experimental Methods

In this chapter, the experimental methods which are intensively employed to investigate the properties of ferromagnet/insulator surfaces and interfaces are reviewed. As a matter of course, the experiments have to take place *in situ* under ultrahigh vacuum (UHV) conditions. Different physical aspects are of high relevance in order to conduct a successful spin- and angle-resolved photoemission experiment: Whereas clean, single-crystalline samples with flat surfaces provide the basis for angular-resolved photoemission studies of the electronic band structure, the knowledge of the magnetic anisotropy is necessary for the spin-detection process.

The ability of preparing clean and high quality single-crystalline samples under UHV conditions is provided by molecular beam epitaxy. The continuative characterization of the samples involves the investigation of the surface structure by means of low-energy electron diffraction (LEED), the determination of the magnetic anisotropy of the ferromagnetic samples by magnetooptical Kerr effect (MOKE) and the chemical surveillance by Auger electron spectroscopy (AES), including surface cleanliness and composition. Moreover, AES is employed to calibrate the material growth rate.

On such well-defined FM/I samples, the electronic structure is investigated by spin- and angle resolved photoemission spectroscopy. Whereas the physical processes, which lead to the excitation of spin-polarized photoelectrons, are discussed in chapter 2.2, the present section deals with the technical details of the spin detection. In the last part of this chapter, the photoemission process from core-levels is discussed with respect to its elemental sensitivity. This method is extensively employed to study the oxidation state of the capping oxide layer.

After a brief glance on the general instrumentation of the experiment, the addressed methodologies and selected practical details of data acquisition and interpretation are presented in the following.

3.1 Layout of the experiment

The technical requirements for the preparation of thin films, their characterization and subsequent photoemission measurements are provided by a two-part ultrahigh vacuum (UHV) system. It consists of a preparation chamber equipped with standard analysis tools, which is connected to the spin- and angle-resolved photoemission experiment via a gate

valve. The photoemission vacuum chamber mainly houses the photoelectron spectrometer with the spin polarization detector. A load-lock with a capacity for eight holders is mounted on a transfer arm, which allows the transport of samples between both devices under UHV conditions. Details are indicated in Figure 3.1, which shows the stationary setup of the experiment at the storage ring DELTA (Dortmund University, Germany), where all photoemission experiments have been conducted.

The preparation chamber is equipped with several evaporation cells and two commercial UHV electron beam evaporators for material deposition. The samples can be cleaned by Ar-ion sputtering and thermally treated by resistive electron heating up to max. 580°C. Oxygen and argon can be introduced into the preparation chamber via a leak valve. The in-situ analysis facilities consist of a low-energy electron diffraction (LEED) optics and an electron gun with a cylindrical mirror analyzer (CMA) for Auger electron spectroscopy. Magneto-optical Kerr effect measurements are performed ex-situ in an IFF in-house facility.

The photoemission chamber is connected to the beamline 5 (U-250-PGM) at the storage ring DELTA. The undulator provides the beamline with linear p-polarized light and photon fluxes of about 10^{13} 1/s/100mA/0,1% BW. The maxima of the photon fluxes, which are determined by the storage ring current ($I \sim 1.5$ GeV) and the so-called K-value of the undulator, lie between photon energies of 14 eV and 76 eV. The actual photon energy employed in the photoemission measurement is set by means of a plane-grating monochromator (PGM) with a 300 lines/mm grating. Two focussing mirror units allow the vertical and horizontal positioning of the beam focus onto the sample inside the photoemission chamber. The samples are probed in a normal emission geometry with the photons impinging at an angle of 45° with respect to the surface normal. The kinetic energy of the photoelectrons is measured by a cylindrical sector analyzer (CSA) operating in a constant pass energy mode. The spin-analysis is performed by a spin-polarized low-energy electron diffraction (SPLEED) detector.

A base pressure of 1×10^{-10} mbar is maintained in both chambers. During a typical experimental cycle, each sample is freshly prepared and transferred from the preparation to the photoemission chamber immediately after deposition.

3.2 Molecular beam epitaxy

Photoemission studies on surfaces and interfaces require clean and monocrystalline samples, which are ideally prepared by molecular beam epitaxy (MBE). For simple physical reasons, the epitaxial growth of thin films onto a crystalline substrate is only possible, if the lattice mismatch is low. A common substrate class, on with stable phases of magnetic $3d$ transition metals can be deposited, are the III-V semiconductors single crystals [77].

Generally, the process of film growth determines the structure and morphology of the deposited film. The growth mechanism thereby depends on several parameters, e.g. on the deposition rate and the substrate temperature. Since atoms are evaporated from thermal sources, the mechanism of (epitaxial) film growth is determined by the surface kinetics. Several individual atomic processes influence the film growth in the non-equilibrium initial stage [41]. Phenomenologically, local equilibrium conditions hold in the case of low deposition rates and a high atomic mobility.

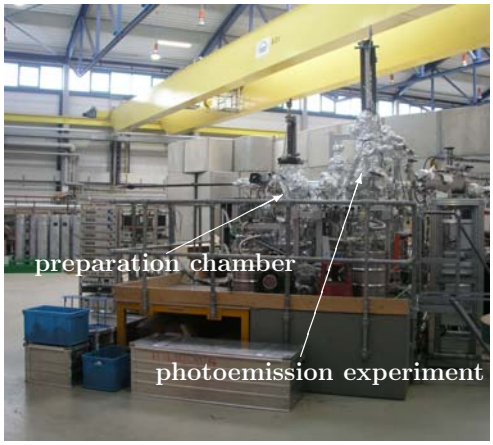

Figure 3.1: Stationary setup of the two-part UHV experiment at the beamline U250-PGM of the storage ring DELTA (Dortmund, Germany). The preparation chamber houses the evaporation cells and surface analysis tools. The photoemission experiments are operated by a CSA photoelectron analyzer with SPEED detector.

Under these assumptions, the growth mode is principally determined by the interaction between substrate and adsorbate. Whether an adsorbate sticks to the surface depends on the surface free energies of the adsorbate, γ_a, the substrate, γ_s and their interface, γ_i as discussed by Bauer [43]. In a simple model, the morphology of an adsorbate, deposited on an substrate, is determined by the balance of the surface free energies under thermal equilibrium conditions. If

$$\gamma_s \geq \gamma_a + \gamma_i, \tag{3.1}$$

a wetting adsorbate lowers the surface energy and creates a smooth first layer if the lattice mismatch is small. Any subsequent layer grows only after completion of the first one for sufficiently fast atomic rearrangements. This layer-by-layer growth mode is known as Frank-van der Merwe growth. In case of a considerable difference in lattice constants of the substrate and the adsorbate, the layer-by-layer growth is no longer favorable with increasing thickness due to an increasing misfit strain between the adsorbed material and the substrate. The growth proceeds with the formation of islands on a flat layer (Stranski-Krastranov growth). This mode leaves as much as possible of the first layer exposed and reduces the strain, because the islands can relax laterally. It is therefore important to choose suitably matched substrates and adsorbates in order to obtain a layer-by-layer growth. In the opposite case of a low surface free energy of the substrate,

$$\gamma_s < \gamma_a + \gamma_i, \tag{3.2}$$

the adsorbate will tend to form three-dimensional islands from the beginning of the deposition in order to minimize the surface energy. This growth mode is termed Vollmer-Weber growth.

Material	GaAs	Fe	Co	MgO
Surface Energy γ (10^3 erg/cm^2)	0.9	2.9	2.7	1.2

Table 3.1: Approximate surface free energies from Himpsel *et al.* [42].

A list of approximate, experimentally measured surface free energies for materials of particular interest in this work is given in Table 3.2 [42]. Generally, materials with a high surface free energy (e.g. Fe, Co) are supposed to achieve a layer-by-layer growth on top of a low surface free energy substrate like GaAs, only if the interfacial free energy γ_i is negative and overcompensates γ_a. Materials with a low surface free energy, like MgO, in turn provide a tight capping layer on ferromagnetic materials.

The above arguments are intended to serve as a rough guide for understanding trends in growth morphologies. They serve as important physical premise for the thickness calibration via Auger electron spectroscopy. Moreover, they are important for the sample preparation (see chapter 4) and consequently for the material selection.

3.3 Structural, magnetic and chemical characterization techniques

3.3.1 Low energy electron diffraction (LEED)

A standard method for studying the surface structure of epitaxial films is based on elastic scattering or diffraction of low-energy electrons (LEED). The technique can be employed to determine the periodic two-dimensional arrangement of atoms on a crystalline surface. In a LEED experiment, an electron beam with a primary energy between 30 and 500 eV impinges normally onto the sample. Since the incoming electrons are strongly scattered inside the crystal, the mean free path of the electrons is in the order of some Ångstrøms, which makes the method very surface sensitive. The elastically backscattered electrons give rise to diffraction spots which are imaged on a spherical screen. The condition for the occurrence of a diffraction spot is given by the Laue relation, $\mathbf{K}_\parallel = \mathbf{k'}_\parallel - \mathbf{k}_\parallel = \mathbf{G}_\parallel$, i.e. the component of the scattering vector parallel to the surface must be equal to the two-dimensional surface reciprocal lattice vector [19]. This condition is fulfilled for every intersection point of the real-space Ewald sphere with a reciprocal lattice rod. From the LEED pattern, one can thus deduce the symmetry of the reciprocal lattice and extract information on the quality of the sample. In particular, the presence of sharp diffraction spots indicates a high surface long-range crystalline order.

3.3.2 Magneto-optical Kerr Effect (MOKE)

The magneto-optical Kerr effect (MOKE) is the change of the polarization state of light, which is reflected at a ferromagnetic surface. The magnitude of this effect is controlled by the magnetization. It is used to identify the principal axes of the magnetic anisotropy [77].

The electromagnetic wave impinging on the surface is partially reflected and transmitted

through the interface. Since the thickness of thin films is in the range of the penetration depth of the light, the measured response comprises contributions from the reflected wave at the ferromagnetic surface and from the light transmitted through the thin film and reflected from the non-magnetic substrate. For the transmitted wave, the effect is known as the Faraday effect. The light reflected from the magnetic surface acquires an additional polarization component, which is not present in the incoming light. Phenomenologically, the incoming linear polarized light can be described as a linear combination of left- and right polarized light. By traversing the magnetic solid, the propagation velocities for both rotation directions are different. The resulting phase shift leads to an elliptical polarization of the reflected light. The angle between the main axis of the polarization ellipse and the incoming linear polarization is referred as the Kerr angle. The Kerr ellipticity is the length ratio of the major and minor axes. In the experiment, both quantities are used as the magnetic Kerr signal.

Depending on the geometry of the experiment, the Kerr effect is characterized as polar, longitudinal or transversal. In this work, the longitudinal geometry is employed, in which the magnetization lies in the reflecting surface parallel to the plane of the light incidence. Linear s-polarized light is created by focusing the light of a laser diode through a polarizer onto the sample. After reflection from the sample surface, the light passes a second polarizer, whose optical axis is rotated by 90° with respect to the first one. The photoelectric modulation of the incident light and detection with a lock-in amplifier reduces the influence of stray-light contributions.

This set-up is used to determine the magnetic anisotropy (hard/easy axes of magnetization) of the ferromagnetic films. It allows one to measure the in-plane component of the magnetization, by assuming that the Kerr intensity is proportional to the sample magnetization. Sweeping the magnetic field yields a hysteresis loop, which is used to extract information on the magnetic properties.

3.3.3 Auger electron spectroscopy (AES)

A standard method to study the growth of thin films and the surface chemical concentration is based on the analysis of Auger electrons. The advantage of AES is its elemental sensitivity, which relies on the physical mechanism of the emission of Auger electrons: At first, an electron beam ionizes an atom from a core level shell. In a second step, the hole created in the inner shell is filled by an electron of an outer shell. The gained energy is transferred to a second electron which can be emitted from the atom at a well-defined kinetic energy. A measurement of this kinetic energy can be used to identify the particular atom, because of the unique core-level energy signature.

Since the Auger signals are small, the spectrum of emitted Auger electrons is detected as a function of the first derivative of the kinetic energy dN/dE to suppress the large background of secondary electrons. An electron multiplier is operating in a voltage regime, in which the amplified signal is proportional to the original Auger signal. The differentiation is performed by modulating the voltage and detecting the signal from the electron multiplier with a lock-in amplifier.

On the basis of this detection mode, the measured signal is proportional to the atomic concentration of a surface. Therefore, AES is commonly used to check the cleanliness

Material	Cu	Fe	Co	Mg
Auger transition (eV)	922	705	716	1188
λ_{SD} (Å)	16.4	14.3	14.4	18.6
λ_{exp} (Å)	13.5 ± 0.6		9.6 ± 0.6	

Table 3.2: Empirical and experimental values for the attenuation length λ for particular Auger transitions. The empirical values λ_{SD} depend only on the kinetic energy [50]. The experimental data λ_{exp} has been obtained by overlayer-film experiments [54].

of a surface, with a sensitivity of about 1% of a monolayer [41]. Moreover, information on the quantitative concentration of an element at a surface can be obtained from the Auger peak intensity, which is proportional to the peak-to-peak height in the derivative count mode [85]. The measured Auger intensity thereby depends on atomic parameters, the experimental geometry as well as on properties of the electron analyzer [51]. If the measurements are obtained under the same experimental conditions, the Auger intensity I is assumed to be proportional to the atomic density n of the element and its element specific sensitivity S, with $I = n \cdot S$ [85]. The comparison of two Auger peaks of element A and element B thus yields the relative concentration,

$$\frac{n_A}{n_B} = \frac{S_B}{S_A} \frac{I_A}{I_B}, \tag{3.3}$$

with $S_{A,B}$ denoting the elemental specific sensitivity factors, which can e.g. be taken from [85]. Equation (3.3) is applied to study the chemical composition of the prepared sample surfaces.

Furthermore, AES is employed in this thesis to estimate the film thickness of a material deposited on a substrate. For this purpose, the intensities of Auger signals emitted from the substrate and the film are recorded during the deposition process. In practice, the necessity of a constant growth rate is guaranteed by an automatical regulation of the evaporant's flux. By this, the evaporation rate is directly related to the evolution of the film thickness.

The underlying physical mechanism involves the scattering of Auger electrons originating from the substrate within the deposited film material. The Auger intensity I of the substrate depends exponentially on the overlayer film thickness d and is characterized by the attenuation length of the Auger electrons λ,

$$I(d) = I_0 \cdot \exp(-d/\lambda). \tag{3.4}$$

To reasonably estimate the film thickness d, the growth mode of the deposited film has to be taken into account. In the case of a Stranski-Krastanov growth mode, the total film thickness d is composed out of the wetting film thickness d_f and the 3-dimensional island height d_i. In practice, this approach is limited by the fact, that the relation between d_f and d_i is usually unknown. To overcome this difficulty, a substrate/film combination should ideally be chosen for the thickness calibration, for which a 2-dimensional layer-by-layer growth is confirmed experimentally. The expression for the thickness of the overlaying adsorbate d thereby reduces to $d_i = 0$ and $d_f = d$. By applying this assumption, the

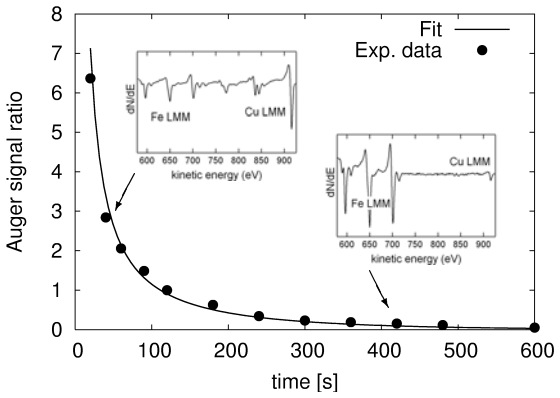

Figure 3.2: Correlation between Auger signal ratio $I_R = I_s(E)/I_f(E)$ and deposition time t, as determined from the corresponding Auger peak-to-peak heights of film and substrate.

integrated Auger intensities of substrate I_s and film I_f take the form

$$I_s = I_0 \cdot S_s \cdot \exp\left(-\frac{d}{\lambda_s}\right) \qquad \text{and} \qquad I_f = I_0 \cdot S_f \left(1 - \exp\left(-\frac{d}{\lambda_f}\right)\right), \tag{3.5}$$

with S_s and S_f being the sensitivity factors for the corresponding Auger transitions [56]. Furthermore, λ_f and λ_s denote the attenuation lengths of the Auger electrons originating from film and substrate, respectively. The primary intensity I_0 is eliminated from equation (3.5) by considering the Auger signal ratio I_R

$$I_R = \frac{I_s}{I_f} = \frac{S_s}{S_f} \frac{\exp\left(-\frac{d}{\lambda_s}\right)}{1 - \exp\left(-\frac{d}{\lambda_f}\right)}. \tag{3.6}$$

The experimental data set I_R consists of the peak-to-peak signal ratio of the corresponding Auger transitions of film and substrate, as illustrated exemplarily in Figure 3.2, with the Auger signal ratio I_R being plotted versus the deposition time t. The film thickness is thereby expressed as $d = R \cdot t$, with R denoting the material deposition rate. The values for R/λ_s are determined by a fit of the theoretical curve according to equation (3.6) to the experimental data points. Equation (3.6) reveals, that the attenuation length λ is actually the key parameter in this quantitative analysis, which sets the length scale of the film width and the deposition rate. In a further step, the ratio λ_f/λ_s is fitted as a separate parameter and an improved matching of the experimental data and the fit curve is achieved.

The attenuation length of electrons in a solid depends on their kinetic energy as well as on the electronic structure and atomic arrangement. The energetic dependence of λ is usually derived from the so-called universal curve proposed by Seah and Dench [50]. This universal curve, expressed by

$$\lambda[\text{Å}] = \frac{14.3}{\sqrt{E}} + 0.54\sqrt{E}, \qquad E \text{ in eV}, \tag{3.7}$$

has been obtained from a best fit for the experimental attenuation length of a large set of electron energies and materials. By this approach, an approximation for the order of magnitude of the attenuation length can be derived. Table 3.2 lists the calculated attenuation lengths according to equation (3.7) for the relevant materials.

Although the energy dependence of λ is reflected quite well in this approach, the material dependence is not accessible. In fact, the data set in [50] reveals a scatter of the attenuation lengths for different materials by almost one order of magnitude for a specific energy. We therefore use experimental values for λ_s, which were obtained for the investigated materials in a comparable experiment [54] and are given in Table 3.2. In comparison to the calculated data according to equation (3.7) these values are smaller by more than 20%. We note, that the fitted value λ_s/λ_f is in agreement with the data taken from [54].

It should be remarked, that it is inadequate to employ the inelastic mean free path (IMFP) instead of the attenuation length in this quantitative analysis. In fact, both quantities are often used interchangeably, which makes it important to distinguish their proper meaning: The attenuation length is related to the opacity of a solid for an electron of a certain energy, which arises from both elastic and inelastic scattering events. It can be obtained by overlayer-film experiments and is based on equation (3.4). The IMFP, in contrast, is defined as the mean distance an electron can travel in a solid until it undergoes an inelastic collision and can be predicted by theoretical calculations, which derive the element specific IMFPs at discrete electron energies [52]. It is found, that the IMFP is usually systematically larger than the attenuation length by about 15-30%, which is due to the fact, that the elastic scattering contributions are neglected.

An intrinsic uncertainty in the thickness determination may originate from the growth morphology. If, for instance, the adsorbate tends to adopt a 3-dimensional growth mode instead of a layer-by-layer mode, the film thickness will be underestimated since the same amount of material yields a smaller attenuation of the substrate signal. This is why the calibration of the film thickness is performed on a fcc Cu(100) single crystal substrate, on which a layer-by-layer growth is reported for fcc Fe and fcc Co [53]. In the case of a Mg thickness calibration on Cu(100), the actual deposition rate may be slightly underestimated due to the possible island formation during the deposition process.

3.4 Operating the spin- and angle-resolved PES experiment

The following section introduces the practical aspects of a spin- and angle-resolved photoemission experiment. The physical mechanisms, which lead to the excitation of spin-polarized photoelectrons, have been previously discussed in chapter 2.2.

The aim of a spin-and angle-resolved photoemission experiment is to analyze the kinetic energy, the momentum and spin polarization of the photoelectrons, which have been excited from the ferromagnetic sample under investigation. This endeavor requires a suitable electron detector which allows to measure all quantities simultaneously. The momentum of the photoelectrons can be selected by a defined small angle of collection at the entrance of the spectrometer unit. The kinetic energy of the incoming photoelectrons is selected by retarding electromagnetic fields in the energy analyzer. In order to measure the degree

of spin polarization of the electron beam, a spin detector converts this quantity into an intensity asymmetry of the spin-polarized photoelectrons. Basically, all methods to analyze the spin polarization of an electron beam rely on the spin-dependent scattering at solid surfaces [48].

The basic setup of the instrument employed in this work is schematically sketched in Fig. 3.3. The electron detector consists of three main parts: the transfer lens system, the energy analyzer and the spin-polarization detector. The incoming photoelectrons are collected from the lens system within an angle of $\approx 6°$ and are focused on the entrance slit of the energy analyzer. During their transfer through the lens system, the electrons are accelerated or decelerated to a constant kinetic energy, the so-called pass energy. The experimental energy resolution is defined by the angular acceptance of the entrance slit optics, the pass energy of the analyzer as well as the entrance and exit slit width.

After having left the energy analyzer, the monoenergetic electrons are accelerated onto the (100) surface of a tungsten single crystal, which represents the main part of the spin-polarization detector [44, 45]. The basic principle of operation relies on the fact, that the scattering probability for spin up and spin down electrons at the W(100) surface differs, if they are scattered in off-normal directions [46]. The spin-dependent contribution to the scattering potential of the tungsten atoms arises from the strong spin-orbit coupling, which is present in all materials, but increases with the atomic number Z. This results in a difference of the scattering cross sections $\sigma^{\uparrow,\downarrow}$ for spin-up and spin-down electrons as a function of the scattering angle Θ. In particular, spin- up and spin-down electrons are scattered with different probabilities in opposite directions $\sigma^{\uparrow,\downarrow}(\Theta) \neq \sigma^{\uparrow,\downarrow}(-\Theta)$. This gives rise to a left-right asymmetry of the intensity of the scattered beam, which is directly proportional to the polarization of the primary beam. This intensity asymmetry of the scattered electron beam can be measured by a LEED-type detection system, as illustrated in Figure 3.3. Each spot pair is thereby sensitive to the component of the spin polarization vector, which lies perpendicular to the scattering plane: The spin polarization component, which lies parallel to the sample surface is thus detected by the (0,2) beams, whereas the component perpendicular to the surface leads to an intensity asymmetry in the (2,0) spots.

The maximum efficiency for the spin asymmetry detection is achieved, if the incoming electrons hit the W(100) surface at normal incidence and at a scattering energy of 104.5 eV. However, only a small fraction of the incident beam finally reaches the channeltrons of the LEED system. The spin sensitivity, which is a measure for the analyzing power between the measured asymmetry A and the spin polarization P of the incoming beam, reaches a value of just $S = 20\%$. In order to compensate this low efficiency of the spin detector, high photon fluxes are essential to operate a spin-resolved photoemission experiment.

The sensitivity of the asymmetry measurement is strongly influenced by the cleanliness of the W(100) surface. It is therefore necessary to provide an UHV environment for a proper functioning of the spin detector. Prior to each measurement, any carbon and other contaminations are therefore removed by flash treatments, which heat the crystal and desorb the contaminants.

In order to define a quantization axis for the spin of the electrons, it is necessary to remanently magnetize the sample under consideration. The direction of the remanent magnetization thereby should be aligned with one of the spin-sensitive axes of the spin detector to achieve a maximum signal. The investigated epitaxial ferromagnetic thin films

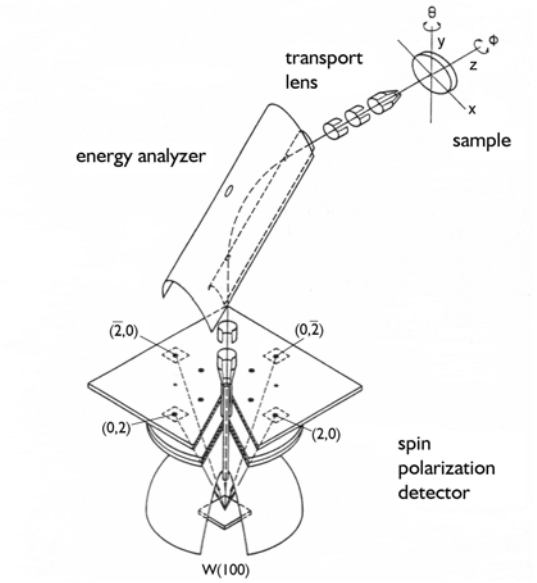

Figure 3.3: Schematic layout of the photoelectron detector combined with the SPLEED spin-polarization detector. Taken from [22].

are ideally magnetized as a single domain. The magnetizing field is obtained from a permanent magnet which is approached next to the sample, thereby magnetizing it in in-plane direction parallel to the sample surface. To minimize any stray fields, the permanent magnet is completely removed from the setup after the magnetization process and the measurements are made with the sample in the remanent magnetic state.

To eliminate any error introduced by apparatus related asymmetries, two measurements of the spin polarization are performed, one with the sample magnetized in "M=+x" direction and the one with the magnetization in "M=-x" direction (see Figure 3.3). The number of electrons scattered from the W(100) surface into the $(0,2)$ and $(0,\bar{2})$ channels are denoted by the intensities $I^+_{(0,2)}$, $I^+_{(0,\bar{2})}$ and $I^-_{(0,2)}$, $I^-_{(0,\bar{2})}$, respectively. By assuming that the incident beam does not move between the two measurements, the instrument asymmetry can be removed by combining the four data sets. The spin polarization P is then given by

$$P = \frac{1}{S} \cdot A = \frac{1}{S} \frac{\sqrt{I^+_{(0,2)} I^-_{(0,\bar{2})}} - \sqrt{I^-_{(0,2)} I^+_{(0,\bar{2})}}}{\sqrt{I^+_{(0,2)} I^-_{(0,\bar{2})}} + \sqrt{I^-_{(0,2)} I^+_{(0,\bar{2})}}}. \tag{3.8}$$

The individual partial intensities I of the spin-up and spin-down spectra are obtained from the polarization P according to equation (2.19),

$$I^{\uparrow} = I_0(1+P), \qquad I^{\downarrow} = I_0(1-P), \qquad \text{with} \qquad I_0 = \frac{I^+_{(0,2)} + I^-_{(0,2)} + I^+_{(0,\bar{2})} + I^-_{(0,\bar{2})}}{4}. \tag{3.9}$$

3.5 Core-level photoemission spectroscopy

Core-level photoelectron spectroscopy is a suitable method to determine the chemistry of a surface, since the spectrum of binding energies is unique for each element. In a solid, the difference in binding energies between two chemical states of the atoms is of special interest, because it reveals modified bonding states. This energy difference is referred as the chemical shift.

The underlying physics of the photoemission process in a solid is discussed in chapter 2.2.2. The binding energy E_B of a core-level line is characteristic for the chemical environment of the atom, because any chemical bonding results in a redistribution of charge. Thus, one can distinguish between atoms of the same element with non-equivalent occupancy of the atomic sub-shells due to a measurably difference in the binding energy [55]. Obviously, with increasing positive charge of an ion, the binding energy increases, whereas with increasing negative charge, the binding energy decreases.

In this work, core-level photoemission spectroscopy is employed to investigate the stoichiometry of ultrathin MgO_x films. In particular, we distinguish between under-oxidized $MgO_{x,\,x<1}$ films and nearly stoichiometric MgO layers, because the oxidation of Mg to Mg^{2+} is accompanied by an increase of the binding energy. The core-level measurements are performed in a spin-integrated mode and the recorded spectra are analyzed with respect to the energetic position and shape of the feature in question.

Any quantification of the core-level features, however, requires a physical model which serves as an input for a standard fit procedure [60]. In the present context, the fit procedure is used to extract information on the degree of oxidation of the Mg $2p$ level. The main parameters for the interpretation of the core-level features are their energetic position, spin-orbit splitting, line shape and their integrated peak area. It is therefore necessary to subtract the secondary electron background from the original spectrum. These particular issues, which are required for the fit procedure, are addressed in the following.

Secondary electron background Every photoemission feature is accompanied by an increased background intensity in the region of higher binding energies. This background signal corresponds to electrons, which have undergone inelastic scattering in the sample. Since only unscattered photoelectrons carry direct information on the electronic structure, this primary peak signal has to be separated from the measured spectrum.

In this work, the model of Shirley is used to correct the spectra from the inelastic scattering background [57]. It assumes that each unscattered electron is associated with a flat background of energy losses. The background intensity within a peak is assumed to be proportional to the integrated intensity at higher energy, with the condition that the background matches the measured spectrum outside the region of the peak. By dividing the total peak area in the regions P and Q according to Figure 3.4, the background intensity $B(E)$ at the energy E is expressed as

$$B(E) = I(E_1) + \alpha \frac{Q}{P+Q} = I(E_1) + \alpha \frac{\int_E^{E_1} I(E')dE'}{\int_{E_2}^{E_1} I(E')dE'}, \tag{3.10}$$

where $\alpha = I_2 - I_1$ defines the step in the background [61]. Since $B(E)$ is initially unknown, the calculation of a Shirley background is an iterative procedure. The integrated areas P

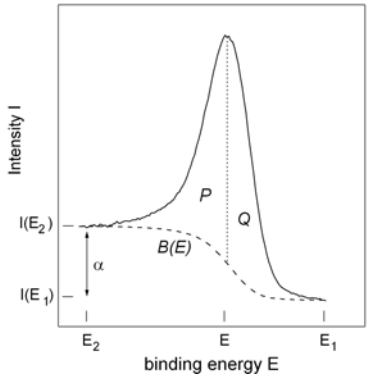

Figure 3.4: Schematic drawing of the Shirley background substraction method and definitions for the calculations. Here, B(E) is the background intensity.

and Q must initially be calculated for each point on the background using an approximation to $B(E)$, then they are redefined using the first approximation as an input to improve the values of P and Q:

$$I^{n+1}(E) = I^0(E) - \frac{I(E_1)}{\int_{E_1}^{E_2} I(E')dE'} \int_E^{E_2} I^n(E')dE'. \tag{3.11}$$

The method of Shirley is well-suited for the case, that the energy loss of scattered electrons is low and nearly constant in the region of the corrected energy interval.

Chemical shift Shifts in the binding energy of peaks follow the changes of the chemical environment of the same atom. The value of the chemical shift is usually of the order of a few or even less than one eV [85]. The analysis of a particular core-level allows in principle to trace back the oxidation state of the atom by modeling the peak by a distinct number of lines. These lines are positioned at the corresponding binding energy positions, which are available in the literature [85]. In this work, the Mg $2p$ level is modeled by taking into account the neutral Mg^0 and the double-charged Mg^{2+} state in a fit procedure. The integrated peak areas of the fitted Mg^0 and Mg^{2+} lines are related in order to estimate the degree of oxidation of the MgO_x layers. No contributions from Mg^+ states are included, because the large difference in electronegativity between Mg and O suggest a full charge transfer in the case of a ionic bonding.

Spin-orbit coupling In terms of a coupling between orbital and spin moments in an atom, electrons ejected from states with a non-zero orbital momentum $l \geq 1$ can leave the core into two excited states. These doublet states are characterized by the total quantum number $j = l \pm s$ which defines the $2j+1$ degenerated fine structure. The relative intensities I of these doublet pairs is thus given by

$$\frac{I_{j=l-s}}{I_{j=l+s}} = \frac{2(l-1/2)+1}{2(l+1/2)+1} = \frac{l}{l+1}. \tag{3.12}$$

In the case of p electrons (l=1), the relative intensities $p_{1/2} : p_{3/2}$ are thus calculated as 1 : 2. This intensity ratio is applied in the Mg $2p$ core-line modeling.

Core-level shapes The line shape of a core-level peak is determined by the physics involved in the ionisation process. In order to model a core level feature, one chooses appropriate functions which are fitted to the peak in a least-square refinement. The basic shape of a core-level peak is of Lorentzian-type, which takes into account the peak broadening due to the finite core-level lifetime. The influence of the measurement process (e.g. thermal broadening) may be modeled by a Gaussian contribution. Both functions are symmetric with respect to the peak maximum.

In case of metallic elements, the observed spectral features may reveal a peak asymmetry, which can be modeled by a synthetic line shape (Doniac-Šunjić (DS)) [51]. The asymmetry of the core lines of metallic samples is caused by electron-hole excitations near the Fermi level, which are directly proportional to the density of states. In semiconductors and insulators, no asymmetry in core-level peaks is observed, because the band gap eliminates the possibility of exciting low-energy electrons just below the Fermi level. The critical issue related to asymmetric line shapes is that the asymmetric tail shifts the intensity away from the peak maximum towards higher binding energies. If a DS-line shape is used to quantify chemical states, the need to calibrate the intensity becomes important [61]. For a standard analysis, fit expressions based on mixed Gaussian-Lorentzian functions are most suitable for intensity quantifications [61].

As will be shown in chapter 4.4, the analysis of the Mg $2p$ core-levels originating from MgO_x films reveals an almost symmetric shape of the peaks and thus indicates the evolution of an – at least partially – oxidized state. In the practical fitting procedure, the Mg $2p$ level is therefore modeled by two Gaussian-Lorentzian sum functions for the Mg^0 and the Mg^{2+} level, respectively. This approach yields a good agreement between the fitted curve and the experimental data.

Quantifying atomic concentrations The photoemission intensity of core levels can be employed to determine the concentration of an element. As has been discussed in chapter 3.3.3, the total intensity $I(E)$ of the core level line depends on the atomic properties of the sample, the experimental geometry and the properties of the analyzer [85]. Geometry and instrumental contributions are eliminated by referring all quantifications of the core level intensities to the same reference. According to chapter 3.3.3, the relative intensities of the core-level lines of elements A and B, which have been recorded under similar conditions, can be written as

$$\frac{n_A}{n_B} = \frac{\sigma_B}{\sigma_A} \frac{I_A}{I_B}, \tag{3.13}$$

with σ denoting the energy-dependent photoionization cross-section and $n_{A,B}$ the density of atoms in the sample.

The analysis of the Mg p core levels, as presented in chapter 4.4, relates the relative intensities of the Mg^0 and the Mg^{2+} lines to the degree of oxidation of the MgO_x layer. Hence, the energetic position of the Mg $2p$ peak is a reliable measure, since the peak is very symmetric.

Chapter 4

Sample Preparation and Characterization

In the present chapter, the successive preparation steps yielding the MgO_x/Fe(001)/GaAs and MgO_x/Co(001)/Fe/GaAs systems, which are extensively investigated in this thesis, are presented in detail.
Due to the strong link between structural and electronic properties, a main aspect concerns the determination of the crystal structure of the prepared samples. The knowledge of the crystalline structure of the system under investigation enables a correct interpretation of the photoemission results. Low-energy electron diffraction (LEED) experiments are employed to identify the type of surface reconstruction of the semiconducting GaAs substrate. In a second step, the crystalline structure of the thin Fe and Co films, which are deposited subsequently on the GaAs substrates, is monitored.
The chemical characterization of the samples involves the surveillance of surface cleanliness for the successive preparation steps. AES has been employed to investigate the atomic termination of the GaAs surface. Moreover, the analysis of the core-levels of substrate and film constituents can reveal a possible intermixing of substrate atoms into the Fe film, which is typically observed in thin ferromagnetic films grown on semiconductors.
One main prerequisite for a successful spin-resolved photoemission experiment is the knowledge of the magnetic anisotropy of the ferromagnetic samples. In order to achieve a maximum spin asymmetry signal, the remanent magnetization should be aligned with one of the spin-sensitive axes of the spin-polarization detector. Magnetization loops are recorded *ex situ* by means of magneto-optical Kerr effect.
Special attention is drawn to the chemical properties of the MgO_x overlayers. The main parameter concerns the MgO_x degree of oxidation, which will be related to the electronic structure of the FM/I interfaces. In order to quantify influences induced by the MgO stoichiometry, the actual chemical state of the MgO covering layers is examined *in situ* by core-level photoelectron spectroscopy. It will be shown, that a reasonable estimation of the oxidation state is possible by employing suitable fitting procedures.

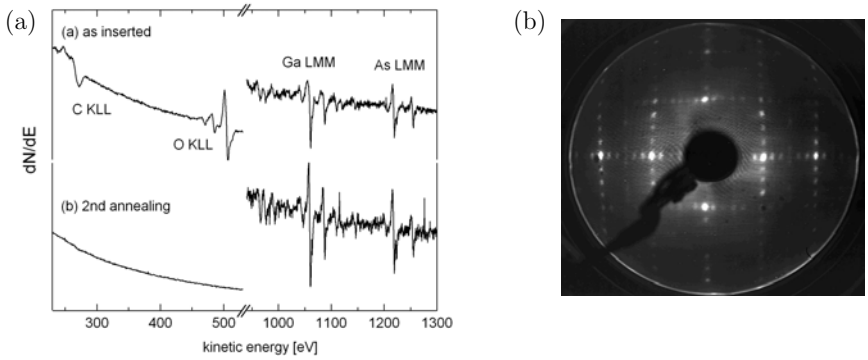

Figure 4.1: (a) Auger spectra recorded from a GaAs substrate (a) as inserted and (b) after the second annealing process. The principal surface contaminants oxygen and carbon are removed by the employed preparation procedure. (b) LEED pattern of a (4x6) reconstructed GaAs surface, taken at E=113 eV.

4.1 GaAs substrate preparation

The MgO_x/Fe and MgO_x/Co thin films investigated in this thesis are grown on well defined GaAs (001) crystal surfaces. GaAs has a zincblende structure with a lattice constant $a_{GaAs} = 5.654$ Å. The zincblende structure can be viewed as composed of two face-centered cubic (fcc) lattices with two separate atom bases, one formed by the Ga atoms, the other by the As atoms. The two lattices are shifted along the diagonal by $1/4\, a_{GaAs}\sqrt{3}$ which gives rise to the tetrahedral coordination. The structure consists of alternating and evenly spaced monoatomic planes in (001) direction, which makes the GaAs (001) surface either Ga- or As-terminated. The Ga-bonds are thereby oriented along the (110)- and the As-bonds along the $(\bar{1}10)$-direction. This asymmetry of the GaAs surface has consequences for the magnetic properties of ferromagnetic films grown on GaAs, which results in an in-plane magnetic anisotropy as discussed in section 4.2.1.

Due to the absence of neighboring atoms, the symmetry of the surface is lowered and a redistribution of the surface atoms may become energetically favorable. In tetrahedrally bonded semiconductors like GaAs, the breaking of the strongly directional sp^3 covalent bonds yields so-called dangling bonds, which follow the principle of energy minimization and saturate by creating new surface reconstructions [25]. A number of reconstructions have been observed for GaAs and are dependent on parameters like temperature and preparation conditions [62]. In general, the As-terminated surfaces are obtained at lower temperatures than Ga-terminated surfaces, since As is more volatile. In the order of decreasing As content, the following reconstructions are reported for GaAs(001) surfaces: c(4x4), 2x4, 1x6, 4x6, 4x2 and c(8x2) [62]. In practice, the process of surface reconstruction counteracts with the elimination of the desorbed native oxides from the surface, which are removed by ion-bombardment. Therefore, sputtering at low energies is required to minimize the damage created by this process. A subsequent annealing is necessary to recover the

surface crystallography. Scanning tunneling microscopy (STM) studies showed that 500eV Ar^+ sputtering with postannealing results in a respectable surface quality with terraces of 50nm width [63]. Care must be taken when elevating the temperature of GaAs, because it decomposes at the surface at too high temperatures. In the following, we present a procedure to obtain a Ga-terminated, (4x6) reconstructed GaAs substrate surfaces. It has been shown, that this GaAs face is particulary suited to grow epitaxial Fe(001) films [71].

The GaAs substrates which have been employed in this work are taken from commercial GaAs wafers (Crystec, Te-doped n-type). Basically, they are treated by two subsequent sputtering and annealing processes, with each step being followed by Auger electron spectroscopy to monitor the evolution of the surface contamination. As a preliminary procedure, the GaAs templates of a size of (8 x 11) mm are cleaned in two separate ethanol and acetone ultrasonic dips and inserted into the UHV without further chemical treatment. A typical Auger analysis of the GaAs surface in Fig. 4.1 indicates the principal surface contaminants to be oxygen (O) and carbon (C). The oxide is largely removed by a first low-energy 500 eV Ar^+-sputtering of 20 minutes. The sputter process is performed at room temperature at an angle of 45° with respect to the surface normal. Subsequently, the sample temperature is gradually raised with a rate of $r \approx 20°C/min$ to a temperature of roughly 500°C to degas the GaAs plate and desorb remaining contaminants. The temperature of 500°C is held until the base pressure drops below a value of $p \sim 3 \times 10^{-9}$ mbar. After the sample has cooled down below a temperature of 100°C, a second low-energy sputtering cycle at 500 eV for 10 minutes is performed in order to achieve a final removal of rest O and C contaminants. The procedure is followed by a second annealing process at a temperature of roughly 560°C for 45 min or longer to promote the formation of the healing surface reconstruction. The temperature is again ramped up and down at a rate of $r \approx \pm 20°C/min$. After the GaAs substrate is cooled down below a temperature of 100°C, no C and O contaminations on the surface are observed within the AES detection limit (see Fig. 4.1(a)).

A qualitative tendency concerning the evolution of the Ga and As content within the GaAs surface during the successive preparation steps can be extracted from analyzing the intensities of the Ga and As *LMM* Auger transitions. The analysis involves the determination of the peak-to-peak heights of the Ga *LMM* transitions at 1069 eV and 1096 eV and the As features at 1229 eV and 1264 eV in the differential AES spectrum dN/dE. The estimated peak-to-peak heights are corrected by the corresponding elemental sensitivity factors [56]. The relative intensities Ga(1069 eV)/Ga(1096 eV) and As(1264 eV)/As(1229 eV) are found to coincide with an error of about ±10%. The analysis of the relations Ga(1069eV)/As(1264 eV) and Ga(1096 eV)/As(1229 eV) exhibits the following tendency: Basically, after each sputtering process, the Ga content increases by approximately (40 ± 5)%, because arsenic is preferentially sputtered. The Ga content is again slightly reduced by $(15 \pm 5\%)$ after each annealing process, because As atoms are able to diffuse from the inner part of the sample towards the surface. In comparison to an unprepared GaAs surface, the total Ga content is found to increase by (30 ± 5)% after both sputtering and annealing processes[1].

[1]The mean free path λ of Auger electrons with kinetic energies between 1000 eV and 1200 eV is in the range of 17 to 19 Å. The surface probing depth of the Auger electrons thus involves the first 4 ML of the GaAs cell size (a_{GaAs} = 5.654 Å). In comparison, the mean free path in the UV-photoemission

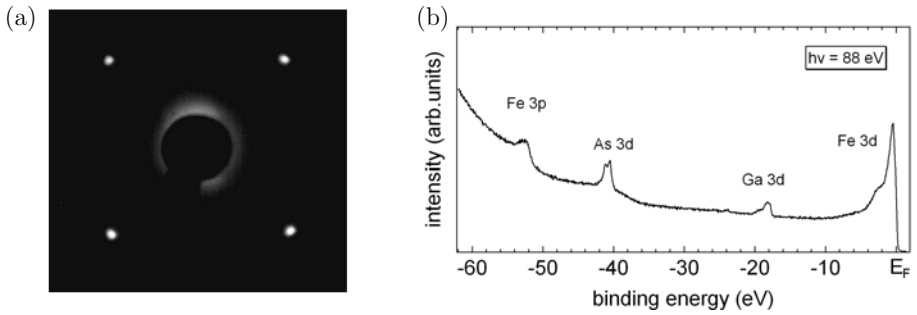

Figure 4.2: (a) LEED picture of a 27 ML thick Fe film recorded an an energy of 52 eV. (b) Core-level spectrum of a 27 ML thick Fe film recorded at a photon energy of $h\nu$=88 eV.

The crystalline structure of the GaAs substrate surface is investigated by low-energy electron diffraction. The representative LEED pattern in Fig. 4.1 (b), taken at $E = 113$ eV, displays a well-ordered (4x6) reconstruction of the surface at room temperature. The crystal axes are orientated along the (110) and ($\bar{1}$10) directions. The symmetry of the pattern is known to deplete considerably the As compared to the As terminated surface [64], which is confirmed by the analysis of the corresponding Ga and As Auger transitions. The sharp diffraction spots indicate a high quality long-range order of the GaAs (4x6) surface. On this well-prepared substrates, the deposition of thin iron films is performed, which is presented in detail in the following section.

4.2 Fe growth on GaAs(001)

It has already been shown in the early eighties, that Fe grows epitaxially on the GaAs (001) surface and thereby adopts a bcc lattice structure ($a_{Fe} = 2.866$ Å) [65, 66]. This is due to the fact that the lattice constant of bcc Fe is almost exactly half that of GaAs ($a_{Fe} = 5.654$Å), with a lattice mismatch of $2a_{Fe}/a_{GaAs} = 1.013$. In the following, the thickness is given in monolayers (ML) corresponding by convention to the Fe(001) lattice spacing of 1.43 Å.

Various studies reported on the epitaxial growth of Fe onto the (4x6) reconstruction of the GaAs (001) surface [63, 71, 74]. In the initial stage, a three-dimensional Volmer-Weber growth mode is consistently observed for the first 1-3 monolayers [71], followed by a gradual smoothing of the Fe surface turning into a quasi layer-by-layer growth. A coalescence of the islands begins at thicknesses of 3 to 5 ML [68,70]. The layer-by-layer growth is reported to persist up to a coverage of 70 ML [70]. The temperature regime during the deposition of the Fe layers thereby ranges between room temperature [62], slightly elevated temperatures ($T = 50$°C) [70] and higher temperatures of up to $T = 175$°C [66]. Generally, clear LEED

experiments ($h\nu \leq 40$ eV) is less than λ =10 Å.

patterns develop at higher Fe coverages (5 ML) for room temperature deposition [62] than at higher growth temperature [71]. This is consistent with several studies, which propose the optimum growth temperature being around 170°C [66, 71].

The morphology of thin Fe films on the GaAs (4x6) and (2x4) surface has been investigated by scanning tunneling microscopy (STM) by Monchesky *et al.* and Thibado *et al.* [63, 75]. A moderate roughness of the Fe film is observed, being partially introduced by the initial GaAs surface morphology, which is not completely flat. Their investigations reveal an island width of 40 Å for a 20 ML thick Fe film grown on (4x6)-GaAs (001) (Ref. 14 in [63]) and a average island size of 50×80 Å^2 for a 35 ML thick Fe film on GaAs(2x4)[2] [75].

Although the lattice constant of Fe(001) is well matched to GaAs(001), interdiffusion of As and Ga into deposited Fe layers presents a general difficulty [76]. Arsenic is known to segregate to the Fe surface for all Fe growth mechanisms on GaAs(100), regardless of the substrate reconstruction or preparation. A deposition of Fe on GaAs(4x6) at room temperature is therefore supposed to diminish the interdiffusion into the Fe layer. Moreover, a post-annealing of the Fe films in order to achieve a smoother surface is not advised for the same reason[3].

In practice, Fe is deposited onto the (4x6) reconstructed GaAs(001) substrates from an electron-heated Fe rod in a base pressure of 2×10^{-10} mbar. The deposition rate is approximately 4 Å/min, as determined by AES calibration of (fcc) Fe deposited on a (fcc) Cu(001) single crystal (for details see chapter 3.3.3). The Fe films are grown at slightly elevated temperatures of about T =100°C, which represents a compromise between good structural growth conditions observed at higher temperatures and an attempt to reduce the interdiffusion of the substrate components. The Fe surface is investigated by AES after growth to monitor the cleanliness of the film. No oxygen and minimal carbon traces are detectable within the AES detection limit.

The crystalline structure of the deposited Fe films is determined by means of LEED. Figure 4.2 (a) displays the LEED pattern of a 27 ML thick Fe film taken at an energy of $E =$ 52 eV. The first order diffraction spots indicate a fully epitaxial matching. The existence of a bcc structure of the Fe film is deduced from the sequences of higher order diffraction spots. A moderate roughness of the Fe film is deduced from the slightly broadened spot size compared to the spot-to-spot distance.

In order to determine the extent of segregation or intermixing of substrate atoms into the Fe film, the Fe 3p, Ga 3d and As 3d low-energy core levels are monitored after Fe deposition. Photons of $h\nu$ =88 eV are used to excite the photoelectrons which posses a very high surface sensitivity due to their low kinetic energies. Figure 4.2 (b) displays the corresponding core level spectrum for a 27 ML thick Fe film on (4x6)-GaAs. Beside the Fe 3p peak located at a binding energy of $E_B = 52.3$ eV, the Ga 2p and As 3p core levels located at 18.7 eV and 41.7 eV, respectively, indicate that As and Ga are located in the

[2]The GaAs(2x4) reconstruction is even more Ga-rich that the GaAs(4x6) surface. The Fe growth process on both surface reconstructions proceeds nearly similarly [67].

[3]An epitaxial growth of bcc Fe(001) is also reported on single crystalline MgO substrates [83]. In this system, a postannealing of the deposited Fe is possible because no intermixing is observed at the substrate/film interface. The insulating character of the MgO substrate, however, prevents its application in a photoemission experiment due to charging effects.

surface region[4]. Each peak intensity is integrated after a Shirley background subtraction and weighted by the energy-dependent photoionization cross sections [58, 59]. We thus obtained an As content of roughly $6 \pm 5\%$ and a Ga content of $0.06 \pm 5\%$ within the upper 4 monolayers. This result is consistent with studies by Carbone *et al.*, who monitored the core level intensities as a function of the Fe coverage (0-75 ML) on a GaAs(110) substrate [72]. The GaAs(110) face is not known to form reconstructions, in contrast to the Ga(001) surface. The authors investigated the Ga and As content of the surface with increasing Fe film thickness and found the attenuation of the As $3p$ core level being much slower than the emission from Ga $2p$ levels, indicating an As out-diffusion and surface segregation. Nevertheless, the authors stated that a small amount of As was still detectable at the surface at the highest coverage of 75 ML. Comparing these findings our results, the (4x6) reconstruction of the GaAs face is found to reduce the As content by more than a factor of two.

4.2.1 Magnetism of Fe/GaAs(001)

The magnetic measurements of the Fe(27ML)/GaAs films are intended to reveal the orientation of easy and hard axis of the ferromagnetic film in order to define a quantization axis for the spin detection during the PES experiment. It has been found by a number of groups, that a large in-plane uniaxial magnetic anisotropy is present in thin Fe films, which have been epitaxially grown on GaAs(001) [68,69]. Usually, a cubic bcc material like bulk Fe has a four-fold anisotropy, which arises from the four-fold crystalline anisotropy and becomes dominant for increasing Fe film thickness. If thin Fe are grown on a GaAs surface, however, the two-fold symmetry of the (001) surface of the zincblende crystal structure has to be taken into account [77]. It is assumed, that the orientation of the magnetic axes should be related to the alignment of the dimer rows at the reconstructed surface. One common feature of all types of reconstructions is that the uniaxial easy axis is perpendicular to the direction of the dangling bonds. Ga-terminated and As-terminated surfaces have easy uniaxial axes along $(\bar{1}10)$ and (110), respectively [77]. The in-plane anisotropy strongly depends on the thickness of the ferromagnetic layer since it reflects the reduced dimensionality of the film (interface anisotropy), compared to the four-fold anisotropy which is observed in bulk bcc Fe [77]. It has been found by Brockmann *et al.*, that beyond a Fe thickness of 75 ML on (4x6)-GaAs, the fourfold (cubic) easy axes of bulk Fe along (100) and (010) superimpose onto the uniaxial component [69].

The magnetic measurements in this work on the Fe(27ML)/GaAs(001) system are performed with a protective capping layer of 15 ML MgO. Magnetic hysteresis loops $M(H)$ are measured using the longitudinal magneto-optical Kerr effect at room temperature as shown in the Figures 4.3a and 4.3b. The magnetic field is applied along the $(1\bar{1}0)$ and (110) direction, respectively. No MOKE signal is expected from the semiconducting substrate[5] [62]. The loop in Figure 4.3 clearly shows a hysteresis, indicating a full development

[4]An approximation of the probing depth is deduced from the corresponding mean free path: Electrons excited from the As $3p$ level have a kinetic energy of about 40 eV, from Ga $3p$ about 65 eV and from Fe $3p$ approximately 32 Å. The inelastic mean free path ranges from 5.6Å to 5.8 Å, according to equation 3.7. We are thus probing the first 3-4 monolayers of the bcc Fe sample.

[5]The complete measured signal originates from the Kerr signal of the FM film and the Faraday signal

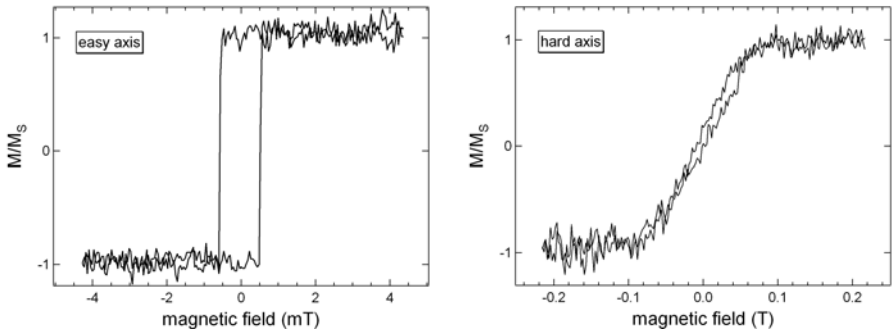

Figure 4.3: Magnetization loops of MgO(15ML)/Fe(27ML)/GaAs-(4x6) for the magnetic field applied along the ($\bar{1}10$) (easy axis) and (110) direction (hard axis), respectively.

of the ferromagnetic phase. The small coercive field $H_c = 1 \cdot 10^{-3}$ T (10 Oe) indicates a good crystalline film quality [70]. We identify the ($\bar{1}10$) direction as the easy axis, which is in accordance with previous studies. The magnetization loop along (110) is referred to the hard axis. This result clearly reveals the presence of a two-fold uniaxial anisotropy of the Fe(27ML)/GaAs films. We find no hints for the four-fold anisotropy being superimposed to the two-fold anisotropy by applying the magnetic field in (100) and (010) direction.

4.3 Co growth on Fe/GaAs(001)

In the context of this work, we investigate the electronic structure of bcc Co, which is closely related to that of the bcc-Fe system. Bcc-Co, however, is not a known thermodynamic phase which occurs naturally. The stable bulk phase at room temperature is the hcp structure, which persists up to a temperature of 425°C, at which it transforms to the face-centered cubic (fcc) structure [77]. Under specific geometrical and preparation conditions, bcc-Co can be stabilized as a thin epitaxial film.

Theoretical calculations predicted a minimal total energy for bulk bcc-Co at a lattice constant of 2.82 Å [125]. It has been shown, that this bcc phase is unstable against a volume-conserving tetragonal distortion. The energetic minimum of this metastable bct[6] phase is predicted for a distortion ratio of $c/a = 0.92$, where c is the lattice constant in growth direction and a is the in-plane lattice constant [124]. Consequently, epitaxial growth can stabilize the bct phase, until it reaches a critical thickness, at which the system structurally relaxes into the hcp structure. In practice, it is thus very difficult to stabilize a pure bcc Co film. The fact, that epitaxial bct-Co phases are usually strain-induced results in a variation of the experimentally observed distortion ratios c/a. For similar growth on the same substrates, different lattice parameters have been observed, which means that the

of the non-magnetic substrate, from which the light is reflected. The only magnetic response, however, arises from the thin ferromagnetic film.

[6]bct: body-centered tetragonal

exact structure depends strongly on the experimental conditions [124]. It is thus difficult to state a precise experimental lattice parameter for Co growth on Fe(001)/GaAs(4x6) from the literature.

There is some controversy on the maximum stability of bcc-Co. Most groups show stability limits in the range of 10-20 ML for various substrates and crystal orientations [124]. The exact value thereby depends on the growth method, interface preparation and deposition rate. A frequently used substrate is Fe(001), which provides a very small mismatch of 1.4% with respect to the in-plane bcc-Co lattice constant a. The highest stability for Co growth on Fe is found for deposition temperatures between room temperature and 200°C [124].

In our preparation procedure, we evaporated Co from an electron heated high-purity Co rod with a deposition rate of about 1.3 Å/min onto 27 ML thick Fe seed layers. The Co films are deposited at slightly elevated temperatures of about 80°C.

In order to determine the crystalline structure of the Co films as well as its stability, we take LEED images at various stages during the Co deposition. Figure 4.4 shows the LEED pattern of 3 ML, 11 ML, 15 ML and 17 ML thick Co films on Fe(001) taken at primary energies of about 52 eV. These first-order diffraction spots indicate the full epitaxial relation of Co on top of the Fe substrate. An increase of the background intensity is attributed to an enhanced surface roughness. It is found, that under the present preparation conditions, the Co lattice conserves its crystalline structure up to a coverage of about 16 ML. Beyond this thickness, we can observe the spots fading away, which indicates a loss of structural order of the Co film. The critical thickness of the Co layers in our investigations is in very good agreement with determinations of previous studies [123]. We mention, that the LEED analysis gives insights to the in-plane surface conditions, but provides no access to the vertical lattice dimensions. These restriction has to be kept in mind with regard to the interpretation of the electronic structure results in chapter 5.3.

Magnetism of Co/Fe/GaAs(001) It has been shown in section 4.2.1, that 27 ML Fe on (4x6) GaAs(001) exhibit a uniaxial anisotropy, which is caused by the asymmetry of the GaAs interface bonding. In order to investigate the magnetic properties of the Co/Fe/GaAs multilayer samples, magnetization curves are measured by MOKE on 12 ML Co/27 ML Fe/GaAs with 15 ML MgO on top. By applying the magnetic field in $(\bar{1}10)$ direction, the magnetization loop shown in Figure 4.4 reveals the presence of an easy axis, with a coercive field of about $H_c = 3.5 \cdot 10^{-3}$ T (35 Oe). As expected, the magnetization behavior is mainly that of the Fe/GaAs(001), with the coercive field H_c being enhanced. Generally, the latter depends on the structural perfection of the film, which in turn is determined by the growth conditions. An increase of H_c can be interpreted in terms of structural defects, which are supposed to hinder the motion of domains during the magnetization reversal.

The hard axis of the system is identified by applying the magnetic field in (110) direction (see Figure 4.4). The double-loop structure is due to the occurrence of quadratic MOKE-effects [77]. The Co/Fe/GaAs sample saturates at a magnetic field of about 0.03 T, which is obviously smaller compared to that measured for the Fe-based samples. The reduction of $H(M_S)$ is related to the smaller influence of the interface anisotropy, which decreases with increasing film thickness.

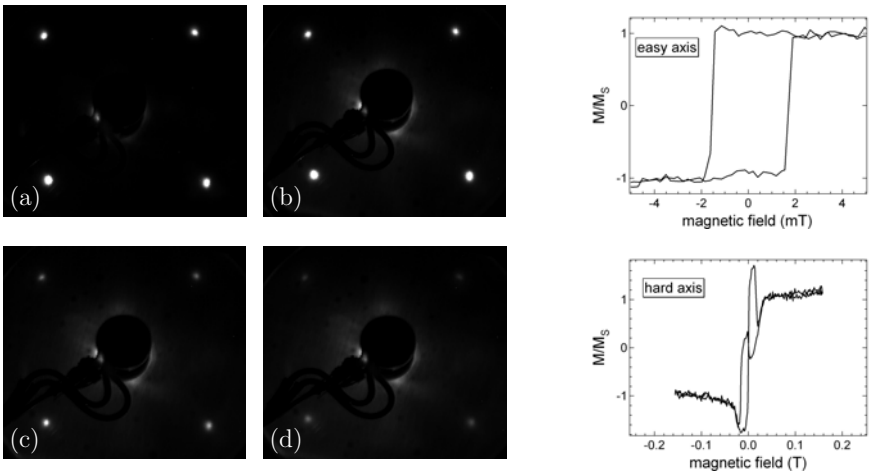

Figure 4.4: Left: LEED images of Co deposited on 27 ML thick Fe(001) films of bcc structure. The Co thickness varies from (a) 3 ML, (b) 11 ML, (c) 15 ML to (d) 17 ML Co. Right: MOKE magnetization loops of MgO(15ML)/Co(12ML)/Fe(27ML)/GaAs-(4x6) for the magnetic field applied in ($\bar{1}10$) (easy axis) and (110) direction (hard axis).

4.4 Ultrathin MgO_x on Fe(001) and Co(001)

The final preparation step involves the coverage of the Fe(001) and Co(001) surfaces with ultrathin MgO_x layers. Due to the very similar conditions of Fe(001) and Co(001) concerning lattice geometry and surface free energies, the main aspects of MgO epitaxy and growth are exemplarily discussed for MgO deposited onto a Fe(001) surface, since this material system is studied to a larger extend in the framework of this thesis. In the case of noteworthy differences regarding the Co(001) surface, these are explicitly mentioned in the text.

Several previous studies reported on the epitaxial matching between stoichiometric MgO and Fe [79–81]. The MgO lattice is found to be oriented with a 45° rotation between the Fe(001) and the MgO(001) unit cell axes (MgO[100] ∥ Fe[110]). The relatively small lattice mismatch between MgO and Fe of 3.8% in this configuration allows epitaxial growth in the initial stage. Structure studies suggested, that the Fe atoms are positioned on top of the oxygen atoms [83]. Due to the large difference of the surface free energies of Fe (2.9 J/m^2) and MgO (1.2 J/m^2), the initial stage of growth favors in principle a layer-by layer mode [84]. This two-dimensional growth is actually reported for smooth Fe surfaces, which have been postannealed after deposition [80]. The growth is predicted to proceed pseudomorphically up to a thickness of 4-6 monolayers [80, 84].

In our preparation process, granular Mg material is evaporated from a molebdynum crucible with a deposition rate of about 1.8 Å/min. The deposition is carried out at slightly elevated temperatures between 60°C and 80°C. Simultaneously, oxygen is let into the prepa-

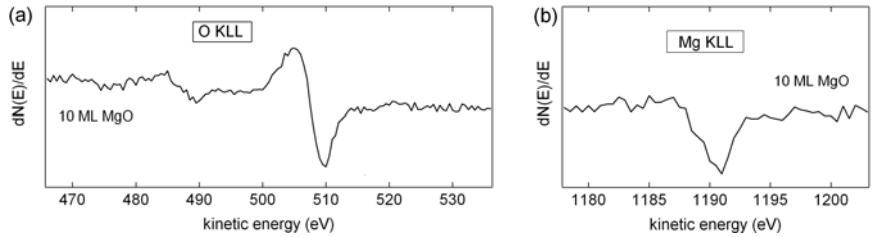

Figure 4.5: Auger spectra acquired with a primary energy of $E = 3$ keV after the deposit of 10ML MgO on Cu(001). (a) Oxygen KLL transitions and (b) magnesium KLL Auger transitions. From the comparisons of the corresponding peak-to-peak heights, the Mg/O ratio is obtained.

ration chamber via a leak valve in order to systematically control the oxygen supply. The actual amount of oxygen is estimated from the ion gauge reading. In comparison to an evaporation of MgO from polycrystalline material, we are thus able to consciously prevent an excess of atomic oxygen over Mg, which would favor the oxidation of the Fe(001) surface during the first stages of growth [16]. We find the evaporation of the pure Mg material being always accompanied by the evaporation of a non-negligible amount of MgO. This effect is reasonable, because the granular Mg material posses a large surface, which has been completely oxidized during its exposition to air. This causes a partial evaporation of MgO and thus gives raise to a small partial oxygen background. During the thermal evaporation process, the pressure in the UHV chamber rises up to 2×10^{-9} mbar.

A comment should be made on the film morphology, which is expected after the deposition of MgO and MgO_x. The first aspect concerns the Fe surface. As discussed in section 4.2, any postannealing of the Fe layer in order to smooth the surface has a detrimental effect due to a substrate/film intermixing. If the Fe film is not postannealed, as being the case in this work, the surface may reveal the presence of three-dimensional islands. The subsequent growth of MgO layers, although considered as layer by layer-type from thermodynamical considerations [84], covers the Fe surface by enveloping the three-dimensional island or forming new ones. In the case of very thin coverages in the monolayer regime, parts of the Fe layer may thus remain uncovered. Another aspect concerns the actual growth mechanism of under-oxidized MgO onto the Fe surface. To our best knowledge, this process has not yet been studied by suitable methods. One might suppose, that the surplus of metallic magnesium enhances the surface free energy of the MgO_x composition (see Figure 2 in Ref. [82]) and thus makes a layer-by-layer growth on bcc Fe less favorable. From energetic considerations, however, it still seems reasonable to assume an identical positioning of Mg and O atoms on top of the bcc Fe surface. Nevertheless, these considerations have to be kept in mind for the valence band photoemission experiments.

The crucial parameter regarding the ensuing experiments at the MgO_x/Fe and MgO_x/Co interface is given by the MgO degree of oxidation. Depending on the amount of oxygen atoms which are provided during the growth of the MgO_x layers, a partial, a complete or an over-oxidation will take place. These situations, an oxygen deficiency (=excess of

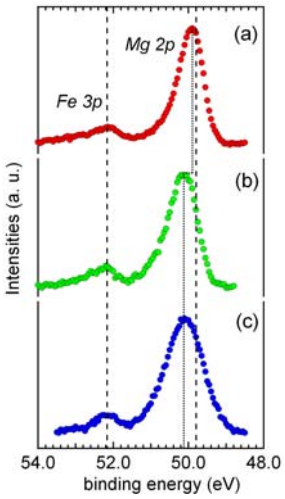

Figure 4.6: Core-level photoemission spectra of the Fe $3p$ and Mg $2p$ levels recorded at a photon energy of $h\nu = 88.3$ eV. (a) Oxygen-deficient MgO layer, (b) nearly stoichiometric MgO and (c) subsequently oxidized (over-oxidized) MgO capping layer.

magnesium) and excess of oxygen are not equivalent, since in case of an over-oxidation, the remaining oxygen atoms may be able to interact with the Fe surface layer.

As a preliminary experiment, an estimate of the oxygen dose, which has to be applied in order to obtain a nearly stoichiometric Mg:O composition, is obtained by AES. Mg is evaporated onto a Cu(100) substrate at a rate of 1.8 Å/min with a partial oxygen pressure of about $p_{O_2} = 1 \times 10^{-8}$ mbar. Figure 4.5 displays the corresponding O KLL transition at 510 eV and the Mg KLL Auger line at 1191 eV at a coverage of 10 ML MgO. A comparison of the O(KLL)/Mg(KLL) Auger intensity ratios, which are weighted by their sensitivity factors, reveals a Mg:O ratio of 47%:53%. Thus, nearly the same amount of oxygen and Mg atoms are present in the surface near area.

The degree of oxidation at the MgO_x/Fe and MgO_x/Co interface is investigated by core-level photoemission spectroscopy. The Fe $3p$ and Mg $2p$ core levels, located at 52.2 eV and 49.8 eV, are excited with photons of an energy $h\nu = 88.3$ eV. Due to the very low kinetic energy of the photoelectrons of about 35 eV, a surface sensitivity of approximately 4 Å probing depth is provided by the experiment. Since the photoionization cross section σ_i is much higher for the Mg $2p$ level ($\sigma_i = 60$ mbarn) than for the Fe $3p$ level ($\sigma_i = 1$ mbarn) [58], the Mg $2p$ feature dominates in intensity even at low coverages. As has been discussed in chapter 3.5, the oxidation of the Mg atoms leads to a chemical shift of the Mg^0 $2p$ level towards higher binding energies. The quantification of the oxidation ratio Mg^{2+}/Mg^0 is easily accessible from the peak areas of the fitted Mg^{2+} and Mg^0 features. A quantitative conclusion, whether a partial oxidation of the Fe surface has taken place, can only inadequately be deduced from the Fe $3p$ peak position and shape[7]. As we will see in

[7]The beamline 5 at the storage ring DELTA, where all photoemission experiments have been performed,

chapter 5.2.2, the interaction between oxygen and the Fe surface can be unambiguously deduced from an induced exchange splitting on the oxygen $2p$ valence bands.

Oxygen-deficient MgO If Mg is deposited with just minimal additional oxygen supply (less than $p_{O_2} < 2 \times 10^{-9}$ mbar), the analysis of the Mg $2p$ and Fe $3p$ core levels reveals an oxygen deficiency of the MgO layer. The corresponding core-level spectrum of an oxygen-deficient MgO layer is exemplarily shown for a one ML thick MgO_x film in Figure 4.6. The secondary-electron background is subtracted from the spectrum by applying the Shirley algorithm. The position of the Mg $2p$ feature indicates a partial oxidation of the Mg layer due to the leftward shift of the Mg $2p$ peak center towards a higher binding energy E_B relative to the Mg^0 $2p$ level. Furthermore, the unshifted position of the Fe^0 $3p$ level indicates, that no oxidation of the Fe interface layer has taken place. The oxidation ratio is quantified by fitting two spin-orbit split Gaussian/Lorentzian line shapes for the Mg^{2+} and Mg^0 state. Figure 4.7 clearly displays a nearly equal distribution of oxidized Mg^{2+} and metallic Mg^0 atoms. The Mg^0 peak position is thereby fixed to E_B=49.8 eV whereas the remaining parameters, Mg^{2+} position, relative intensity and full-width at half maximum (FWHM) are allowed to vary within reference-based intervals [85]. Exemplarily, the oxidation ratio for under-oxidized MgO was estimated from the ratios of the peak areas as being $Mg^{2+}/Mg^0 \approx 0.52/0.48$.

Nearly stoichiometric MgO In order to obtain a nearly stoichiometric composition Mg:O, an approximate estimation of the partial oxygen pressure ($p_{O_2} \approx 1 \times 10^{-8}$ mbar), which has to be supplied during Mg deposition, is obtained by AES (see previous section). In order to prevent the formation of a premature FeO layer, Mg is evaporated in the submonolayer regime (approx. 0.2-0.4 ML), before the oxygen is admitted into the chamber. The result of this procedure yields a completely oxidized MgO layer, as can be deduced from the complete leftward shift of the Mg $2p$ feature in Figure 4.6. In order to quantify the amount of oxygen atoms, which have been oxidized by this preparation step, a representative Mg peak fit is shown in Figure 4.7. In comparison to the under-oxidized MgO layer, a clear difference of the corresponding peak areas A and B is observable. In agreement with the further leftward shift of the peak maximum, a displacement of intensity takes place and results in an enhanced oxidation ratio of $Mg^{2+}/Mg^0 \approx 0.88/0.12$. This results stand representative for a nearly stoichiometric MgO composition.

Over-oxidized MgO An oxygen excess at the Fe(001)/MgO interface is generated, if the deposition of under-oxidized MgO_x is followed by a subsequent oxygen exposure of approximately 1 L (1 langmuir (L)=10^{-6} torr for 1 sec). This procedure yields a complete oxidation of Mg atoms, as visualized by the chemical shift of the Mg peak maximum towards the Mg^{2+} $2p$ level in Figure 4.6. Moreover, the broadening of the Fe $3p$ peak is a first hint for the presence of partially oxidized Fe $3d$ atoms within the Fe surface layer. This finding stands in agreement with theoretical and experimental studies, which report

gives no access to photon energies higher than 400 eV. Therefore, the Fe $3p$ level instead of the more intense Fe $2p$ peak at 720 eV was observed.

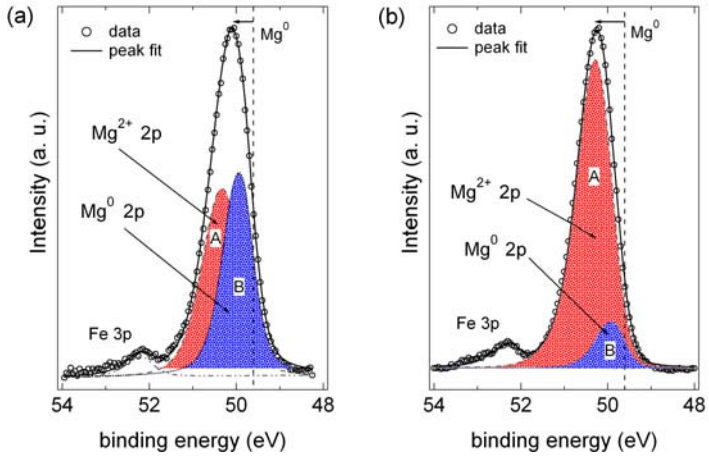

Figure 4.7: Core-level photoemission spectra of the Fe $3p$ and Mg $2p$ levels recorded at a photon energy of $h\nu = 88.3$ eV. (a) Mg $2p$ peak of an oxygen-deficient MgO layer. By fitting the Mg^0 and Mg^{2+} areas an oxidation ratio of $Mg^{2+}/Mg^0 \approx 0.52/0.48$ was obtained. (b) Mg $2p$ peak of a nearly stoichiometric MgO layer with an oxidation ratio of $Mg^{2+}/Mg^0 = 0.88/0.12$.

that during adsorption of low oxygen coverages, O_2 molecules spontaneously dissociate on the sample surface and partially incorporate below the Mg top layer [86, 87].

The preceeding experiments revealed the probability of classifying the actual MgO degree of oxidation for each sample uniquely by employing low-energy core-level photoelectron spectroscopy. In the following experiments, we will refer to three different classes: i) the under-oxidized, ii) the nearly stoichiometric and the iii) over-oxidized FM/I interface. The electronic structure of these systems will be investigated in the following chapter.

4.5 Summary

In the previous sections, the successive preparation steps yielding the MgO_x/Fe(001) samples, which are designed to determine the electronic structure of their FM/I interface, have been presented. An analysis of the crystalline structure, the magnetic anisotropy of the thin ferromagnetic films and the chemical environment at the surface and of MgO_x give access to various parameters being relevant for a thorough characterization of the samples.

All films are prepared on well-defined GaAs(001) crystal surfaces. The preparation of GaAs was discussed with respect to the actual type of surface reconstruction. The presented preparation method results in a Ga-rich surface of (4x6) symmetry. The Ga-termination of the GaAs substrates has been confirmed by Auger electron spectroscopy.

On these (4x6)-GaAs(001) substrates, the deposition of thin Fe films of a thickness of 27 ML has been performed. The crystalline structure of the 27 ML thick Fe films has been investigated by LEED and displays a well-ordered cubic lattice. The difficulty of As

segregation was addressed by monitoring the $3p$ core levels of Fe, Ga and As by means of low-energy core-level spectroscopy. As was reported in previous studies, a small amount of arsenic is found to segregate to the Fe surface region.

Magnetic measurements on 15ML MgO/27ML Fe/GaAs, using the magneto-optical Kerr effect, reveal a two-fold in-plane anisotropy of the ferromagnetic layer, which is typically observed for thin ferromagnetic films grown on a semiconducting surface. We find no contributions of the four-fold anisotropy being superimposed to the two-fold anisotropy. Thus, we are able to perform spin-resolved photoemission experiments with respect to the quantization axis, which is given by the easy axis of the thin Fe film.

The structural analysis of Co films deposited on 27 ML Fe reveals a full epitaxial match on the latter. We observed the crystalline structure being conserved up to a critical thickness of about 16 ML, which is in close agreement with previous experiments. The magnetic measurements on a 12 ML thick Co film indicate a magnetization behavior comparable to that of the Fe-based system.

The degree of oxidation of the MgO_x overlayers represents a crucial parameter in the context of this thesis. It is addressed by means of core level spectroscopy which monitors the Mg $2p$ and Fe $3p$ levels. The chemical shift of the Mg $2p$ level towards higher binding energies is found to indicate a good measure for the degree of oxidation. A quantification of the latter is deduced from fitting the Mg $2p$ core levels by Gaussian-Lorentzian sum functions. This enables one to classify each particular sample concerning its interface chemistry.

Chapter 5

Electronic Structure of MgO_x/Fe(001) and MgO_x/Co(001) Interfaces

It is a well established fact, that the spin-dependent tunneling process in magnetic tunnel junctions is an extremely interface sensitive phenomenon. Important insights into the physical mechanisms involved are provided by theoretical studies, which recognized the electronic structure of ferromagnet/insulator boundaries as acting crucial in controlling the matching of electronic wavefunctions and the magnitude of the tunneling spin polarization in epitaxial FM/I/FM junctions. These considerations, however, hold for perfectly sharp and well-ordered interfaces, which cover the experimental situation only to a minor extent. A real interface prepared, for example, by molecular beam epitaxy usually exhibits deviations from ideality. In particular, oxygen defects or oxygen excess must play a key role at FM/I interfaces in real MTJs with oxide barriers.

It is reasonable to assume, that a modification of the interface stoichiometry can significantly affect the chemical bonding between ferromagnet and insulator. As a consequence, a redistribution of the interfacial spin-polarized electronic states can take place, which changes the properties of the electronic structure at the interface. This, in turn, is directly reflected by the interfacial ground state spin polarization at the Fermi level and has direct consequences for the spin-dependent tunneling process.

In order to gain deeper insight into the electronic states of real interfaces and the physical mechanisms, which govern the interfacial spin polarization, this thesis addresses in detail the electronic structure of ferromagnet/insulator interfaces on the basis of spin- and angle-resolved photoemission spectroscopy. The photoemission studies presented in this chapter focus in particular on the response of the electronic system of the ferromagnetic layer in contact with MgO overlayers of different oxide stoichiometries. The interplay between chemical bonding and electronic structure formation is analyzed by combining results from core-level and valence-band photoemission spectroscopy. By relating the MgO degree of oxidation extracted from the Mg $2p$ core level shifts to modifications of the ferromagnetic $3d$ valence bands, a profound dependence of the interfacial spin polarization on the interface chemistry becomes evident. The complex behavior of the electronic structure is interpreted with regard to possible models of the interface atomic environment, which reflect the type

of interfacial bonding mechanisms.

5.1 Introductory remarks

The idea underlying the following photoemission experiments is based on the fact, that the electronic structure of a ferromagnetic sample can be probed through an ultrathin MgO overlayer, since the valence bands of ferromagnet and insulator are located at different energetic positions with respect to the Fermi level. Whereas the valence states of Fe and Co are entirely dominated by $3d$ contributions at the Fermi energy, electronic states attributed to MgO valence bands are located at binding energies of about $E_B = -3.5$ eV and below [102]. This behavior reflects the metallic and insulating character of both material classes, and enables an observation of the ferromagnetic $3d$ states in contact with MgO within an energy window between the Fermi level and the onset of the MgO valence band maximum.

With increasing MgO thickness, however, the photoemission signal arising from the ferromagnetic layers is attenuated. In order to be particularly sensitive to the interface of FM/I samples, the overlayer thickness and the photoelectron's attenuation length have to be delicately balanced. In the following experiments, the FM or FM/I systems are probed by photons with energies between 34 eV and 40 eV. According to equation (3.7), the attenuation length λ of photoelectrons originating from the ferromagnetic $3d$ states is approximately 4 monolayers. The total number of photoelectrons that leave the crystal depends exponentially on the thickness d of the traversed film $I = I_0 \exp(-d/\lambda)$. Thus, the major contribution of the photoelectron signal for an uncovered Fe or Co film is indeed originating from the very first atomic layers. By choosing the MgO coverage in an ultrathin monolayer regime (1-2 ML), modifications induced by the MgO overlayer on the ferromagnetic $3d$ electronic states at the interface are observable within the energy window below the Fermi level, because the MgO layer conserves the orientation of the photoelectron spin.

All photoemission experiments presented in the following chapter have been performed under similar conditions. The excitation of photoelectrons is accomplished with p-polarized light, which impinges on the sample at an angle of 45°. The electrons are collected in normal emission direction. According to the dipole selection rules introduced in chapter 2.2.2, the experiments provides access to initial states of Δ_1 and Δ_5 symmetry along the Γ-Δ-H line of the bcc reciprocal lattice space. The final state possesses a Δ_1 symmetry, into which both electrons of either Δ_1 or Δ_5 symmetry are excited. The energetic resolution is set to 200 meV, which is sufficient to clearly separate the exchange split valence bands. An angular acceptance of $\pm 6°$ allows the data interpretation in terms of normal emission ($\mathbf{k}_\parallel = 0$). We assume a constant secondary-electron background of the order of 5% and normalize the spectra to the count rate maximum.

In the present geometry, the photoemission experiment probes ferromagnetic electronic states, which are considered as being involved in a tunneling transport process in Fe- and Co-based MTJ devices with MgO barriers. As has been discussed in chapter 2.3.2, the spin-tunneling process in these systems involves electrons with a wavevector $\mathbf{k}_\parallel = 0$. Thus, photoemission along the Δ-line can probe relevant initial states and extract information about their spin polarization. Moreover, the experiment aims at being particularly sensi-

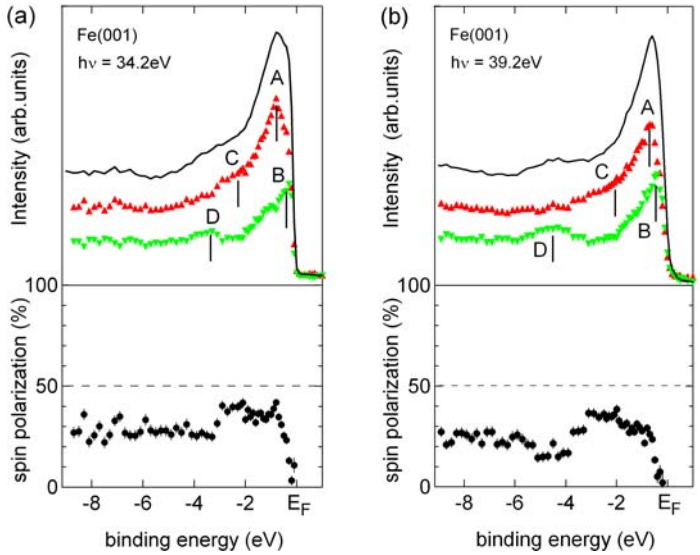

Figure 5.1: Photoemission spectra and spin polarization distributions from bcc-Fe(001) recorded in normal emission geometry. The samples have been excited with p-polarized light ($h\nu = 34.2$ eV (a) and 39.2 eV (b)) incident at 45° with respect to the surface normal. Solid line: spin-integrated data, ▲ denotes majority spin electrons (↑), ▼ denotes minority spin electrons (↓).

tive to changes of the electronic structure of MgO_x/Fe(001) and MgO_x/Co(001) interfaces evoked by modifications of the chemical bonding. It is therefore reasonable to address those ferromagnetic 3d bands, which lie closest to the Fermi level. For this purpose, the photon energy has to be chosen adequately. In the following sections, we will show that the spin polarization of these electronic states is sensitively controlled by the stoichiometry of the overlaying MgO barrier.

5.2 The MgO_x/Fe(001) interface

5.2.1 Electronic structure of bcc-Fe(001)

The initial experiments are dedicated to characterize the spin-resolved 3d electronic structure of the uncovered Fe(001) surface. The knowledge of the energetic positions, spin character and spectral weight of the valence band features is of major importance, since any MgO_x-induced modifications of the electronic structure at MgO_x/Fe interfaces will be compared to the Fe(001) reference. In particular, we are interested in the sign and magnitude of the spin polarization of electronic states directly at the Fermi level.

The photoemission experiments are carried out on 27 ML thick bcc-Fe films, which

have been deposited on well-defined (4x6)-GaAs(001) surfaces. Further details on the preparation steps and the *in situ* characterization can be found in chapter 4.2. Figure 5.1 shows exemplarily the results of the spin-resolved photoemission experiments on bcc-Fe(001). The spectra have been recorded at photon energies of $h\nu = 34.2$ eV and 39.2 eV, respectively. The spin-integrated intensities (full lines) and spin polarization spectra are displayed together with the partial intensities of majority and minority spin electrons, which have been calculated using equation (3.9). In the energy regime ranging from -4 eV up to the Fermi level, the entire electronic structure can be attributed to the spin-polarized Fe 3*d* valence bands. Whereas the features at the Fermi level do not exhibit any dispersion with $\mathbf{k}_\perp$, a weak dispersive peak is observed at higher binding energies above $E_B = -3$ eV.

By comparing the experimental binding energies of the partial intensities to a band structure calculation within the three step model, the spectral features can be associated with particular initial states. Moreover, this procedure enables one to assign a symmetry character to the observed peaks, which is of interest for the interpretation of bonding mechanisms in the following sections. However, a constriction of this procedure should be mentioned in advance: Whereas the band structure calculation refers to the electron ground state, the photoemission experiment samples an excited state of the (N-1) electron system. Therefore, the unoccupied states computed in a bandstructure calculation cannot be interpreted as excited states of the system, as well as the occupied states do not give the real binding energies. In order to identify the initial states of the spin-resolved spectra, the comparison with the bulk bandstructure seems to be appropriate despite these limitations.

For this purpose, the spin-polarized bandstructure of a bulk Fe(001) system has been calculated in an energy interval of $-10\,\mathrm{eV} < E_F < 40\,\mathrm{eV}$ (see Figure 5.2) by assuming the experimental lattice constant of $a_{\mathrm{Fe}} = 2.86$ Å. The symmetries of the bands are labeled in the notion of a single-group representation, which has been introduced in chapter 2.1.3. The unoccupied band structure at higher binding energies is supposed to resemble that of the dispersion of nearly free electrons, and thus has at least the correct topology of the real final states.

The comparison of the partial intensities in Figure 5.1 and the bandstructure shown in Figure 5.2 leads to the following identification of the initial states: In the order of increasing binding energy, the first peak below the Fermi energy is of minority character and located at a binding energy of $E_B = -0.3 \pm 0.2$ eV. This feature is ascribed to the direct transition from the $\Delta_5^\downarrow$ band lying flatly below E_F (henceforth labeled **B**). The following features appear in the majority spectra: One peak is located at a binding energy of $E_B = -0.7 \pm 0.2$ eV (labeled **A**) and a peak shoulder is positioned at $E_B = -2.5 \pm 0.2$ eV (labeled **C**). These features are assigned to photoemission contributions from $\Delta_1^\uparrow$ and $\Delta_5^\uparrow$ symmetry bands, respectively. Since they do not exhibit a dispersion with $\mathbf{k}_\perp$, they are observable simultaneously in the spectra recorded at 34.2 and 39.2 eV. Finally, a feature labeled **D** is located at $E_B = -3.4 \pm 0.2$ eV and $E_B = -4.5 \pm 0.2$ eV in the spectra recorded at 34.2 eV and 39.2 eV, respectively. It originates from a strongly dispersive $\Delta_1^\downarrow$ band, which starts at the Γ-point. The peaks at $E_B = 0.3 \pm 0.1$ eV (**B**) and $E_B = -2.4 \pm 0.2$ eV (**C**) are due to emission from the exchange-split $\Delta_5^\downarrow$ and $\Delta_5^\uparrow$ bands, which are separated by a value of $\Delta_{xc} = 2.1 \pm 0.2$eV. The above findings are in good agreement with previous photoemission studies on Fe(001) as presented, for example, in Ref. [91]. Moreover, the observed average exchange splitting of the Δ_5 bands is in agreement with theoretical predictions in Ref. [92]

and [93] at the Γ-point. The results indicate, that the agreement of experiment and theory is very reasonable.

An important issue concerns the question, whether a surface state contribution might be superimposed on the observed 3*d* bulk-related features. These states are by definition localized at the surface of a sample and confined to two dimensions [95]. This implies, that the binding energy does not depend on the photon energy for a fixed value of $\mathbf{k}_\parallel$. Moreover, surface states are strongly affected by the surface conditions, i.e. small doses of adsorbants will effectively quench a surface state. In our experiments, none of these indications are observed: In particular, as will be shown in section 5.2.2, no particular peak of the spectra is noticeably suppressed when the surface is exposed to small doses of gaseous oxygen. Moreover, results from scanning tunneling spectroscopy (STS) experiments identify localized d_{z^2} surface features at Fe(001) surfaces at +0.17 eV above the Fermi energy, which shift to even higher energies upon contact with isolated oxygen impurities [96,97]. Further surface resonances are found to be located more than 2 eV below the Fermi level [98]. We thus exclude that any surface state is superimposed on the observed Fe 3*d* valence bands and conclude, that the Fe(001) samples reveal a fully bulk-like electronic structure.

The spectra of the spin polarization distributions $P(E)$ in Figure 5.1 reveal a positive value of P at the Fermi level E_F. This is due to the high spectral weight of the majority spin feature of Δ_1 symmetry, which overlaps with the minority peak originating from the $\Delta_5^\downarrow$ band. Summarizing all measurements on Fe(001) surfaces, the typical spin polarization P within an interval of $-2\text{eV} < E_B \leq E_F$ is found to be positive with a magnitude of the order of $40\% < P < 50\%$ for spectra recorded at photon energies $h\nu$ =34.2 eV, and $30\% < P < 40\%$ for $h\nu$ =39.2 eV.

Obviously, the magnitude of the spin asymmetry P decreases with increasing photon energy. This behavior was also observed in previous photoemission studies on Fe(001) by Kisker *et al.*, who found strong changes in the spectra between photon energies of 20 and 60 eV [91]. In this study, the intensity of the minority Δ_5 peak just below the Fermi level suddenly drops at photon energies below 33 eV. This effect is due to the fact, that the band of $\Delta_5^\downarrow$ character is only partly filled and intersects the Fermi level around $\mathbf{k}_\perp \approx 0.5$, as can be seen in Figure 5.2. Hence, direct interband transitions will occur only at $\mathbf{k}_\perp < 0.5$ and require photon energies above 33 eV to reach the final state parabola, which starts at H. From this finding we can draw the conclusion, that the photoemission experiment probes electronic states of the Δ_1 and Δ_5 bands along Γ-Δ-H, which are directly located at the Fermi level.

In summary, the photoemission experiments on uncovered bcc-Fe(001) samples reveal the spin-split electronic structure of the 3*d* valence bands. We demonstrated the absence of surface-related features, which indicates the presence of a fully bulk-like electronic structure. An analysis of the spin polarization indicates that we probe electronic states in the left half of the Brillouin zone along $\Gamma - \Delta -$ H, which are located directly at the Fermi energy. This finding is in good agreement with previous photoemission studies on bcc-Fe(001) [91]. The magnitude of the spin polarization P at the Fermi level serves as a reference for the following experiments on MgO_x/Fe(001) interfaces.

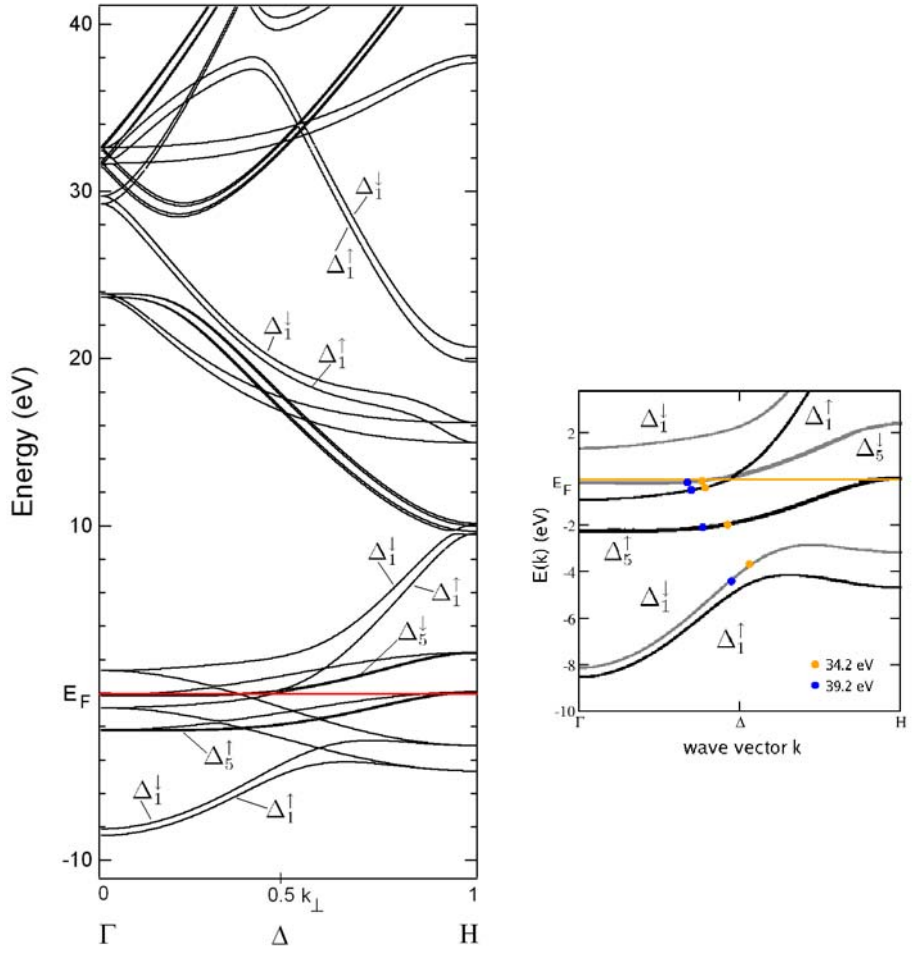

Figure 5.2: Bulk Fe(001) band structure calculated by using the SPR-KKR method [23]. Inset: Zoom into the valence band region around the Fermi level. Under the present experimental conditions, the Δ_1 and Δ_5 initial state can be addressed. Black lines: majority spin, grey lines: minority spin. The possible initial states are denoted by red ($h\nu = 34.2$ eV) and green ($h\nu = 39.2$ eV) dots.

5.2.2 Electronic structure of MgO_x/Fe(001)

The following photoemission experiments focus on the investigation of the Fe 3*d* electronic structure in contact with ultrathin MgO_x overlayers, with the degree of oxidation x thereby representing the critical parameter. Beyond the idealistic model of FM/I interfaces with nearly stoichiometric MgO coverages, the idea of examining more realistic interfaces is connected to the question, which modifications should be expected from an oxygen deficiency or oxygen excess at the FM/I boundary.

In order to gain a deeper insight into the physical mechanisms involved, the electronic structures of nearly stoichiometric, over-oxidized and oxygen-deficient MgO_x/Fe(001) interfaces are investigated in the following sections. Since the samples are also analyzed with respect to a Mg 2*p* core-level shift (see chapter 4.4), the experiments allow one to extract detailed information on the electronic structure as a function of the interface chemistry.

Nearly stoichiometric MgO on Fe(001): The model system

In the present section, we focus on the evolution of the Fe 3*d* electronic structure in contact with nearly stoichiometric MgO. As discussed in chapter 4.4, we identify the MgO stoichiometry from the shift of the Mg 2*p* level towards the Mg^{2+} 2*p* binding level. No preliminary hint for an oxidation of the Fe surface can be deduced from the energetic position of the Fe 3*p* core-levels.

The modification of the electronic structure of the MgO/Fe(001) system is investigated at a photon energy of $h\nu = 34.2$ eV. Figure 5.3 a-c displays the spin-resolved photoemission spectra of MgO/Fe samples as a function of the thickness of the nearly stoichiometric MgO. The latter thereby ranges from (a) 1.25 ML, (b) 1.65 ML to (c) 2.05 ML. All spectra are normalized to the $\Delta_1^{\uparrow}$ feature (**A**). Due to the increasing overlayer thickness, the Fe 3*d* valence states close to the Fermi level are increasingly attenuated in intensity in comparison to the uncovered Fe film. The energetic positions of the $\Delta_1^{\uparrow}$ and $\Delta_5^{\downarrow}$ feature thereby remain unchanged. A comparison of the spectra with that of an uncovered Fe layer (see Figure 5.1 a) indicates the existence of additional spectral features below a binding energy of -3.5 eV, which can be ascribed to the MgO valence band (labeled **O**) [101]. It is assumed, that the Fermi level lies in the middle of the MgO band gap. Thus, our findings are in good agreement with previous studies, which reported on an experimental MgO band gap of about $E_g = 7.9$ eV [84].

In order to identify an electronic interaction between the oxygen atoms of the MgO overlayer and the Fe surface, it is appropriate to analyze the spin-resolved photoemission contributions of the O 2*p* peaks (labeled **O**): Any occurrence of an induced exchange splitting in features, which originate from non-magnetic atoms in contact with a ferromagnet, represents a clear indication for a magnetic interaction between both atomic species [109]. Figure 5.3 a-c demonstrates, that the MgO valence band features do not exhibit any exchange splitting, i.e. the peak maxima of the minority and majority **O** features are centered about a binding energy of $E_B = -6$ eV. In the present case, we can thus exclude a magnetic interaction at the MgO/Fe interface.

We find the spin polarization distributions P in the energy window -3.5 eV $< E_B < E_F$ being remarkably similar to that of an uncovered Fe film (Figure 5.1 a). In particular, the magnitude of the spin polarization at the Fermi level remains practically unchanged.

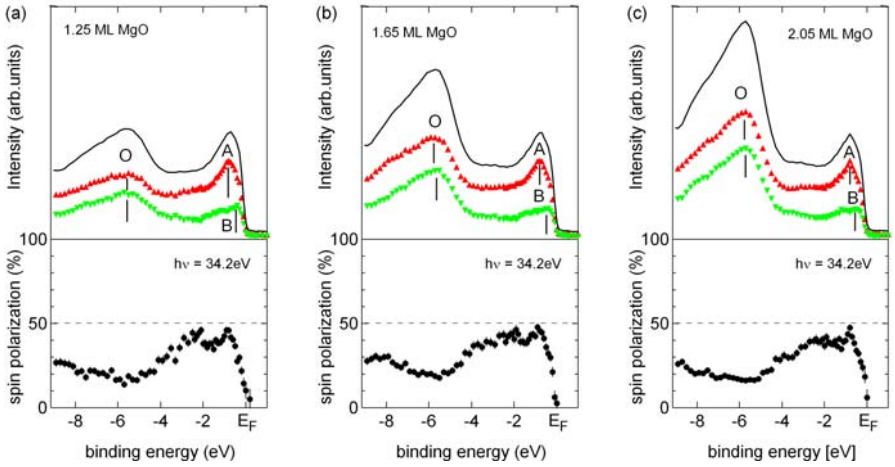

Figure 5.3: Photoemission spectra and spin polarization distribution for nearly stoichiometric MgO on Fe(001) for different overlayer thicknesses, recorded at a photon energy $h\nu = 34.2$. Solid line: spin-integrated data, ▲ denotes majority spin electrons, ▼ denotes minority spin electrons.

Generally, any formation of an interfacal chemical bond is associated with a modification of the electronic structure. In particular, the bonding process would involve the $3d$ valence electrons of the ferromagnetic layer, and consequently, the most significant charge rearrangement is expected to occur directly at the Fermi level. Since this is obviously not the case in the spectra investigated, we are led to conclude, that there is only a negligible interaction between the Fe and MgO overlayer. One can easily understand this finding from a chemical point of view: Saturated MgO bonds are known for a low reactivity and a weak tendency to oxidize an adjacent metal [102]. The strong ionicity of the bonding minimizes an interfacial electron transfer and limits the influence of one material upon the other.

These results are in good agreement with theoretical studies. Li and Freeman calculated the electronic structure of one monolayer of Fe on top of a MgO(001) substrate, standing representative for an ideally epitaxial Fe/MgO system [101]. The authors predicted a negligible hybridization between Fe and MgO. It was found, that the charge density of both substrate and overlayer remains nearly unchanged (with a charge transfer of less than 0.02 e/atom), thus forming an extremely noninteractive interface. The lack of electronic interaction between Fe and MgO could additionally be deduced from the shape of the spin density of the oxygen $2p$ states at the interface, which is only slightly influenced by the magnetic Fe overlayer. Thus, the studies ruled out a sizeable direct magnetic and chemical interaction between Fe and MgO, in accordance with our observations.

On the experimental side, the presented results can be discussed with regard to two other independent photoemission studies on the electronic structure of bcc Fe(001) covered by stoichiometric MgO. Experiments by Matthes *et al.* were performed in a spin-resolved

mode, whereas the studies by Sicot *et al.* were obtained in a spin-integrated experiment [99, 100]. The spin-resolved measurements by Matthes *et al.* support the proposed picture of a weak interacting MgO/Fe interface: The measured Fe spin polarization in these studies is not destroyed by a top MgO barrier. Beside, both authors reported on the following mechanism: With increasing thickness of the MgO layer, the attenuation of spectral weight for the direct transition from the $\Delta_5^\downarrow$ band (feature **B**) is stronger than that originating from the $\Delta_1^\uparrow$ states (feature **A**).

In agreement with their findings, our experiments indicate a comparable behavior for nearly stoichiometry MgO coverages as illustrated in Figure 5.3. Apart from a general attenuation in intensity, the spectra for 1.25 ML and 2.05 ML MgO coverage show a small relative intensity difference of the 3*d* $\Delta_5^\downarrow$ (**B**) compared to the $\Delta_1^\uparrow$ (**A**) spectral features. The energetic positions thereby remain unchanged. The relative attenuation of the $\Delta_5^\downarrow/\Delta_1^\uparrow$ peaks is of the order of 13%, if the MgO thickness is enlarged by about 60%. This is in accordance with the results by Matthes *et al.*, who found a relative reduction of the $\Delta_5^\downarrow/\Delta_1^\uparrow$ states of almost 20% for an increase of the MgO thickness by a factor of 2.

We point out, that this behavior is not understandable by only considering the particular initial state symmetries of the photoelectrons involved in the photoexcitation process. The photoelectrons excited from the two initial states in question, the majority Δ_1 and minority Δ_5 states, each possess the same probability of being excited into a Δ_1 final state with increasing MgO thickness. This argument is based on the fact, that the strength of a particular photoelectron transition is determined in the corresponding transition matrix element, which describes an intraatomic process. Once the excited photoelectrons reach the final state and are released into the crystalline (Fe) system, they form a spin-polarized current which propagates through the MgO barrier, before entering the vacuum. While passing the MgO layer, it is reasonable to exclude spin-flips or a spin-selective scattering of the photoelectrons.

At this point, one may speculate about possible mechanisms, which lead to the enhanced attenuation of the Fe 3*d* $\Delta_5^\downarrow$ feature with increasing MgO thickness. One may draw an analogy to the ideas discussed in chapter 2.3.2: It is known, that ferromagnetic wavefunctions couple with different strength to the MgO electronic structure at Fe/MgO interfaces. Theoretical predictions report on a preferred transmission for Δ_1 states through the MgO band gap, since they possess the slowest decay rate among all participating states. Although these considerations concern the energy regime around the Fermi level, it is tempting to assume an analogue mechanism in the unoccupied band structure, which is interspersed with energy gaps as well. We propose, that the observed attenuation of $\Delta_5^\downarrow$ spectral weight could be related to a reduced transmission probability of the corresponding electronic states of the photoelectrons while passing the unoccupied band structure of the MgO layers.

In summary, we find that the Fe(001) electronic structure is mainly chemically and magnetically conserved by being covered with nearly stoichiometric MgO. This finding is in good agreement with theoretical predictions and comparable experiments. The effect of a disproportionate reduction of the Fe 3*d* $\Delta_5^\downarrow$ state in comparison to the $\Delta_1^\uparrow$ state with increasing MgO thickness is suggested to originate from the symmetry selective electron transport in oxide layers, in analogy to theoretical predictions. Although this effect is relatively small, it can influence the magnitude of the measured interfacial spin polarization.

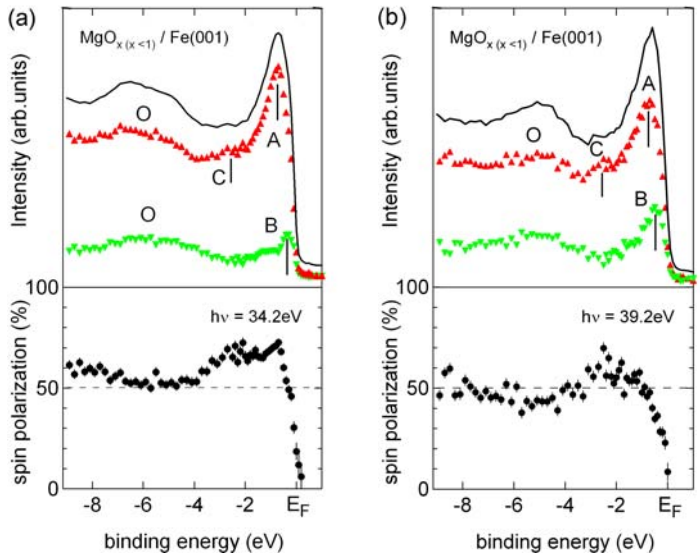

Figure 5.4: Normal-emission spectra for oxygen-deficient MgO_x/Fe(001) interfaces ((a) $h\nu = 34.2$ eV and (b) $h\nu = 39.2$ eV). The spin polarization P is strongly enhanced in the vicinity of the Fermi level. Solid line: spin-integrated data, ▲ denotes majority spin electrons, ▼ denotes minority spin electrons.

For this reason, the following experiments on MgO_x/Fe(001) systems are performed for comparable MgO_x overlayer thicknesses.

Fe(001) in contact with oxygen-deficient MgO_x ($x < 1$)

The preparation and chemical analysis of MgO_x samples with an oxygen content $x < 1$ is discussed in detail in chapter 4.4. Basically, the degree of oxidation is derived from the partial shift of the Mg $2p$ core levels towards the fully oxidized state. A quantification of the oxidation ratio Mg^{2+}/Mg^0 is carried out by means of a standard peak fit procedure. In case of the most under-oxidized MgO_x overlayers, a degree of oxidation of $Mg^{2+}/Mg^0 \approx 0.5\%$ is estimated from the fitted parameters.

The spin-resolved photoemission spectra and spin polarization distributions for oxygen-deficient MgO_x/Fe interfaces are exemplarily displayed in Figure 5.4, recorded at photon energies of $h\nu = 34.2$ eV and 39.2 eV, respectively. In the region of interest close to the Fermi level, we observe a clear difference of the spectral weights of the $\Delta_5^\downarrow$ (**B**) and $\Delta_1^\uparrow$ (**A**) features in comparison to the electronic structure of nearly stoichiometric MgO/Fe interfaces or uncovered Fe. The energetic position of both initial states does not change under this redistribution of the spectral intensity. The spin polarization in an interval of $-2\text{eV} < E_B < E_F$ below the Fermi level thereby exceeds values of 70% and 50%, respectively. Obviously, the coverage of Fe(001) with oxygen-deficient MgO_x leads to an

enhancement of the interfacial spin polarization in comparison to the uncovered Fe surface or the nearly stoichiometric MgO/Fe interface.

The analysis of the oxygen $2p$ states (labeled **O**) below binding energies of -3.5 eV does not reveal any hint for an exchange splitting between majority and minority states. This is a clear indication for a negligible interaction at the oxygen-deficient MgO_x/Fe interface. Obviously, we can deduce a general preference for a Mg-O bonding instead of a Fe-O interaction in the case of the preparation of oxygen deficient MgO. This is due to the gain of electrostatic energy in the highly ionic MgO system ($Mg^{2+}(3s^0)$ $O^{2-}(2p^6)$), which stabilizes the Mg^{2+} and the O^{2-} ions within the crystal field of the structure. In the case of a smaller amount of oxygen atoms compared to the amount of Mg atoms, one can imagine that due to the high reactivity (small electronegativity) of the Mg atoms, a Mg-O bonding will be energetically much more favorable for the oxygen atoms (high electronegativity) compared to a bonding with the less reactive Fe surface.

The presented results provide the first clear evidence for a major change in the electronic structure at MgO/Fe interfaces, if the ferromagnetic layer is covered by an off-stoichiometric MgO layer. In the present case it is reasonable to assume, that the oxygen deficiency of the MgO_x overlayer involves a statistical distribution of vacancy centers at the oxygen sites in the ultrathin MgO layers [102]. One of the most important issues at this point concerns the question, how the existence of these so-called F-centers within the MgO_x layer modifies the electronic structure of the latter and whether an influence on the interfacial electronic structure with the ferromagnetic Fe layer can be expected.

The presence of oxygen defects in oxides is of particular interest in quantum chemistry, because they are common in all oxides and determine their chemical properties [102]. Generally, a neutral oxygen vacancy (F center) attracts two electrons from the Mg atoms, which are trapped by the unbalanced Coulomb potential associated with the vacancy. If one of these electrons is removed, this generates the so-called F^+ center, which represents an unpaired singly charged state. It was shown, that the number of oxygen vacancies in metal oxides simply increases with decreasing oxygen partial pressure during preparation [103], in accordance with our results in chapter 4.4.

The electronic structure of defective oxides is modified in contrast to stoichiometric ones: The oxygen defects give rise to electronic levels *within* the bandgap of the oxide, which are clearly split-off from the continuous bands [104]. Numerous theoretical studies determined the electronic structure of F states induced by MgO oxygen vacancies in bulk materials [104–106]. Their energetic position was determined by means of LDA-based calculations, which are known to systematically underestimate the width of calculated bandgaps (see chapter 2.2.4). Nevertheless, there are various indications that a bound F-center state is typically located in the middle of a calculated bandgap [104, 108].

Very recent interest focused on the properties mediated by defects in MTJs with oxide barriers. Velev *et al.* studied the electronic structure of F centers in a bulk MgO barrier layer in Fe/MgO/Fe MTJs [39]. In accordance with the previous studies, the authors found, that the O vacancy creates two new electronic states, one above and one below the Fermi level as illustrated in Figure 5.5 (a). The first one is an unoccupied p-like state, which appears at the bottom of the MgO conduction band. The second state is occupied by two electrons on the F center site, therefore has an predominantly s-like character and is located about -1 eV below the Fermi level. The s character of this neutral F-center state

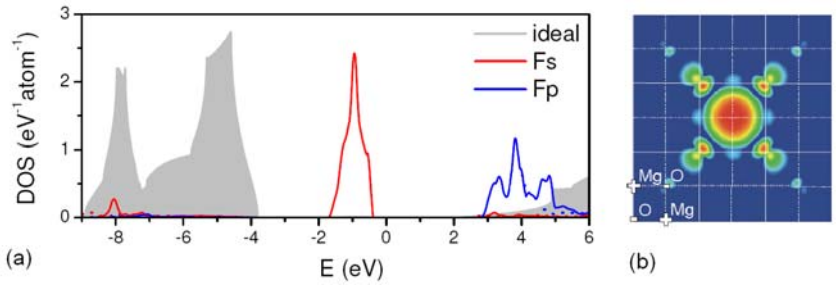

Figure 5.5: (a) Density of states of bulk MgO (shaded area) and F center s and p states for a 32-atom supercell calculation. E=0 is the position of the Fermi level. (b) Charge density of a MgO F center s state. The vacancy is positioned in the middle, the sites of the Mg(+) and O(-) atoms are indicated for one unit cell. From [39].

is evident from the spherically symmetric charge density on the vacancy site, as can be seen in Figure 5.5 (b).

On the experimental side, very recent studies investigated F centers in thin MgO films using electron paramagnetic resonance [110] and scanning tunneling microscopy [111,112]. The experiments identified two defect levels in the band gap of MgO, which coincide with the theoretical predictions. One defect state is centered a few eV above the valence band maximum and another is overlapping with the conduction band minimum. The first level can be identified with a s-like F center ground state, while the second corresponds to the p-like F center exited state (see Figure 3 in [111] and [112], respectively). It seems worthwhile to mention, that the occupied level is unlikely to represent a neutral Mg vacancy, as suggested in Ref. [112], because the formation energy of an so-called V center is larger than that of an F center [113]. The precise position of the levels varies in the experiments, since they depend on the exact environment of the vacancy and the size of the gap. Nevertheless, the s-like, bound F center state of a thin defective MgO film has been found to be positioned about -1 eV below the Fermi level [111], as has been predicted also by theory.

We finally link these considerations to the question, how a bound F center state located at a FM/I interface may interfere with the underlying ferromagnetic electronic structure. The first aspect concerns the localization length scale of the F center. It has been shown theoretically, that the s-like state is spatially localized within the two nearest neighbors of the vacancy site [107]. A slightly shorter extension is predicted in Figure 5.5 (b), which shows that the charge density of the O vacancy interacts at least with the neighboring layers [39]. Both predictions reveal, that the interaction between an F-center, located at the interface and the neighboring Fe surface layer, is actually possible.

The second aspect concerning the interaction between F-centers and the Fe surface at a MgO_x/Fe interface is essentially of geometrical nature. Due to the spatial orientation of the atomic orbitals, the strength of an orbital overlap is strongly geometry dependent. It is well established, that it is energetically favorable for the oxygen atoms to sit on-top of the surface Fe [83]. The interaction along the surface normal usually involves the O $2p_z$ and the Fe $d_{3z^2-r^2} + sp$ orbitals, whose shapes are directly pointing towards each other. In a

further step, we assume, that the oxygen vacancies are positioned at the same lattice sites. As a consequence, in the case of an interaction between a F center with the underlying Fe atom, the s-like F center state will interact with an highly symmetric Fe $3d$ state. It thus seems reasonable to assume, that the oxygen defect state hybridizes with the Fe $3d$ $\Delta_1^{\uparrow}$ level. This orbital overlap may result in an increased charge density of majority electrons, which in turn can enhance the spin polarization at about -1 eV below the Fermi level. This qualitative assumption is in accordance with the above photoemission data.

Oxygen excess at the MgO_x/Fe ($x > 1$) interface

In the following section, we study the electronic structure and interfacial spin polarization of over-oxidized MgO_x/Fe interfaces ($x > 1$). As discussed in chapter 4.4, the oxygen excess is accomplished by offering about 1 L oxygen gas to an under-oxidized MgO_x layer (1 langmuir (L) = 10^{-6} torr/1 sec). Before analyzing the consequences of this preparation procedure for the ferromagnetic $3d$ valence states at the Fermi level, we have to identify the chemical conditions at the MgO_x/Fe interface in a preliminary step. In particular, it is important to clarify, whether the Fe surface is partially oxidized under the present preparation process.

Based on the analysis of the Mg^{2+} $2p$ core level shifts in chapter 4.4, we find, that the subsequent oxygen exposure of about 1 L onto the under-oxidized MgO_x/Fe(001) system yields a complete oxidation of the deposited Mg atoms. Nevertheless, an *over*-oxidation of the MgO layer cannot be deduced from the Mg^{2+} $2p$ core-level shifts. We tentatively assume, that the surplus of supplied oxygen molecules can dissociate and partially incorporate below the MgO_x layer. In this case, it is energetically favorable for the oxygen atoms to be positioned within the bcc hollow sites of the bcc-Fe surface [115]. Due to the very low photoemission cross section of the Fe $3p$ core level, we are not able to extract a possible chemical shift of the latter and thus draw an unequivocal conclusion on the oxidation state of the Fe surface layer.

In order to acquire more information on the chemical environment at the MgO_x/Fe interface, a qualitative analysis of the work function of the samples may serve as a measure for modifications of the electrostatic potential at the surface. In particular, a chemical interaction of oxygen ions with the Fe surface atoms leads to an increase of the surface dipole moment [117]. We can verify these considerations by comparing the work functions of an under-oxidized MgO_x/Fe system to that of an over-oxidized MgO_x/Fe interface. The change of the work function $\Delta\Phi$ may be extracted from a shift of the onset on the low energy side of the photoemission spectrum, which in the present case shifts by a value of more than +0.05 eV. This shift lies below the energetic resolution, but we suppose, that it is an accurate indication of a basic alteration in the surface dipole, which is in accordance with previous photoemission studies on O/Fe systems [117]. Thus, we take the increase of the work function as a first fingerprint, that excess oxygen atoms are partially adsorbed below the top MgO_x layer.

In order to get further insights into the chemical state of the interface, we focus on the properties of the O $2p$ valence states. In the case of an Fe-O interaction, the exchange split $3d$ ferromagnetic electronic structure should be mirrored by the oxygen $2p$ levels [109]. An inspection of the photoemission spectra in Figure 5.6 in the energy regime below $E_B = -3.5$

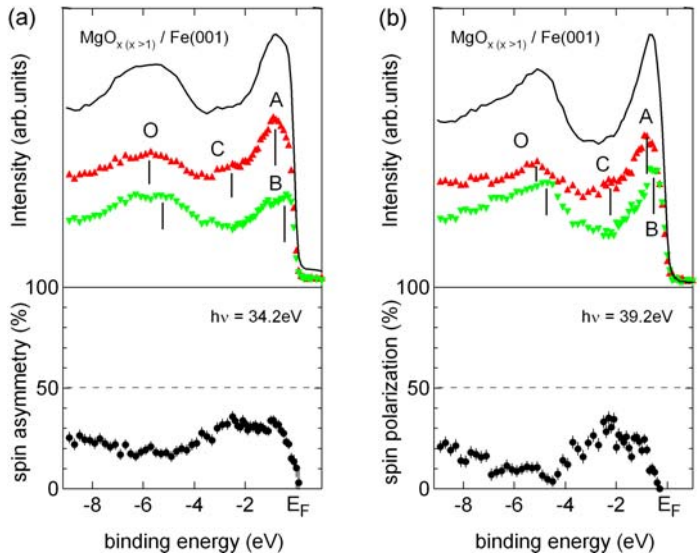

Figure 5.6: Photoemission spectra for MgO_x/Fe(001) interfaces with an oxygen excess ($x > 1$), recorded at photon energies of (a) $h\nu = 34.2$ eV and (b) $h\nu = 39.2$ eV. An electronic interaction between the excess oxygen atoms and the Fe surface can be derived from the exchange splitting of the oxygen $2p$ features (labeled **O**). Solid line: spin-integrated data, ▲ denotes majority spin electrons, ▼ minority spin electrons.

eV reveals, that the oxygen minority and majority features are not centered around a certain binding energy, but do exhibit an induced exchange splitting. The oxygen peaks are thereby ferromagnetically aligned with the Fe surface, i.e. the majority O $2p$ contributions lie deeper on the energy scale by about $\Delta_{xc} = 0.5$ eV in comparison to the minority features. This value is in good agreement with studies by Vescovo *et al.*, who found similar magnitudes for Δ_{xc} for the O/Fe(110) system [109]. The finding confirms, that the Fe surface is in contact with excess oxygen atoms, which are not involved in saturated Mg-O bonds.

At this point it is not yet clear, which type of chemical bonding at the MgO_x/Fe interface actually prevails. For the sake of argument we may distinguish between two different types of interaction of the oxygen atoms in the bcc-hollow sites with the Fe surface: On the one hand, the oxygen atoms can hybridize with the Fe atoms, which may be classified as a covalent interaction driven by orbital overlap, but without a significant charge transfer. On the other hand, the formation of Fe-O bonds in a ionic type of bonding is accompanied by a charge redistribution between both species. As long as the Fe surface is not completely oxidized, i.e. magnetically alive, both types of interaction can principally lead to an induced exchange splitting of the O $2p$ peaks.

We will now turn to the analysis of the Fe $3d$ valence states, which we believe to reflect the actual chemical bonding at the over-oxidized MgO_x/Fe interfaces. We observe

a converse modification of the interfacial electronic structure in comparison to the under-oxidized MgO_x/Fe interface: As displayed in Figure 5.6, the photoemission contributions of the Fe 3*d* $\Delta_1^{\uparrow}$ (**A**) and $\Delta_5^{\downarrow}$ (**B**) features converge. This behavior is apparent in both spectra, being recorded at $h\nu = 34.2$ eV and 39.2 eV, respectively, and leads to a noticeable reduction of the spin polarization at the Fermi level below values of 30%.

Obviously, the chemical bonding at over-oxidized MgO_x/Fe interfaces is characterized by the presence of an exchange splitting, which is linked to a redistribution of spectral weights at the Fermi level. We thus assume, that the chemical bonding at the over-oxidized MgO_x/Fe interface is essentially ionic in nature, because of the significant modifications of the electronic structure at the Fermi level.

In order to understand the detailed mechanism, we draw an analogy to theoretical calculations by Zhang *et al.*, who studied the influence of the Fe-O bond formation on the ferromagnetic 3*d* electronic structure in Fe/FeO_x/MgO/Fe systems. As has been discussed in detail in chapter 2.3.3, the Fe-O bond formation is followed by a reduction of the partial Δ_1 charge density in the interface region (see Figure 2.7). We suggest, that this mechanism can be responsible for the convergence of the Fe 3*d* $\Delta_1^{\uparrow}$ (**A**) and $\Delta_5^{\downarrow}$ (**B**) features, as it can basically reflect a reduction of the $\Delta_1^{\uparrow}$ spectral weight. Consequently, the partial oxidation of the Fe surface layer is thus accompanied by a significant decrease of the interfacial spin polarization.

Interlude: Electronic structure of the O/Fe(001) system

The subsequent exposure of about 1 L of oxygen onto an oxygen-deficient MgO_x film is found to change the latter into an oxygen-excess MgO_x/Fe(001) interface. Moreover, the presence of excess oxygen atoms considerably affects the Fe 3*d* valence band properties and leads to a reduction of the spin polarization at the Fermi level. In the present section, we study the influence of oxygen adsorbates on top of a clean bcc Fe(001) surface, in order to compare the mechanisms of bonding and spin polarization at O/Fe and oxygen excess MgO_x/Fe interfaces. It is reasonable to assume, that the oxygen-exposed Fe surface could reflect the bonding mechanisms at the over-oxidized MgO_x interfaces. We performed spin-resolved photoemission studies of a bcc-Fe(001) film and supplied oxygen doses ranging from 1 L to 11 L (1 langmuir (L) = 10^{-6} torr for 1 sec).

The oxygen exposures are accomplished by admitting high purity gas via a leak valve into the preparation chamber. The actual oxygen dose is determined from the ion-gauge reading. Within the above range of oxygen exposure, previous structural studies revealed the formation of a c(2x2) structure for O coverages below 4 L and a more dense p(1x1) structure for higher oxygen supply [117]. It was consistently reported, that single oxygen atoms incorporate into the four-fold bcc hollow sites of the (001) iron surface [115].

Figure 5.7 shows the spin-resolved photoemission spectra recorded at 34.2 eV for the different stages of oxygen exposure onto a clean Fe(001) surface. The oxygen contribution is found to be centered at about -6 eV below E_F, and gradually increases with continuous oxygen exposure. Since for molecular oxygen (O_2) one would expect to see several molecular orbitals, the single oxygen level at $E_B = -6$ eV is attributed to the 2*p* orbitals of atomic oxygen [117]. The Fe 3*d* valence band emission near E_F does not reveal significant changes. The spin polarization P of the clean Fe film is mainly preserved for an oxygen amount of

about 1 L. In the case of an oxygen dose of 6 L, P increases by more than 15%. According to structural studies, this oxygen dose corresponds to a single-atom coverage of about 1 ML [116]. For the double amount of oxygen atoms (11 L), the spin polarization again decreases to the value of a clean Fe surface.

The oxygen supply of about 1 L on top of a clean Fe(001) surface and on an oxygen-deficient MgO_x film obviously results in a completely different modification of the electronic structure. The adsorption of about 1 L oxygen does not affect the spin polarization of a clean Fe(001) surface, which is complementary to the results presented in section 5.2.2. Here, a reduction of P was observed with a subsequent exposure of about 1 L of oxygen onto the oxygen-deficient MgO_x layers, as the excess oxygen incorporates below the MgO_x film. We believe, that this discrepancy may be related to a different sticking probability of the oxygen atoms at the clean Fe and MgO-covered surface. In the latter case, we can distinguish between two different situations, caused by the presence of unbonded Mg atoms in an under-oxidized MgO_x layer on the one hand and saturated MgO bonds on the other hand. We suggest, that the existence of Mg atoms strongly promotes the dissociation of molecular oxygen due to the large gain of binding energy, if a Mg-O bond is formed. In the case of saturated MgO, we assume, that the strong dipolar character of the ionic bonds enhances the sticking probability for oxygen atoms in comparison to the clean Fe(001) surface. Although these two mechanisms may actually differ in their efficiency, both can lead to an enhanced effective coverage of oxygen atoms on the MgO/Fe surface compared to the clean Fe(001) surface, if the same nominal dosage of oxygen is provided.

In order to analyze the chemical bonding mechanisms at O/Fe and MgO_x/Fe interfaces, it is thus necessary to study both systems under comparable conditions, i.e. with an approximately similar amount of oxygen atoms at the Fe surface. We suggest, that the supply of 6 L oxygen, which refers to roughly 1 ML oxygen coverage, can reflect the partial occupancy of oxygen atoms in the bcc-hollow sites at the oxygen excess MgO_x/Fe interface. By comparing the corresponding photoemission spectra recorded at 34.2 eV in Figures 5.7 and 5.6, the fundamental differences in the chemical bonding mechanisms for the O/Fe and over-oxidized MgO_x/Fe interface become obvious. It can be observed, that the spectral weight of the Fe 3d features is not significantly altered at the O/Fe interface, indicating that practically no charge transfer is involved in the bonding process. However, the presence of an O 2p exchange splitting indicates a magnetic interaction between the oxygen and Fe atoms. Thus, we can exclude a simple physisorption state and conclude on a chemisorption of the oxygen atoms, which involves a hybridization of the electronic states. In contrast, a clear reduction of the Δ_1 spectral weight is found at the oxygen excess MgO_x/Fe interface. This fact supports the assumption of an Fe-O formation in the in-plane direction at the MgO_x/Fe interface, which is accompanied by a charge redistribution in the valence state regime.

The modifications induced by chemisorbed oxygen on the Fe(001) electronic structure have been subject of a number of photoemission studies [116–120]. To our best knowledge, however, no spin-resolved photoemission data on the development of the Fe(001) spin polarization as a function of small doses of adsorbed oxygen have been published so far. From the theoretical point of view, the electronic structure of the (001) surface of bcc Fe covered by one monolayer oxygen has been investigated by Tsymbal *et al.* [121]. It was found, that the spin-polarized density of states of the O/Fe(001) system exhibits a

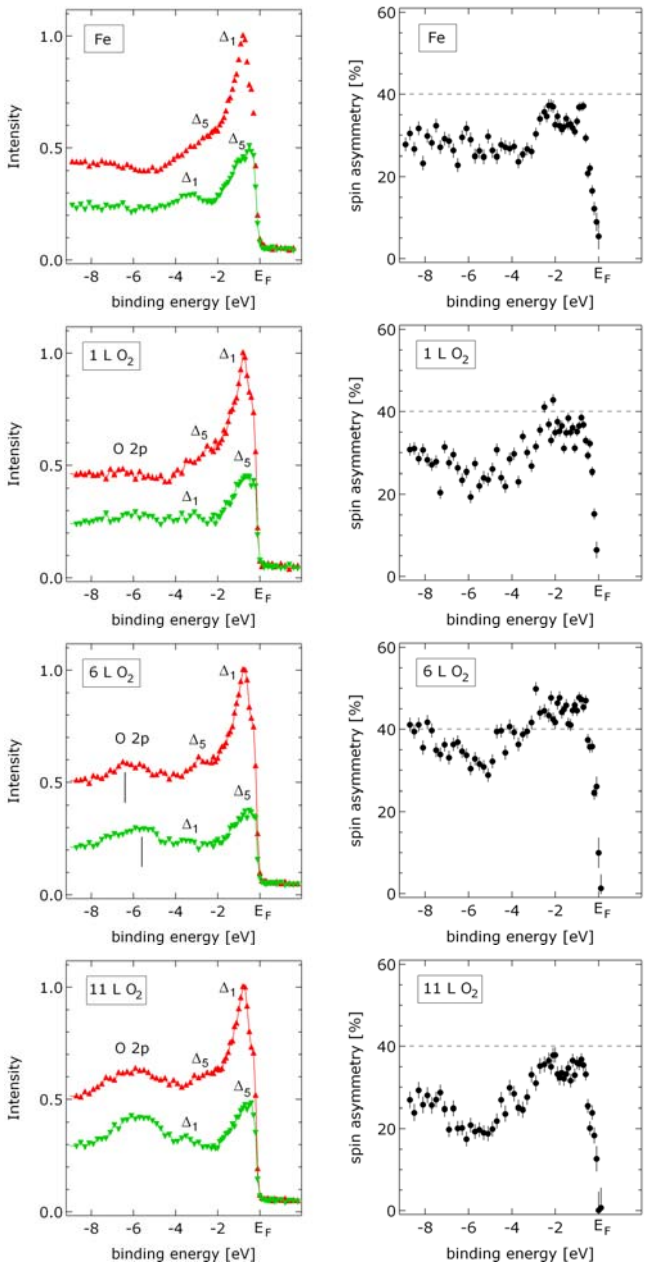

Figure 5.7: Spin-resolved photoemission spectra and spin polarization distributions recorded at $h\nu$ =34.2 eV for an uncovered Fe(001) surface and oxygen-exposed O/Fe(001) samples, offering oxygen doses of 1L, 6L and 11L. ▲ denotes majority spin electrons, ▼ denotes minority spin electrons.

small, induced positive spin polarization in comparison to a free Fe surface [121] (see inset in Figure 5.8). The authors assigned this mechanisms to a hybridization between Fe the $3d$ and O $2p$ orbitals at the Fermi level due to an induced exchange splitting of the antibonding oxygen states. This process can be understood from Figure 5.8, which displays the calculated densities of states (DOS) for bulk Fe, the Fe surface- and O overlayer, according to [121]. The DOS of the surface layer is different from the bulk because of the reduced symmetry. We are not able to resolve this behavior in our photoemission experiments due to strong contributions from the sub-surface layers. The DOS of the oxygen layer has pronounced features located below the Fe $3d$ bands, which are attributed to the bonding O $2p$ orbitals. In addition to the bonding levels, the oxygen DOS displays a broad band of antibonding (AB) states extending up to 3 eV above the Fermi level (see inset in Fig. 5.8). The antibonding character of these electronic states is reflected by the fact, that there is not much charge density shifting from the O atom to the nearest Fe atoms [122]. The exchange splitting between the d orbitals of Fe and the bonding between the d orbitals of Fe and the p orbitals of oxygen induces a splitting of these AB states. They are partially occupied for the majority and almost unoccupied for the minority spins. This leads to an induced positive spin polarization at the Fermi level. We believe, that this mechanism can be held responsible for the enhancement of the spin polarization of the O/Fe(001) system at an oxygen dose of 6 L. Thus, the slightly enhanced positive spin polarization observed in photoemission indicates the hybridization between antibonding O $2p$ and Fe $3d$ valence states.
As a final remark, we note that for higher oxygen exposures the chemisorption stage passes into the formation of iron oxide [117]. This process is accompanied by a constant decrease of the spin polarization, as is already initialized at an oxygen dosage of 11 L (see Figure 5.7).

5.2.3 Interface chemistry and spin polarization

From the experiments presented in the last sections, we observed that the interfacial spin polarization strongly depends on the amount of oxygen atoms and their bonding conditions at the MgO/Fe interfaces. To compile the results, a complete overview of all data sets taken at $h\nu = 34.2$ eV, which illustrate the dependence of the spin polarization on the MgO stoichiometry is given in Figure 5.9. As a measure of the degree of oxidation of the MgO layer, the Mg $2p$ core level peak maximum position of each sample is plotted versus the corresponding maximal spin polarization in an energy interval of -2 eV $< E_B < E_F$.

We thus find a kind of phase diagram, separating Fe/Mg/MgO-type systems characterized by high spin polarizations ($55\% < P < 75\%$) from Fe/MgO-samples with an Fe-like spin polarization ($40\% < P < 50\%$). The degree of oxidation of the MgO layer in these systems can be distinguished by the amount of the Mg $2p$ core level shift. A separate class is formed by the Fe/FeO/MgO-type samples with smaller spin polarization ($P < 35\%$) due to oxidation, which are distinguished by the appearance of an oxygen $2p$ exchange splitting.

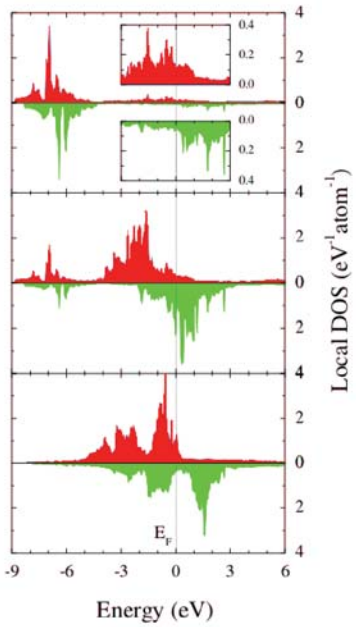

Figure 5.8: Local densities of states of the O/Fe(001) slab as a function of the electron energy. Spin up electrons are denoted by the red and spin-down electrons by the green color. The exchange-split antibonding oxygen states at E_F (see inset) induce a positive spin polarization in the oxygen layer. After Ref. [121].

5.3 The MgO_x/Co(001) interface

In this second part of the chapter, we present first results on MgO_x/Co(001) interfaces. The shape of the valence band structure of ideal bcc-Co is comparable to that of bcc-Fe, but the energetic bands are shifted towards higher binding energies. This is due to the fact, that the (n+1) higher electron occupancy of Co leads to a [Ar $3d^7$] electronic configuration, in comparison to the Fe electronic structure with an [Ar $3d^6$] occupancy. We thus expect particular differences of the valence band electronic structure at Co-based FM/I interfaces.

5.3.1 Electronic structure of bcc-Co(001)

The first set of photoemission experiments aims at characterizing the valence band features of bcc-Co along the (001) direction. In analogy to the analysis of bcc-Fe(001) (see chapter 5.2.1), we choose the photon energy such that the measurements probe electronic states in the direct vicinity to the Fermi level, i.e. in the left half of the Γ-Δ-H line.

The experiments are performed on 6 ML and 12 ML thick Co(001) samples, which are deposited on 27 ML thick Fe seed layers. In chapter 4.3, the preparation procedure is described in more detail. The results of the spin-resolved photoemission experiments

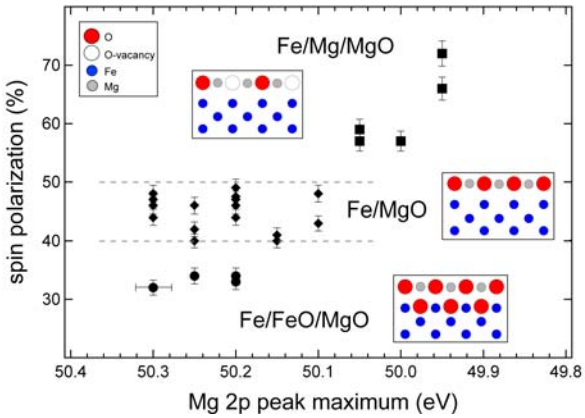

Figure 5.9: Spin polarization P close to the Fermi energy for the systems Fe/Mg/MgO (■), Fe/MgO (⧫) and Fe/FeO/MgO (●). The interface structure is schematically sketched in the insets. For uncovered Fe films, a spin polarization P of about 40% to 50% was obtained. A clear dependence of P on the Mg $2p$ peak maximum is observable.

are exemplarily displayed in Figure 5.11, with the spectra being recorded at a photon energy of $h\nu = 39.2$ eV. The $3d$ valence band electronic structure is dominated by two broad features for majority and minority spin electrons within an energy interval of -3 eV $< E_B < E_F$, which in each case comprise of a double-peak structure. Below a binding energy of $E_B = -3$ eV, a single minority feature of low spectral weight is observed.

The corresponding initial states and spatial symmetries of the partial intensities can be identified from an analysis of a band structure calculation. As has been discussed in chapter 4.3, the experimental structure of the Co films is not exactly bcc, but should contain a slight tetragonal distortion of the lattice resulting in the so-called bct-structure. In this case also the bct band structure is slightly different from the bcc one. Therefore, the influence of the crystalline distortion on the Co electronic structure can not be neglected in the analysis of the present photoemission results. In order to quantify this aspect, the corresponding band structures have been calculated for a bulk bcc Co system, employing the lattice constant of $a = 2.82$ Å, and for a bct-Co lattice, using a distortion ratio of $c/a = 0.92$ (see chapter 4.3) [124, 125]. The results of the calculations are shown in Figure 5.10. Obviously, the consequence of a lattice compression along the c-axis is to change the energetic position of the electronic bands. The modifications reveal a symmetry dependence: Compared to the bcc band structure, the sp-like bands of Δ_1 symmetry in a bct lattice shift towards slightly higher binding energies at the Γ-point. This finding is in accordance with calculations on bct Co by Duò *et al.* [123]. The d-like bands of Δ_5 character, in turn, are bent upwards towards E_F at the Brillouin zone center Γ. The shape of the Δ_1 and Δ_5 bands is not significantly influenced by the bct lattice compression.
Considering the energy region around the Fermi level, an important difference of the valence band structures between bcc-Co and bct-Co becomes evident: Whereas in bcc-Co, the $\Delta_1^{\downarrow}$

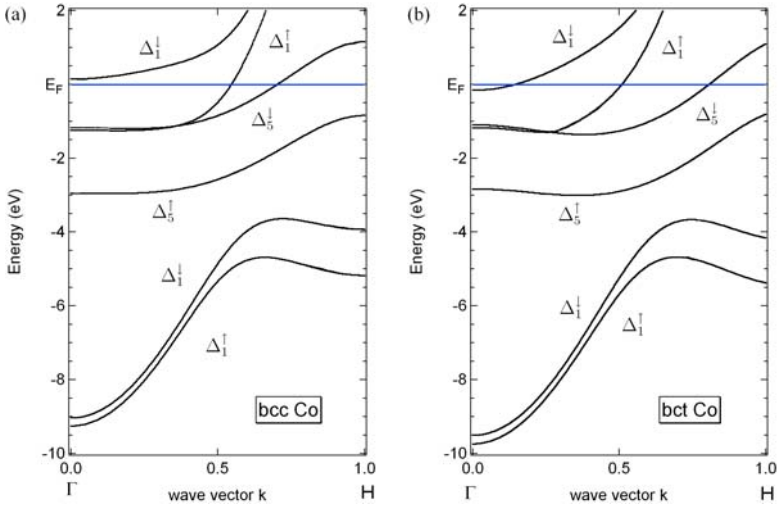

Figure 5.10: Bulk Co(001) band structure calculated by using the SPR-KKR method [23]. (a) Calculation for a bcc lattice and (b) for a bct structure. Under the present experimental geometry, the Δ_1 and Δ_5 initial states can be addressed.

band lies about +0.2 eV above the Fermi energy, it moves downwards on the energy axis and intersects the Γ-point at a binding energy of about $E_B = -0.2$ eV in bct-Co. The structural deviation of the bcc lattice from ideality thus results in a modification of the valence band occupancy at the Fermi level. In view of the (experimental) uncertainty concerning the distortion ratio c/a, the actual energetic shift of the $\Delta_1^\downarrow$ band might be different from the one modeled in the calculation (see Figure 5.10). A quantitative analysis of this aspect requires the knowledge of the distortion in a monolayer-resolved manner and as a function of the Co film thickness. This requires extensive I(V) LEED investigations, which have not yet been performed.

Taking into account the above considerations, we choose the bct Co band structure for a further analysis. In Figure 5.11, we observe a peak of minority character, which lies closest to the Fermi level at a binding energy of $E_B = -0.5 \pm 0.2$ eV (labeled **B**). Obviously, this photoemission contribution cannot be related to the bcc Co valence band features in the left half of the Brillouin zone along Γ-Δ-H. By comparing it to the bct Co band structure, we conclude, that the photoemission from feature **B** can originate from the $\Delta_1^\downarrow$ energy band just below the Fermi level. One has to keep in mind, however, that the tetragonal compression varies with the film thickness and becomes more significant at lower coverages. Indeed, peak **B** reveals a small decrease in spectral weight by increasing the Co coverage from 6 ML to 12 ML. This is attributed to a relaxation of the crystal lattice in c-direction with increasing film thickness, such that the $\Delta_1^\downarrow$ state can shift towards or above the Fermi energy, as it is found for bcc-Co.

By comparing the partial intensities of the 6 ML thick Co film to the bct band structure

in Figure 5.10 (b), further initial states can be identified in the order of decreasing binding energy: The weak minority feature located at $E_B = -4.7 \pm 0.2$ eV (labeled **E**) can be ascribed to a dispersive $\Delta_1^{\downarrow}$ parabola, which starts at the Γ-point. A majority feature labeled **C** is positioned at a binding energy of $E_B = -1.4 \pm 0.2$ eV. It originates from a weakly dispersive $\Delta_1^{\uparrow}$ valence band below the Fermi energy. A $\Delta_5^{\downarrow}$ band lies above the latter at slightly lower binding energies. It gives rise to the peak observed at $E_B = -1.1 \pm 0.2$ eV, which in the following is labeled **D**. The partial intensities **E** and **D** for emission from a 12 ML thick Co film are nearly independent of the film thickness and thus are positioned at similar binding energies. Only the feature labeled **C** exhibits a slight energetic downward shift and is positioned at $E_B = -1.6 \pm 0.2$ eV.

A question arises about the origin of a majority feature located at $E_B = -0.8 \pm 0.2$ eV (labeled **A**). On the basis of the present band structure data, we cannot assign it to a particular interband transition in the bct Brillouin zone. Considering the fact, that the LEED investigations in chapter 4.3 indicate a noticeable roughness of the Co layers, which increases with the Co film thickness, we should take into account the influence of crystalline disorder. The latter can favor the photoemission from regions of the three-dimensional density of states and thus masks direct interband transitions. We thus tentatively attribute the majority feature **A** to emission events from a point of a high density of states, i.e. the high-symmetry point $H_{25}^{\uparrow}$ in the bulk Brillouin zone. We note, that peak **B** cannot be assigned to a surface state, because it also preserved by a top MgO_x layer, as will be shown in the following sections.

The energy distribution of the spin polarization P reveals a characteristic topology within an interval of -2 eV $< E_B < E_F$: It has a negative value of about -10% to -20% in direct vicinity of the Fermi level, but changes its sign at approximately -0.5 eV. Finally, P increases to values of about +20% at a binding energy $E_B = -2$ eV. The arrows in Figure 5.11 indicate a characteristic valley feature, which arises from the strong photoemission contributions of peak **D**.

In summary, the photoemission experiments on Co(001) reveal characteristic $3d$ valence band features of the bct Co bandstructure. In contrast to an ideal bcc structure, we can observe photoemission contributions from a $\Delta_1^{\downarrow}$ state close to the Fermi level. Theoretical calculations emphasize, that changes of the lattice distortion can lead to a shift of the actual $\Delta_1^{\downarrow}$ band position. The spin polarization close to the Fermi level exhibits a negative sign, with a magnitude of about -10% to -20%, but changes its sign at a binding energy of about $E_B = -0.5$ eV.

5.3.2 Electronic structure of MgO_x/Co(001)

In analogy to the studies on MgO_x/Fe systems, the experiments presented in the last section of this chapter investigate modifications of the bct-Co valence bands in contact with a MgO_x overlayer. The thickness of the Co thickness is fixed to 12 ML, in order to study the interfacial electronic states and spin polarization under comparable conditions. Thus, the following data sets on MgO_x/Co always have to be compared to the photoemission spectrum of the uncovered 12 ML Co(001) surface shown in Figure 5.11 (b).

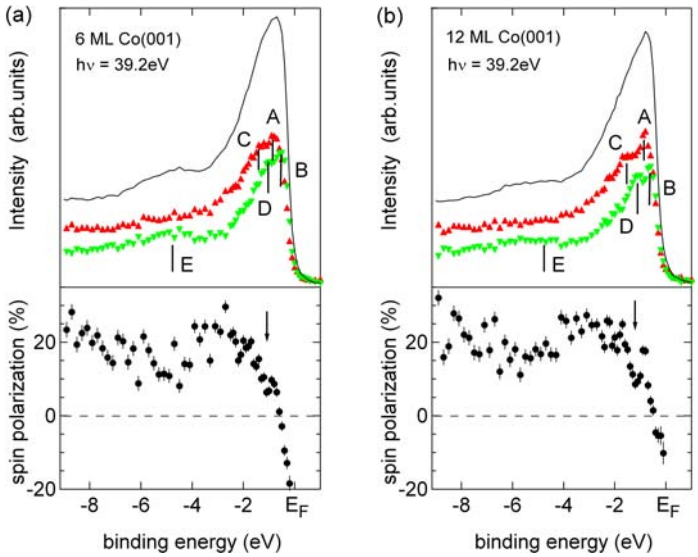

Figure 5.11: Normal-emission spectra from Co(001) for a Co thickness of (a) 6 ML and (b) 12 ML. The excitation was accomplished with p-polarized light ($h\nu = 39.2$ eV) incident at 45° with respect to the surface normal. Solid line: spin-integrated data, ▲ denotes majority spin electrons, ▼ denotes minority spin electrons.

Stoichiometric MgO on Co(001) The spin-resolved photoemission spectra and spin polarization distributions for a nearly stoichiometric MgO overlayer on Co(001) are shown in Figure 5.12. Considering the energy regime in the direct vicinity of the Fermi level, we find the spectral weights of the peaks **A** and **B** to be comparable to that of the uncovered 12 ML Co film. This leads to a comparable rise in the spin polarization spectrum from a negative value of about $P = -15\%$ to $P = +20\%$ in the region between -1 eV and E_F. The analysis of the O $2p$ features indicates, that no noticeable magnetic interaction between the Fe layer and oxygen atoms can be discerned. From this finding, we can exclude a significant chemical interaction between the top MgO layer and the Co surface in the case of a nearly stoichiometric MgO coverage, in analogy to the results on the MgO/Fe(001) system.

Moreover, we can assume, that the vertical lattice spacing c of the crystalline surface is not significantly altered upon coverage with MgO. This is due to the fact, that any shift of the bct lattice would have a direct impact on the energetic position of the $\Delta_1^{\downarrow}$ band. In particular, a structural relaxation would lead to a reduction or even reversal of the negative sign of the spin polarization at E_F by shifting it above the Fermi level.

In comparison to the uncovered 12 ML Co(001) surface, a minor change of the spectral distribution of the features **C** and **D** takes place in the energy regime below $E_B = -1$ eV. The $\Delta_5^{\downarrow}$ state (feature **D**), located at a binding energy of about $E_B = -1.1$ eV, is stronger suppressed in comparison to the other photoemission contributions. This effect is reflected

in the spin polarization spectrum, which indicates a slightly enhanced polarization at $E_B = -1$ eV indicated in Figure 5.12 (b). We note, that an analogue effect of a disproportional reduction of the $\Delta_5^\downarrow$ state has been previously observed for the MgO/Fe(001) system and we refer to chapter 5.2.2 for a further discussion of this issue.

The over-oxidized MgO_x/Co(001) interface Finally, we present the results obtained for an over-oxidized MgO_x/Co(001) interface. The corresponding photoemission spectrum is displayed in Figure 5.12. In analogy to the over-oxidized MgO_x/Fe(001) system, we can clearly identify a Fe-O interaction from the distinctive exchange splitting of the O $2p$ peaks of about $\Delta_{xc} \approx 0.4 \pm 0.2$ eV in the energy regime below $E_B = -3.5$ eV. The enhanced spectral weight of the minority O $2p$ is possibly due to an overlap with the $\Delta_1^\downarrow$ feature **E**, leading to a noticeable hybridization effect. The partial oxidation of the Fe surface is accompanied by a convergence of the majority and minority features close to E_F, which is followed by a reduction of the interfacial spin polarization in the interval -2 eV $< E_B < E_F$. This finding agrees with the results obtained on the corresponding Fe-based interfaces.

Concluding remarks The particular aspects studied at bct Co(001) and MgO_x/Co interfaces reveal both analogies and differences compared to their bcc-Fe counterparts. We thus briefly address some remaining questions, which could not be addressed within the time frame of this thesis.

The results on over-oxidized MgO_x/Co interfaces indicate a comparable behavior to the Fe-based system. It would be interesting to clarify, if the mechanisms of oxygen bonding can be compared that of the oxygen-exposed O/Co(001) surface. We note, that to our best knowledge no spin-resolved photoemission experiments on the valence states of O/bct-Co(001) systems have been performed so far. On the theoretical side, we are aware on a study of the bonding mechanisms at O/Co interfaces for the Co(111) direction [126].

Moreover, the question arises, which influence on the electronic structure can be expected from an under-oxidized MgO overlayer. The presence of the localized bound F-center states below the Fermi level is suggested to lead to a hybridization with the Co $3d$ states in analogy to the Fe system. On the basis of the present data, however, it is not possible to conclude on its particular influence on the interfacial spin polarization in more detail.

In view of the sensitive interplay between the crystalline and electronic structure manifested in bcc and bct Co(001), the question arises, if an induced strain on the bcc Fe(001) lattice would lead to a significantly modified valence band occupancy as well. Indeed, structural studies on bcc-Fe/GaAs(001)-(4x6) reported on a slight tetragonal lattice distortion for thin Fe films ($d \approx 10$ Å) [74]. However, due to the high structural stability of bcc Fe, the distortion is significantly smaller compared to that of the metastable bct Co phase. Moreover, due to the (n-1) lower electron occupancy of the $3d$ states, the $\Delta_1^\downarrow$ state in bcc-Fe(001) is located at higher binding energies above the Fermi level ($E_B = +1.4$ eV at Γ), which excludes a shift of the latter below E_F in the case of a bct lattice distortion. Thus, no significant modification in the Fe $3d$ valence band structure is expected.

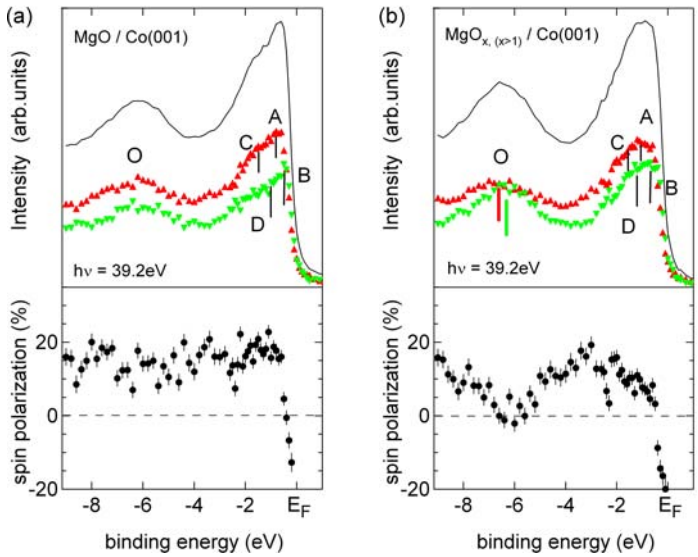

Figure 5.12: (a) Photoemission spectra for nearly stoichiometric MgO on 12 ML Co(001) and (b) for an over-oxidized MgO_x/12 ML Co(001) interface. Solid line: spin-integrated data, ▲ denotes majority spin electrons, ▼ denotes minority spin electrons.

5.4 Summary

In this chapter, the electronic structure of MgO_x/Fe(001) and MgO_x/Co(001) interfaces has been investigated by means of spin- and angle-resolved photoemission spectroscopy, recorded at photon energies between $h\nu = 34.2$ eV and 39.2 eV. By combining results from the Mg $2p$ core-levels with the analysis of the ferromagnetic $3d$ valence- and the oxygen $2p$ states, consistent pictures of the particular chemical environment could be proposed for the different FM/I systems. The distinct interface bonding conditions are sensitively reflected by the interfacial spin polarization.

As a prerequisite for the subsequent investigations, in a first step the Fe(001) electronic structure was investigated. The uncovered Fe(001) samples revealed a fully bulk-like electronic structure. We identified the possible initial states from the calculated band structure of a bulk Fe(001) system. The energetic position of the observed photoemission features as well as the measured spin polarization P are in good agreement with previous photoemission studies on the Fe(001) system.
The results of the electronic structure of the Fe(001) system served as a reference for the following experiments, in which possible modifications of the interface due to a MgO_x coverage were investigated. We focused on three different cases of a MgO_x/Fe(001) interface: the nearly stoichiometric, the oxygen-deficient ($x < 1$) and the oxygen excess interface ($x > 1$). Special attention was paid to MgO_x stoichiometries deviating from the nearly

stoichiometric case.
The nearly stoichiometric MgO/Fe(001) interface was found to exhibit only a very weak interaction between ferromagnet and insulator. No significant changes in the electronic structure close to the Fermi energy were detected, which goes along with a conservation of the interfacial spin polarization. This finding is in good agreement with theoretical predictions of a weak interaction between ferromagnet and insulator in case of a well-balanced oxide stoichiometry.
If the ferromagnetic sample was covered with under-oxidized MgO_x, the modification of the Fe $3d$ electronic structure was accompanied by an enhancement of the spin polarization close to the Fermi level. This result represents an important finding, since it demonstrates for the first time, that an MgO coverage deviating from the ideal stoichiometry has a strong impact on the interfacial electronic structure. This unexpected increase of P is qualitatively explained by taking into account the electronic structure of the defective oxide layer and we proposed a hybridization between s-like, bound F center states with the Fe $3d$ $\Delta_1^{\uparrow}$ valence band.
In the case of a MgO_x/Fe interface with an excess of oxygen atoms ($x > 1$), a detrimental influence on the electronic structure was observed. In contrast to the previous cases, a reduction of the spin polarization was detected in the vicinity of E_F. We attribute this behavior to a redistribution of Δ_1 states, which are supposed to form a sub-stoichiometric FeO intralayer at the interface. The experimental confirmation for this Fe-O interaction was deduced from the induced exchange splitting of the O $2p$ levels. This result is in qualitative agreement with theoretical calculations [15], which predict a decrease of the partial Δ_1 majority density of states at the Fe/FeO/MgO interface.
The adsorption of oxygen atoms onto a Fe(001) surface was investigated, in an effort to elucidate possible bonding mechanisms involved at an over-oxidized interface. Surprisingly, a slight enhancement of the spin polarization P was found, if the Fe(001) surface was covered by roughly one monolayer of oxygen. By increasing the oxygen dose, the effect is reversed. We were able to relate this finding to an induced exchange splitting of the antibonding oxygen $2p$ levels. In contrast to the over-oxidized interface, the chemisorption of 1 L of oxygen atoms is not accompanied by a reduction of the spin polarization, which clearly points out the different bonding mechanisms at the MgO_x/Fe interface.
We finally propose a phase diagram, which summarizes the dependence of the spin polarization on the amount of oxygen atoms at the MgO_x/Fe interface.
In the second part of the chapter, the investigations extended towards the MgO_x/Co interface. In a first step, the valence band structure of Co(001) was investigated at a photon energy of $h\nu = 39.2$ eV. The results were discussed with regard to a tetragonal distortion of the bcc lattice, which gives rise to a shift of individual band positions. A theoretical modeling indicates, that the $\Delta_1^{\downarrow}$ band moves across the Fermi level at the Γ-point under a bct lattice compression. We could identify photoemission contributions of the $\Delta_1^{\downarrow}$ states in the close vicinity of the Fermi level, suggesting the presence of a strain-induced bct Co structure.
The photoemission experiments on MgO_x/Co(001) interfaces revealed a nearly conserved interfacial electronic structure for a stoichiometric MgO coverage and a reduction of the spin polarization at the over-oxidized interface. These observations perfectly agree with the results on MgO_x/Fe interfaces.

Chapter 6

Conclusions and Outlook

The thesis at hand represents the first detailed study on the electronic structure of MgO_x/Fe and MgO_x/Co ferromagnet-insulator interfaces – material combinations that are widely used now in magnetic tunnel junctions. The systems have been investigated by means of spin- and angle-resolved photoemission spectroscopy, addressing the Mg $2p$ core levels as well as the ferromagnetic $3d$ and oxygen $2p$ valence states in order to elucidate the correlation between electronic structure and chemical bonding formation. The results reveal, that the ferromagnetic $3d$ states at the interface and, consequently, the interfacial spin polarization are sensitively controlled by the interface chemistry. In particular, we could identify three distinctive scenarios: the nearly stoichiometric, the oxygen-deficient and the over-oxidized MgO_x/ferromagnet interface. Each case is defined by innate characteristics of the electronic structure at the Fermi level: While the spin polarization is conserved for nearly stoichiometric MgO overlayers, a beneficial and detrimental impact on the latter is manifested for oxygen-deficient and over-oxidized MgO_x/Fe interfaces. An analogue mechanism was observed at stoichiometric and oxygen-excess MgO_x/Co interfaces.

These findings provide an important new aspect of the electronic structure at ferromagnet-insulator interfaces and we suggest, that they may also have direct consequences for the spin-polarized electron transport in single-crystalline, MgO-based magnetic tunnel junctions (MTJs). The results underline, that details of experimentally realized ferromagnet-insulator interfaces can be crucial, and the assumption of an ideal MgO composition may be oversimplified in theoretical descriptions. By focussing particularly on the influence of a varying MgO stoichiometry, the results obtained in this thesis provide important insight into electronic structures of *real* ferromagnet-insulator interfaces in magnetic tunnel junctions.

The impact of this aspect becomes evident by considering the various experimental approaches to prepare MTJ structures with MgO barriers, which can easily lead to an oxygen excess or deficiency at the ferromagnet-MgO interface. A common method is to evaporate MgO from polycrystalline material. It is known, that in this case an FeO layer can form at the interface between Fe and MgO, leading immediately to a deviation from the ideal interface structure [16]. Therefore, the trick to prevent the oxidation of the ferromagnetic electrode by covering it with a thin layer of pure Mg before the evaporation of MgO in an O_2 atmosphere is frequently used [17]. However, our results show that this approach fails if an excess of oxygen is provided.

Our experiments reveal, that any deviation from a stoichiometric MgO composition can have an enormous impact on the electronic ground state properties of the ferromagnetic electrode. If too much oxygen is provided during the post-oxidation of a magnesium layer, we find that the presence of unoxidized Mg atoms promotes the dissociation of molecular oxygen. Thus, the presence of Mg can even enhance the probability for an FeO formation at the partially covered ferromagnetic interface, although it was initially intended to prevent it. Our studies reveal, that this mechanism is followed by a reduction of the interfacial spin polarization. By considering the opposite situation, in which not enough oxygen atoms are provided during a post-oxidation of Mg to form stoichiometric MgO, the system ends up with an oxygen deficient interface and MgO barrier. In this situation, we could manifest a significant enhancement of the spin polarization at the interface.

By taking the reversed view, our results demonstrate, that it is actually feasible to carefully control the magnitude of the ground state spin polarization by 'chemically engineering' the bonding conditions at the ferromagnet-insulator interface. It is apparent, that this aspect is of high relevance for an extended understanding of the mechanisms, which can determine the magnitude of the tunneling spin polarization beyond simple ferromagnet-insulator-ferromagnet model systems.

In a more detailed picture, the electronic structure at ferromagnet-insulator interfaces in a tunnel junction determines the properties of the spin-polarized tunneling current, which is carried by the spatially least decaying wavefunctions. In the special case of Fe/MgO/Fe(001) and Co/MgO/Co(001), the tunneling probability is largest for electronic states with a Δ_1 symmetry along the (001) direction. Thus, the partial ground state polarization of the Δ_1 symmetry states at the Fermi level is decisive for the tunneling spin polarization. As an important result of our experiments, the reduction of the interfacial spin polarization at the over-oxidized MgO-ferromagnet interface can be assigned to a reduction of the Δ_1 majority spectral weight, which is in perfect agreement with theoretical studies. The importance of the Δ_1 ground state properties is evident by considering the insertion of a FeO (CoO) interlayer into a magnetic tunnel junction: Due to the partial reduction of the Δ_1 density of states, the tunneling magnetoresistance (TMR) signal is significantly reduced. More generally, the chemical bonding at the interface has direct consequences for the electronic ground states, which in turn influence the properties of the spin-polarized tunneling current.

As a central outcome of our experiments, the occurrence of an enhanced spin polarization at under-oxidized MgO/Fe interfaces is related to an enhanced Δ_1 majority occupancy, caused by the presence of oxygen vacancy states. By taking into account this experimental finding and the recent theoretical predictions discussed in chapter 2.3.3, the oxygen vacancies apparently have both beneficial and detrimental influence on the TMR, depending on where they are placed. On the one hand, being located at the Fe/MgO interface, they are able to enhance the Fe interfacial spin polarization of the Δ_1 states, thereby enhancing the TMR. On the other hand, oxygen vacancies in the bulk of the MgO barrier may lead to a decrease of the Δ_1 majority conductance, thus decreasing the TMR. On the basis of this picture, one may suggest, that the high TMR in understoichiometric Fe(001)/MgO is affected by a delicate balance of position and density of oxygen vacancies.

These findings may support recent experiments by Yuasa *et al.* [8] on single crystalline Fe(001)/MgO/Fe magnetic tunnel junctions, which exhibited remarkably high TMR values:

It was reported, that while MgO(001) was grown by electron-beam evaporation from a stoichiometric MgO source material, some of the evaporated MgO released O atoms, that formed O_2 molecules. The authors conclude, that the deposited MgO contained some oxygen vacancy defects. The experimental results give substance to the speculation, that the magnitude of the tunneling spin polarization might have significantly increased by introducing a MgO barrier of under-oxidized stoichiometry into Fe-based TMR devices. According to the picture proposed in this discussion, the enhancement should be most effective, if the oxygen vacancy defects are mostly located at the Fe/MgO interface.

The spin-split electronic structure in bcc Co-based MTJs is known to yield an improved spin-filtering effect, leading to even higher TMR ratios compared to Fe-based systems. Our experiments on the electronic structure of Co(001) emphasize the necessity to stabilize a bcc lattice in Co-based MTJs, since the presence of a strain-induced bct phase gives rise to a valence band occupancy of Δ_1 minority states, thus reducing the TMR. It is therefore of major importance to provide a bcc structure close to ideality in order to optimize the tunneling efficiency.

The results presented in this thesis leave various questions open, which ask for further investigation. The experimental realization of MTJs with an under-oxidized MgO interface and a stoichiometric bulk MgO barrier opens up a new and highly topical pathway for studying a new kind of MTJs. It should be accompanied by theoretical studies of under-oxidized MgO/Fe interfaces to enlarge the understanding of the fundamental mechanisms, which originate from interfacial oxygen vacancy states and may act beneficial on the TMR. Moreover, it would be interesting to study the correlation between electronic structure and chemical bonding in magnetic tunnel junctions with other electrode materials. For example, the electronic structure of ferromagnetic manganese perovskite materials like $LaSrMnO_3$ with its half-metallic behavior is suggested to provide an enhanced ground state spin polarization. It is interesting to clarify, which modifications of the electronic ground state properties are induced by the chemical bonding at such interfaces and which consequences can be expected for the spin-dependent tunneling process. A further important aspect to be investigated concerns the morphology of ultrathin Mg and under-oxidized MgO layers grown on ferromagnetic bcc (001) surfaces. It is particularly important to reveal the actual growth mechanisms in order to estimate the consequences of a post-oxidation process on the under-oxidized MgO barrier. In addition, this aspect may allow deeper insight into the electronic properties of transition metal-Mg interfaces from a fundamental point of view. A wide field of study is opened up by exploring the electronic and structural properties of bcc and bct MgO/Co(001) systems. Several questions come to the fore: Is it possible to optimize the stability of the bcc phase? Does the Co(001) surface reveal an analogue behavior concerning an oxygen exposure compared to Fe(001)? Can we expect an influence on the TMR for under-oxidized MgO overlayers as well?
This thesis has added some tiles to the mosaic of our understanding of the material-dependence in TMR systems. Answering some of the questions raised above will lead to a refined comprehension of the relationship of the tunneling magnetoresistance and spin polarization to the ferromagnetic and tunnel barrier electronic structures in the near future.

Bibliography

[1] P. Grünberg, R. Schreiber, Y. Pang, M. B. Brodsky and H. Sowers, *Layered Magnetic Structures: Evidence for Antiferromagnetic Coupling of Fe Layers across Cr Interlayers*, Phys. Rev. Lett. **57**, 2442 (1986)

[2] G. Binash, P. Grünberg, F. Saurenbach, and W. Zinn, *Enhanced magnetoresistance in layered magnetic structures with antiferromagnetic interlayer exchange*, Phys. Rev. B **39**, 4828 (1989)

[3] M. Baibich, J. Broto, A. Fert, F. v. Dau, F. Petroff, P. Etienne, G. Greuzet, A. Freidrich, and J. Chazelas, *Giant magnetoresistance of (001)Fe/(001)Cr magnetic superlattices*, Phys. Rev. Lett. **61**, 2471 (1988)

[4] S. A. Wolf, D. D. Awschalom, R. A. Buhrmann, J. M. Daughton, S. v. Molnar, M. L. Roukes, A. Y. Chtchelkanova, and D. M. Treger, *Spintronics: A spin-based electronic vision for the future*, Science **294**, 1488 (2001)

[5] J. S. Moodera, L. R. Kinder, T. M. Wong and R. Meservey, *Spin-tunneling in ferromagnetic junctions*, Phys. Rev. Lett. **74**, 3273 (1995)

[6] T. Miyazaki and N. Tezuka, *Giant magnetic tunneling effect in Fe/Al_2O_3/Fe junctions*, J. Magn. Magn. Mat. **139**, L231 (1995)

[7] S. S. P. Parkin, C. Kaiser, A. Panchula, P. M. Rice, B. Hughes, and M. Samant, *Giant tunneling magnetoresistance at room temperature with MgO(100) tunnel barriers*, Nature Materials **3**, 862 (2004)

[8] S. Yuasa, T. Nagahama, A. Fukushima, Y. Suzuki, and K. Ando, *Giant room-temperature magnetoresistance in single-crystal Fe/MgO/Fe magnetic tunnel junctions*, Nature Materials **3**, 868 (2004)

[9] J. Mathon and A. Umerski, *Theory of tunneling magnetoresistance of an epitaxial Fe/MgO/Fe(001) junction*, Phys. Rev. B **63**, R220403 (2001)

[10] W. H. Butler, X. G. Zhang, T. C. Schulthess, and J. M. MacLaren, *Spin-dependent tunneling conductance of Fe/MgO/Fe sandwiches*, Phys. Rev. B **63**, 054416 (2001)

[11] M. Jullière, *Tunneling between ferromagnetic films*, Phys. Lett. A **54**, 225 (1975)

[12] J. M. MacLaren, X.-G. Zhang, W. H. Butler and X.-D. Wang, *Layer KKR approach to Bloch-wave transmission and reflection: Application to spin-dependent tunneling*, Phys. Rev. B **59**, 5470 (1999)

[13] P. Mavropoulos, N. Papanikolaou, and P. H. Dederichs, *Complex bandstructure and tunneling through ferromagnet/insulator/ferromagnet junctions*, Phys. Rev. Lett. **85**, 1088 (2000)

[14] J. M. de Teresa, A. Barthélémy, A. Fert, J. P. Contour, F. Montaigne, and P. Seneor, *Role of metal-oxide interface in determining the spin polarization of magnetic tunnel junctions*, Science **286**, 507 (1999)

[15] X. G. Zhang, and W. H. Butler, *Effects of the iron-oxide layer in Fe-FeO-MgO-Fe tunneling junctions*, Phys. Rev. B **68**, 092402 (2003)

[16] H. L. Meyerheim, R. Popescu, J. Kirschner, N. Jedrecy, M. Sauvage-Simkin, B. Heinrich and R. Pinchaux, *Geometrical and compositional structure at metal-oxide interfaces: MgO on Fe(001)*, Phys. Rev. Lett. **87**, 076102 (2001)

[17] S. S. P. Parkin, *Spin-polarized current in spin valves and magnetic tunnel junctions*, MRS Bulletin **31**, 389 (2006)

[18] S. Blundell, *Magnetism in Condensed Matter*, Oxford University Press, Oxford (2001)

[19] H. Ibach and H. Lüth, *Solid State Physics*, Springer, Berlin (1995)

[20] P. Mohn, *Magnetism in the Solid State*, Springer, Berlin (2003)

[21] R. Zeller, 36. Spring School 2005 *Magnetism goes nano*, Lecture Notes, Jülich (2005)

[22] C. M. Schneider and J. Kirschner, *Magnetism at Surfaces and in Ultrathin Films* in Handbook of Surface Science, Elsevier, Amsterdam (2000)

[23] H. Ebert *et al.*, *The Munich SPR-KKR package, Version 2.1*, http://olymp.cup.uni-muenchen.de/ak/ebert/SPRKKR

[24] I. I. Mazin, *How to define and calculate the degree of spin polarization in ferromagnets*, Phys. Rev. Lett **83**, 1427 (1999)

[25] W. A. Harrison, *Electronic Structure and the Properties of Solids*, Dover, New York (1989)

[26] C. N. Berglund and W. E. Spicer, *Photoemission study of copper and silver: Experiment and Theory*, Phys. Rev. B **136**, A1030, A1044 (1964)

[27] P. D. Johnson, *Spin-polarized Photoemission*, Rep. Prog. Phys. **60**, 1217 (1997)

[28] D. R. Penn, S. P. Apell, and S. M. Girvin, *Theory of spin-polarized secondary electrons in transition metals*, Phys. Rev. Lett. **55**, 518 (1985)

[29] J. Kirschner, *Polarized Electrons at Surfaces*, Springer, Berlin (1985)

[30] J. Hermanson, *Final state symmetries and polarization effects in angle-resolved photoemission spectroscopy*, Solid State Comm. **22**, 9 (1977)

[31] W. Eberhardt and F. J. Himpsel, *Dipole selection rules for optical transitions in the fcc and bcc lattices*, Phys. Rev. B **21**, 5572 (1980)

[32] S. Hüfner, *Photoelectron Spectroscopy*, Springer, Berlin (1995)

[33] P. Hohenberg and W. Kohn, *Inhomogeneous electron gas*, Phys. Rev. **136**, 864 (1964)

[34] M. Levy, *Universal variational functionals of electron densities, first order density matrices, and natural spin-orbits and solutions of the v-representability problem.*, Proc. Natl. Acad. Sci. USA **76**, 6062 (1979)

[35] W. Kohn and L. J. Sham, *Self-consistent equations including exchange and correlation effects*, Phys. Rev. **140**, 1133 (1965)

[36] R. Meservey and P. M. Tedrow, *Spin-polarized electron tunneling*, Physics Reports **238**, 173 (1994)

[37] J. S. Moodera, J. Nassar and G. Mathon, *Spin-tunneling in ferromagnetic junctions*, Ann. Rev. Mater. Sci. **29**, 381 (1999)

[38] X.-G. Zhang and W. H. Butler, *Band structure, evanescent states, and transport in spin tunnel junctions*, J. Phys.: Condens. Matter **15**, R1603 (2003)

[39] J. P. Velev, M. Ye. Zhuravlev, K. D. Belashenko, S. S. Jaswal, E. Y. Tsymbal, T. Katayama, and S. Yuasa, *Defect-mediated properties of magnetic tunnel junctions*, Appl. Phys. Lett. **90**, 072502 (2007)

[40] J. Hayakawa et al., Talk 18 A-6, ICMFS 2006, Sendai

[41] H. Lüth, *Surfaces and Interfaces of Solid Materials*, Springer, Berlin (1996)

[42] F. J. Himpsel, J. E. Ortega, G. J. Mankey, and R. F. Willis, *Magnetic nanostructures*, Adv. Phys. **47**, 511 (1998)

[43] E. Bauer, Z. Kristallogr. **110**, 372 (1958)

[44] J. Kirschner and R. Feder, *Spin polarization in double diffraction of low-energy electrons from W(001): Experiment and theory*, Phys. Rev. Lett. **42**, 1008 (1979)

[45] J. Kirschner, R. Feder and J. F. Wendelken, *Electron spin polarization in energy- and angle-resolved photoemission from W(001): Experiment and theory*, Phys. Rev. Lett. **47**, 614 (1981)

[46] R. Feder, *Spin-polarized low-energy electron diffraction*, J. Phys. C: Sol. State Phys. **14**, 2049 (1981)

[47] C. Carbone, 30. Spring School 1999 *Magnetische Schichtsysteme*, Lecture Notes, Jülich (1999)

[48] J. Kessler, *Polarized Electrons*, Springer, Berlin (1976)

[49] G. Ertl and J. Küppers, *Low energy electrons and surface chemistry*, VCH Weinheim (1985)

[50] M. P. Seah and W. A. Dench, *Quantitative electron spectroscopy of surfaces: A standard database for electron inelastic mean free pathes in solids*, Surf. Interface Anal. **1**, 2 (1979)

[51] D. Briggs and M. P. Seah, *Practical Surface Analysis, Vol.1: Auger and x-ray photoelectron spectroscopy*, Wiley, Chichester (1990)

[52] S. Tanuma, C. J. Powell, and D. R. Penn, *Calculation of electron inelastic mean free path for 31 materials*, Surf. Interface Anal. **11**, 577 (1988)

[53] R. Germar, W. Dürr, J. W. Krewer, D. Pescia, and W. Gudat, *Layer-by-layer growth of metal overlayers*, App. Phys. A **47**, 393 (1988)

[54] C. M. Schneider, *Electronic structure and magnetic properties of ultrathin epitaxial films: fcc Cobalt on Cu(100)*, PhD Thesis, Berlin (1990)

[55] W. F. Egelhoff, Jr., *Core-level binding-energy shifts at surfaces and in solids*, Surf. Sci. Reports **6**, 253 (1987)

[56] *Handbook of Auger electron spectroscopy*, Physical Electronics Inc., Minnesota (1995)

[57] D. A. Shirley, *High-resolution X-ray photoemission spectrum of the valence bands of gold*, Phys. Rev. B **5**, 4709 (1972)

[58] J.-J. Yeh and I. Lindau, *Atomic Subshell Photoionization Cross Sections and Asmmetry Parameters: $1 < Z < 103$*, At. Data Nucl. Data Tables **32**, 1 (1985)

[59] J.-J. Yeh, *Atomic Calculations of Photoionization Cross Sections and Asymmetry Parameters*, Gordon and Breach, Langhorne, PA (1993)

[60] XPSPeak Version 4.1, XPS Fitting Program, freely available software

[61] CasaXPS Handbook, *Peak fitting in XPS*, Casa Software Ltd. www.casaxps.com (2006)

[62] Q.-K. Xue, T. Hashizume, and T. Sakurai, *Scanning tunneling microscopy studies of GaAs(001) surfaces*, Appl. Surf. Sci. **141**, 244 (1999)

[63] T. L. Monchesky, B. Heinrich, R. Urban, K. Myrtle, M. Klaua and J. Kirschner, *Magnetoresistance and magnetic properties of Fe/Cu/Fe/GaAs(100)*, Phys. Rev. B **60**, 10242 (1999)

[64] P. Kocán, A. Ohtake, and N. Koguchi, *Structural features of Ga-rich GaAs(001) surfaces: Scanning tunneling microscopy study*, Phys. Rev. B **70**, 201303 (2004)

[65] G. A. Prinz and J. J. Krebs, *Molecular beam epitaxial growth of single-crystal Fe films on GaAs*, Appl. Phys. Lett. **39**, 397 (1981)

[66] J. J. Krebs, B. T. Jonker and G. A. Prinz, *Properties of Fe single-crystal films grown on (100) GaAs by molecular-beam epitaxy*, J. Appl. Phys. **61**, 2596 (1986)

[67] E. Kneedler, P. M. Thibado, B. T. Jonker, B. R. Bennett, B. V. Shanabrook, R. J. Wagner, and L. J. Whitman, *Epitaxial growth, structure, and composition of Fe films on GaAs(001)-2x4*, J. Vac. Sci. Technol. B **14**, 3193 (1997)

[68] M. Zölfl, M. Brockmann, M. Köhler, S. Kreuzer, T. Schweinböck, S. Miethaner, F. Bensch, and G. Bayreuther, *Magnetic films epitaxially grown on semiconductors*, J. Magn. Magn. Mater. **175**, 16 (1997)

[69] M. Brockmann, M. Zölfl, S. Miethaner, and G. Bayreuther, *In-plane volume and interface magnetic anisotropies in epitaxial Fe films on GaAs(001)*, J. Magn. Magn. Mater. **198**, 384 (1999)

[70] M. Doi, B. Roldan Cuenya, W. Keune, T. Schmitte, A. Nefedov, H. Zabel, D. Spodding, R. Meckenstock, and J. Pelzl, *Magnetic and structural properties of epitaxial thin Fe films on GaAs(001) and interfaces*, J. Magn. Magn. Mater. **198**, 384 (1999)

[71] M. Gester, C. Daboo, S. J. Gray, and J. A. C. Bland, *Formation of pyramid-like structures in the growth of epitaxial Fe/GaAs(001) structures*, J. Magn. Magn. Mater. **165**, 242 (1997)

[72] C. Carbone, B. T. Jonker, K.-H. Walker, G. A. Prinz, and E. Kisker, *The epitaxial growth of Fe on GaAs(110): Development of the electronic structure and interface formation*, Sol. State Comm. **61**, 297 (1987)

[73] R. Moosbüher, F. Bensch, M. Dumm, and G. Bayreuther, *Epitaxial Fe films on GaAs(001): Does the substrate surface reconstruction affect the uniaxial magnetic anisotropy?*, J. Appl. Phys. **91**, 8757 (2002)

[74] R. A. Gordon, E. D. Crozier, D.-T. Jiang, P. S. Budnik, T. L. Monchesky, and B. Heinrich, *In situ EXAFS study of Fe epitaxially grown by MBE on GaAs(001)-4x6*, Surf. Sci. **581**, 47 (2005)

[75] P. M. Thibado, E. Kneedler, B. T. Jonker, B. R. Bennett, B. V. Shanabrook, and L. J. Whitman, *Nucleation and growth of Fe on GaAs(001)-(2x4) studied by scanning tunneling microscopy*, Phys. Rev. B **53**, R10481 (1996)

[76] S. A. Chambers, F. Xu, H. W. Chen, I. M. Vitomirov, S. B. Anderson, and J. H. Weaver, *Simultaneous epitaxy and substrate out-diffusion at a metal-semiconductor interface: Fe/GaAs(001)-c(8x2)*, Phys. Rev. B **34**, 6605 (1986)

[77] B. Heinrich and J. A. C. Bland, *Ultrathin Magnetic Structures II*, Springer, Berlin (1994)

[78] G. Prinz, *Stabilization of bcc Co via Epitaxial Growth on GaAs*, Phys. Rev. B **54**, 1051 (1985)

[79] Y. Park, E. E. Fullerton, and S. D. Bader, *Epitaxial growth of ultrathin MgO films on Fe(001) seed layers*, J. Vac. Sci. Technol. A **13**(2), 301 (1994)

[80] J. L. Vassent, M. Dynna, A. Marty, B. Gilles, and G. Patrat, *A study of growth and the relaxation of elastic strain in MgO on Fe(001)*, J. Appl. Phys. **80**, 5727 (1996)

[81] J. L. Vassent, A. Marty, B. Gilles, and C. Chantillion, *Thermodynamic analysis of molecular beam epitaxy of MgO(s): II. Epitaxial growth of MgO layers on Fe(001) substrates*, J. Cryst. Growth. **219**, 444 (2000)

[82] B. D. Yu and J.-S. Kim, *Ab initio study of ultrathin MgO films on Fe(001): Influence of interfacial structures*, Phys. Rev. B **73**, 125408 (2006)

[83] T. Urano and T. Kanaji, Thin Solid Films **32**, 217 (1976)

[84] M. Klaua, D. Ullmann, J. Barthel, W. Wulfhekel, J. Kirschner, R. Urban, T. L. Monchesky, A. Enders, J. F. Cochran, and B. Heinrich, *Growth, structure, electronic, and magnetic properties of MgO/Fe(001) bilayers and Fe/MgO/Fe(001) trilayers*, Phys. Rev. B **64**, 134411 (2001)

[85] C. D. Wagner, W. M. Riggs, L. E. Davis, J. F. Moulder, G. E. Muilenberg, *Handbook of X-ray Photoelectron Spectroscopy*, Physical Electronics, Inc. (1992); B. V. Crist, *Handbooks of Monochromatic XPS spectra Vol.1*, XPS International, Inc. (1999)

[86] E. Schröder, R. Fasel, and A. Kiejna, *O adsorption and incipient oxidation of the Mg(0001) surface*, Appl. Phys. Rep. **67**, 2001 (2003)

[87] C. Bungaro, C. Noguera, P. Ballone, and W. Kress, *Early oxidation stages of Mg(0001): A density functional study*, Phys. Rev. Lett. **79**, 4433 (1997)

[88] R. Feder, A. Rodriguez, U. Baier, and E. Kisker, *Theoretical analysis of spin-resolved photoemission data from ferromagnetic Fe(001)*, Solid State Comm. **52**, 57 (1984)

[89] A. M. Turner, A. W. Donoho, and J. L. Erskine, *Experimental bulk electronic properties of ferromagnetic iron*, Phys. Rev. B **29**, 2986 (1984)

[90] B. T. Jonker, K.-H. Walker, E. Kisker, G. A. Prinz, and C. Carbone, *Spin-polarized photoemission study of epitaxial Fe(001) films on Ag(001)*, Phys. Rev. Lett. **57**, 142 (1986)

[91] E. Kisker, K. Schröder, W. Gudat, and M. Campagna, *Spin-polarized angle-resolved photoemission study of the electronic structure of Fe(001) as a function of temperature*, Phys. Rev. B **31**, 329 (1985)

[92] W. L. Moruzzi, J. F. Janak and A. R. Williams, *Calculated Electronic Properties of Metals*, Pergamon, New York (1978)

[93] K. B. Hathaway, H. J. F. Jansen and A. J. Freeman, *Total-energy local-spin-density approach to structural and electronic properties of ferromagnetic iron*, Phys. Rev. B **31**, 7603 (1985)

[94] R. Feder, W. Gudat, E. Kisker, A. Rodriguez and K Schröder, *Spin- and angle resolved photoemission from ferromagnetic Fe(001)*, Solid State Comm. **46**, 619 (1983)

[95] A. M. Turner and J. L. Erskine, *Surface electronic properties of Fe(100)*, Phys. Rev. B **30**, 6675 (1984)

[96] M. M. J. Bischoff, T. K. Yamada, C. M. Fang, R. A. de Groot, and H. van Kempen, *Local electronic structure of Fe(001) surfaces studied by scanning tunneling spectroscopy*, Phys. Rev. B **68**, 045422 (2003)

[97] J. A. Stroscio, D. T. Pierce, A. Davies, R. J. Celotta and M. Weinert, *Tunneling spectroscopy of bcc (001) surface states*, Phys. Rev. Lett. **75**, 2960 (1995)

[98] W. A. Hofer, J. Redinger, A. Biederman, and P. Varga, *Quenching surface states with the tip: STM scans on Fe(100)*, Surf. Sci. **482**, 1113 (2001)

[99] F. Matthes, L.-N. Tong, and C. M. Schneider, *Spin-polarized photoemission spectroscopy of the MgO/Fe interface on GaAs(100)*, J. Appl. Phys. **95**, 7240 (2004)

[100] M. Sicot, S. Andrieu, P. Turban, Y. Fagot-Revurat, H. Cercellier, A. Tagliaferri, C. De Nadai, N. B. Brookes, F. Bertran, and F. Fortuna, *Polarization of Fe(001) covered by MgO analyzed by spin-resolved x-ray photoemission spectroscopy*, Phys. Rev. B **68**, 184406 (2003)

[101] C. Li and A. J. Freeman, *Giant monolayer magnetization of Fe on MgO: A nearly ideal two dimensional system*, Phys. Rev. B **43**, 780 (1991)

[102] V. E. Henrich and P. A. Cox, *The Surface Science of Metal Oxides*, Cambride University Press (1994)

[103] W. Göpel and U. Lampe, *Influence of defects on the electronic structure of zinc oxide surfaces*, Phys. Rev. B **32**, 6447 (1980)

[104] B. M. Klein, W. E. Pickett, L. L. Boyer, and R. Zeller, *Theory of F centers in the alkaline-earth oxides MgO and CaO*, Phys. Rev. B **35**, 5802 (1987)

[105] A. Gibson, R. Haydock, and J. P. LaFemina, *Stability of vacancy defects in MgO: The role of charge neutrality*, Phys. Rev. B **50**, 2582 (1994)

[106] F. Illas and G. Pacchioni, *Optical properties of surface and bulk F centers in MgO from ab inito cluster model calculations*, J. Chem. Phys. **108**, 7835 (1998)

[107] R. F. Wood and T. M. Wilson, *Electronic structure of the F-center in CaO*, Phys. Rev. B **15**, 3700 (1977)

[108] C. Jun, L. Lin, T. Lu, and L. Yong, *Electronic structure of F, F^+ centers in MgO*, Eur. Phys. J. B **9**, 593 (1999)

[109] E. Vescovo, C. Carbone, W. Eberhardt, O. Rader, T. Kachel, and W. Gudat, *Spin-resolved photoemission study of the clean and oxygen-covered Fe(110) surface*, Phys. Rev. B **48**, 285 (1993)

[110] M. Sterrer, E. Fischbach, T. Rice, and H.-J. Freund, *Geometric characterization of a singly charged oxygen vacancy on a single-crystalline MgO(001) film by electron paramagnetic resonance*, Phys. Rev. Lett. **94**, 186101 (2005)

[111] M. Sterrer, M. Heyde, M. Novicki, N. Nilius, T. Risse, H.-P. Rust, G. Pacchioni, and H.-J. Freund, *Identification of color centers on Mg(001) thin films with scanning tunneling microscopy*, J. Phys. Chem. B Lett. **110**, 46 (2006)

[112] P. G. Mather, J. C. Read, and R. A. Buhrman, *Disorder, defects and band gaps in ultrathin (001) MgO tunnel barrier layers*, Phys. Rev. B **73**, 205412 (2006)

[113] A. M. Ferrari and G. Pacchioni, *Electronic structure of F- and V- centers on the MgO surface*, J. Phys. Chem. **99**, 17010 (1995)

[114] J. P. Velev *et al.*, 10^{th} Joint MMM/Intermag conference 2007 and private communication

[115] K. O. Legg, F. P. Jona, D. W. Jepsen, and P. M. Marcus, *Structural analysis of oxygen adsorption on Fe(001)*, J. Phys. C: Solid State Phys. **8**, L492 (1975)

[116] A. Clarke, N. B. Brookes, P. D. Johnson, M. Weinert, B. Sinkovic, and N. V. Smith, *Spin-polarized photoemission studies of the adsorption of O and S on Fe(001)*, Phys. Rev. B **41**, 9659 (1990)

[117] C. F. Bruckner and T. N. Rhodin, *Oxygen chemisorption and reaction on α-Fe(100) using photoemission and low-energy electron diffraction*, Surf. Sci. **57**, 523 (1976)

[118] R. L. Fink, G. A. Mulhollan, A. B. Andrews, J. L. Erskine, and G. K. Walters, *Spin- and angle-resolved photoemission study of chemisorbed p(1x1) O on epitaxial ultrathin Fe/W(001) films*, Phys. Rev. B **45**, 9824 (1992)

[119] G. Panzner, D. R. Mueller and T. N. Rhodin, *Angle-resolved photoemission studies of oxygen adsorbed on Fe(100)*, Phys. Rev. B **32**, 3472 (1985)

[120] P. D. Johnson, A. Clarke, N. B. Brookes, S. L. Hulbert, B. Sinkovic, and N. V. Smith, *Exchange-split adsorbate bands: The role of substrate hybridization*, Phys. Rev. Lett. **61**, 2257 (1988)

[121] E. Y. Tsymbal, I. I. Oleinik, and D. G. Pettifor, *Oxygen-induced positive spin-polarization from Fe into the vacuum barrier*, J. Appl. Phys. **87**, 5230 (2000)

[122] H. Huang and J. Hermanson, *Bonding and magnetism of chemisorbed oxygen on Fe(001)*, Phys. Rev. B **32**, 6312 (1985)

[123] L. Duò, R. Bertacco, G. Isella, F. Ciccacci, and M. Richter, *Electronic and magnetic properties of the Co/Fe(001) interface and the role of oxygen*, Phys. Rev. B **61**, 15294 (2000)

[124] H. Wieldraaijer, J. T Kohlhepp, P. LeClair, K. Ha, and W. J. M. de Jonge, *Growth of epitaxial bcc Co(001) electrodes for magnetoresistive devices*, Phys. Rev. B **67**, 224430 (2003)

[125] V. L. Moruzzi, P. M. Marcus, H. Schwarz, and P. Mohn, *Ferromagnetic phases of bcc and fcc Fe, Co, and Ni*, Phys. Rev. B **34**, 1784 (1986)

[126] E. Y. Tsymbal, K. D. Belashenko, J. P. Velev, S. S. Jaswal, M. van Schilfgaarde, I. I. Oleynik, and D. A. Stewart, *Interface effects in spin-dependent tunneling*, cond-mat/0511663

Danksagung

An dieser Stelle möchte ich allen herzlich danken, die zum Gelingen dieser Arbeit beigetragen haben.

Mein besonderer Dank gilt Herrn Prof. Dr. Claus M. Schneider für seine Unterstützung und Förderung in allen Phasen dieser Arbeit, seine Diskussionsbereitschaft, die vielen wertvollen Anregungen und die motivierende Zeit.

Herrn Prof. Dr. Rolf Möller danke ich für die Übernahme des Korreferats.

Herrn Dr. Frank Matthes danke ich für seine Betreuung, die angenehme Zusammenarbeit und seine unersetzliche Unterstützung während der zahllosen Strahlzeitwochen in Dortmund und Berlin, sowie für die Durchsicht dieser Arbeit.

Dr. Heiko Braak gilt mein Dank für seine Geduld und Hilfe bei den MOKE Messungen, für die Durchsicht von Teilen dieser Arbeit und die netten Gespräche über die Physik hinaus.

Dr. Matthias Buchmeier danke ich für das Teilen seines Expertenwissens bezüglich MOKE und die Hilfe bei den Messungen.

Dr. Stefan Cramm danke ich für die hilfreichen Diskussionen über XPS und die Dortmunder Beamline.

Dr. Daniel Bürgler danke ich für die kritischen Anmerkungen zu Teilen dieser Arbeit.

Dr. Diana Rata gilt mein Dank für alle Präparationsratschläge und die vielen netten Gespräche.

Herrn Bernd Küpper und Herrn Konrad Bickmann danke ich vielmals für die technische Unterstützung bei allen Strahlzeitvorbereitungen und die spontane Hilfsbereitschaft beim Aufbau des Experimentes vor der letzten Strahlzeit bei DELTA.

Bei Herrn Heinz Pfeiffer bedanke ich mich für alle Rettungs- und Wiederbelebungsmassnahmen von grossen und kleinen, alten und versiegelten, kaputten und gehimmelten Geräten. Herrn Jürgen Lauer danke ich für die Umsetzung und Optimierung des Messprogramms.

Frau Jutta Gollnick danke ich für alle organisatorische Hilfe und spannende Einblicke in die Welt des Profifussballs.

Allen Mitarbeitern des Instituts 'Elektronische Eigenschaften' sei an dieser Stelle für die kollegiale und angenehme wissenschaftliche Atmosphäre gedankt.

Den Mitarbeitern von DELTA (Dortmund) ein Dankeschön für ihre unkomplizierte Hilfe bei technischen Problemen, die Gastfreundschaft im Kontrollraum und die zahlreichen Zusatzinjektionen.

Dr. Jan Minar danke ich für die erfolgreichen Ferndiagnosen und hilfreichen Antworten auf alle SPR-KKR-spezifischen Fragen.

Bei Alexandra Steeb bedanke ich mich herzlich für den gegenseitigen seelischen Austausch während unserer gemeinsamen Doktorandenzeit.

Elena Charalambakis danke ich sehr herzlich für ihre Freundschaft und Zuverlässigkeit weit über unsere Aachener Studienzeit hinaus.

Schliesslich möchte ich meinen Eltern Evelyn und Dietmar Müller danken, die immer für mich da sind und mir stets Rückhalt und Unterstützung geben.

Robert, ich danke Dir für diese Jahre unseres Lebens.

1. **Physik der Nanostrukturen**
   Vorlesungsmanuskripte des 29. IFF-Ferienkurses vom 9. bis 20.3.1998
   (1998), ca. 1000 Seiten
   ISBN: 978-3-89336-217-2

2. **Magnetische Schichtsysteme**
   Vorlesungsmanuskripte des 30. IFF-Ferienkurses vom 1. bis 12.3.1999
   (1999), ca. 1300 Seiten, zahlreiche z.T. farb. Abb.
   ISBN: 978-3-89336-235-6

3. **Femtosekunden und Nano-eV: Dynamik in kondensierter Materie**
   Vorlesungsmanuskripte des 31. IFF-Ferienkurses vom 13. bis 24.3.2000
   (2000), ca. 1000 Seiten, zahlreiche z. T. farb. Abb.
   ISBN: 978-3-89336-205-9 (Hardcover)

4. **Massenspektrometrische Verfahren der Elementspurenanalyse**
   Kurzfassungen der Vorträge und Poster des 5. Symposiums und des
   12. ICP-MS-Anwendertreffens vom 18. bis 21. September 2000 in Jülich
   zusammengestellt von H.-J. Dietze, J. S. Becker (2000), XVI, 109 Seiten
   ISBN: 978-3-89336-267-7

5. **Neutron Scattering**
   Lectures of the Laboratory Course
   held at the Forschungszentrum Jülich from 26 September to 6 October 2000
   herausgegeben von Th. Brückel, G. Heger, D. Richter (2000), 382 Seiten
   ISBN: 978-3-89336-269-1

6. **Baryon Excitations**
   Lectures of the COSY Workshop
   held at the Forschungszentrum Jülich from 2 to 3 May 2000
   edited by T. Barnes and H.-P. Morsch (2000), 203 pages
   ISBN: 978-3-89336-273-8

7. **Neue Materialien für die Informationstechnik**
   Vorlesungsmanuskripte des 32. IFF-Ferienkurses vom 05. bis 16.03.2001
   herausgegeben von R. Waser (2001), ca. 1200 Seiten, zahlreiche z. T. farb. Abb.
   ISBN: 978-3-89336-279-0

8. **Deutsche Neutronenstreutagung 2001**
   Kurzfassungen der Vorträge und Poster der
   Deutschen Neutronenstreutagung 2001 vom 19. bis 21. Februar 2001 in Jülich
   zusammengestellt von Th. Brückel (2001), XVI, 186 Seiten
   ISBN: 978-3-89336-280-6

9. **Neutron Scattering**
   Lectures of the 5th Laboratory Course
   held at the Forschungszentrum Jülich from 18 September to 28 September 2001
   edited by Th. Brückel, G. Heger, D. Richter, R. Zorn (2001), 418 pages
   ISBN: 978-3-89336-288-2

10. **Soft Matter. Complex Materials on Mesoscopic Scales**
    Lecture manuscripts of the 33rd IFF winter school on March 04 - 14 2002
    edited by J. K. G. Dhont, G. Gompper, D. Richter (2002),
    c. 1000 pages, many partly coloured illustrations
    ISBN: 978-3-89336-297-4 (Hardcover)

11. **Proceedings of the symposium on threshold meson production in pp and pd interaction**
    Extended COSY-11 Collaboration Meeting Cracow, 20 - 24 June 2001
    edited by P. Moskal, M. Wolke (2002), 274 pages
    ISBN: 978-3-89336-307-0

12. **Polarized Neutron Scattering**
    Lectures of the 1st Summer School held at the Forschungszentrum Jülich
    from 10 to 14 September 2002
    edited by Th. Brückel, W. Schweika (2002), 360 pages
    ISBN: 978-3-89336-314-8

13. **Beam Cooling and Related Topics**
    255th International WE-Heraeus-Seminar, Bad Honnef, May 13 - 18, 2001
    Proceedings
    edited by D. Prasuhn (2002), PDF-Datei auf CD
    ISBN: 978-3-89336-316-2

14. **Fundamentals of Nanoelectronics**
    34th Spring School of the Department of Solid State Research,
    10 - 21 March 2003, Jülich, Germany
    edited by S. Bluegel, M. Luysberg, K. Urban, R. Waser (2003), c. 1000 pages
    ISBN: 978-3-89336-319-3 (Hardcover)

15. **Neutron Scattering**
    Lectures of the Laboratory course held at the Forschungszentrum Jülich
    edited by Th. Brückel, G. Heger, D. Richter, R. Zorn (2003), 375 pages
    New, revised edition of Materie und Material / Matter and Materials Volume 9
    ISBN: 978-3-89336-324-7

16. **Proceedings of the 1st Summer School 2002 and Workshop on COSY Physics**
    28. August - 4. September 2002
    Organizing Committee: K. Brinkmann, M. Büscher, et al. (2003), CD-ROM
    ISBN: 978-3-89336-331-5

17. **Resource-orientated Analysis of Metallic Raw Materials: Findings of CRC 525 for Aluminium**
edited by W. Kuckshinrichs, P. N. Martens (2003), CD-ROM
ISBN: 978-3-89336-342-1

18. **The Physics of Spallation Processes: Theory, Experiments and Applications**
by F. Goldenbaum (2004), V, 174 pages
ISBN: 978-3-89336-346-9

19. **Physics meets Biology: From Soft Matter to Cell Biology**
Lecture manuscripts of the 35th IFF Spring School from March 22 – April 2, 2004, Jülich, Germany
edited by G. Gompper, U. B. Kaupp, J. K. G. Dhont, D. Richter, R. G. Winkler (2004), c. 900 pages
ISBN: 978-3-89336-348-3

20. **Advanced Cold Moderators ACoM-6**
Proceedings of the 6th International Workshop on Advanced Cold Moderators held at Forschungszentrum Jülich from 11 to 13 September 2002
edited by H. Conrad (2004), 223 pages
ISBN: 978-3-89336-363-6

21. **Proceedings of the second symposium on threshold meson production in pp and pd interaction**
Extended COSY-11 Collaboration Meeting, Cracow, 1-3 June 2004
ed. by P. Moskal (2004), c. 300 pages
ISBN: 978-3-89336-366-7

22. **Ferroelectric Tunnel Junctions**
by J. Rodríguez Contreras (2004), VIII, 162 pages
ISBN: 978-3-89336-368-1

23. **Development of Ellipsometric Microscopy as a Quantitative High-Resolution Technique for the Investigation of Thin Films at Glass-Water and Silicon-Air Interfaces**
by F. Linke (2004), 135 pages
ISBN: 978-3-89336-373-5

24. **Caucasian-German School and Workshop on Hadron Physics**
Organizing Committee: M. Büscher, A. Kacharava, M. Nioradze, F. Rathmann, H. Ströher (2004), CD-ROM
ISBN: 978-3-89336-375-9

25. **6th ANKE Workshop on Strangeness Production on Nucleons and Nuclei**
Organizing Committee: M. Büscher, V. Kleber, Y. Valdau
(2004), CD-ROM
ISBN: 978-3-89336-376-6

26. **Magnetism goes Nano**
Lecture manuscripts of the 36th IFF Spring School February 14 – 25, 1005, Jülich, Germany
edited by S. Blügel, T. Brückel, C. M. Schneider (2005), c. 1000 pages
ISBN: 978-3-89336-381-0

27. **Hochfrequenzeigenschaften gepulster, supraleitender Halbwellenresonatoren zur Beschleunigung leichter Ionen**
von R. Stassen (2005), VI, 128 Seiten
ISBN: 978-3-89336-394-0

28. **Neutron Scattering**
Lectures of the Laboratory course held at the Forschungszentrum Jülich
edited by Th. Brückel, G. Heger, D. Richter, R. Zorn (2005), c. 500 pages
New, revised edition of Materie und Material / Matter and Materials Volume 15
ISBN: 978-3-89336-395-7

29. **K^+-Meson Production in Nuclei**
by M. Büscher (2005), 1 CD-ROM
ISBN: 978-3-89336-398-8

30. **STORI'05**
6th International Conference on Nuclear Physics at Storage Rings
23–26 May 2005, Jülich – Bonn
edited by D. Chiladze, A. Kacharava, H. Ströher (2005), c. 400 pages
ISBN: 978-3-89336-404-6

31. **Wetting and Interdiffusion:**
Establishment of a Bio-compatible System and Studies of its Dynamics
by A.-K. Prechtel (2005), 139 pages
ISBN: 978-3-89336-421-3

32. **Computational Condensed Matter Physics**
Lecture manuscripts of the 37th IFF Spring School March 06 – 17, 2006, Jülich, Germany
edited by S. Blügel, G. Gompper, E. Koch, H. Müller-Krumbhaar, R. Spatschek, R. G. Winkler (2006), c. 1000 pages
ISBN: 978-3-89336-430-5

33. **Spin in Hadron Physics**
2nd Caucasian-German School and Workshop on Hadron Physics
Organizing Committee: A. Kacharava … (2006), CD-ROM
ISBN: 978-3-89336-453-4

34. **Probing the Nanoworld**
Microscopies, Scattering and Spectroscopies of the Solid State
Lecture manuscripts of the 38th IFF Spring School March 12 – 23, 2007 Jülich, Germany
edited by K. Urban, C. M. Schneider, T. Brückel, S. Blügel, K. Tillmann, W. Schweika, M. Lentzen, L. Baumgarten (2007), c. 1000 pages
ISBN: 978-3-89336-462-6

35. **Future Perspectives of European Materials Research**
edited by G. Schumacher, St. Preston, A. Smith, St. Reschke (2007), c. 80 pages
ISBN: 978-3-89336-477-0

36. **Physics of more than 11 years of COSY-11 – history, status, achievements, plans**
edited by J. Przerwa, D. Grzonka, P. Klaja, P. Moskal, W. Oelert (2007), 127 pages
ISBN: 978-3-89336-483-1

37. **ANKE/PAX Workshop on SPIN PHYSICS, Ferrara 2007**
Organizing Committee: G. Ciullo, A. Kacharava, P. Lenisa, F. Rathmann, H. Ströher (2007), CD-ROM
ISBN: 978-3-89336-487-9

38. **Neutron Scattering**
Lectures of the JCNS Laboratory Course held at Forschungszentrum Jülich and the research reactor FRM II of TU Munich
edited by Th. Brückel, G. Heger, D. Richter, R. Zorn (2007), c. 500 pages
New, revised edition of Materie und Material / Matter and Materials Volume 28
ISBN: 978-3-89336-489-3

39. **Magnetic and structural properties of thin films and nanoparticles studied by scattering methods**
by M. Feygenson (2007), III, 121 pages
ISBN: 978-3-89336-490-9

40. **Electronic Structure of Ferromagnet-Insulator Interfaces: Fe/MgO and Co/MgO**
by M. Müller (2007), 102 pages
ISBN: 978-3-89336-493-0

Band/Volume 40
ISBN 978-3-89336-493-0

Materie und Material
Matter and Materials